# Improving Mass and Concentration Sensitivity of Nuclear Magnetic Resonance for the Detection of Ligand-Binding Using Bullet-DNP

Zur Erlangung des akademischen Grades einer

Doktorin der Naturwissenschaften

(Dr. rer. nat.)

von der KIT-Fakultät für Chemie und Biowissenschaften des
Karlsruher Instituts für Technologie (KIT)

genehmigte

Dissertation

von

M.Sc. Pooja Pooja

aus Haryana (India)

Tag der mündlichen Prüfung: 18. Dezember 2025
1. Referent: PD Dr. Benno Meier
2. Referentin: apl. Prof. Dr. Gisela Guthausen

# Statutory Declaration

The submitted dissertation entitled

*"Improving Mass and Concentration Sensitivity of Nuclear Magnetic Resonance for the Detection of Ligand-Binding Using Bullet-DNP"*

is my own independent work. I have used only the sources and aids indicated in the thesis and have not made use of any unauthorised assistance from third parties. This work, in whole or in part, has not previously been submitted to any other university in Germany or abroad as part of an examination or qualification procedure. I confirm the accuracy of the above declaration and am aware of the significance of this statutory declaration as well as the legal consequences of making a false or incomplete declaration in lieu of an oath.

I hereby affirm in lieu of an oath that I have, to the best of my knowledge, stated the pure truth and have not concealed anything.

Karlsruhe, 04.11.2025

| | |
|---|---|
| Ort, Datum | Pooja Pooja |

# List of Publications

1. **Narwal, P.**; Lorz, N.; Minaei, M.; Jannin, S.; Kouril, K.; Gossert, A.; Meier, B., "Bullet-DNP Enables NMR Spectroscopy of Pyruvate and Amino Acids at Nanomolar to Low Micromolar Concentrations." *Analytical Chemistry* **2024**, *96* (37), 14734-14740.

2. **Narwal, P.**; Minaei, M.; Lorz, N.; Gossert, A.D.; Meier, B., "Single-Scan Detection of Ligand Binding Using Hyperpolarization and Low-Field Relaxation." *Communications Chemistry*, **2026**, *9* (1), 140-140.

3. Turhan, E.; Minaei, M.; **Narwal, P.**; Meier, B.; Kouřil, K.; Kurzbach, D., "Short-Lived Calcium Carbonate Precursors Observed In Situ via Bullet-Dynamic Nuclear Polarization." *Communications Chemistry* **2024**, *7* (1), 210.
The topic of this publication is not part of this thesis.

4. Razanahoera, A.; Sonnefeld, A.; Sheberstov, K.; **Narwal, P.**; Minaei, M.; Kouril, K.; Bodenhausen, G.; Meier, B., "Hyperpolarization of Long-Lived States of Protons in Aliphatic Chains by Bullet Dynamic Nuclear Polarization, Revealed on the Fly by Spin-Lock-Induced Crossing." *The Journal of Physical Chemistry Letters* **2024**, *15* (35), 9024-9029.
The topic of this publication is not part of this thesis.

5. Schmidt, D.; Gartner, P.; Berezkin, I.; Rudat, J.; Bilger, M.; Grünert, T.; Zimmerer, N.; Quarz, P.; Scharfer, P.; Brückel, J.; Jung, A.P.; **Pooja, P.** et al., "Selective Peptide Binders to the Perfluorinated Sulfonic Acid Ionomer Nafion." *Advanced Functional Materials* **2024**, *34* (20), 2214932.
The topic of this publication is not part of this thesis.

# Acknowledgements

First and foremost, I wish to express my sincere gratitude to my doctoral supervisor, PD Dr. Benno Meier. I am deeply thankful that he welcomed me into his lab and introduced me to the fascinating world of bullet-DNP, which became the core of this thesis. This opportunity allowed me to come to Germany from India and embark on this incredible scientific journey. I am indebted to his exceptional guidance, our insightful scientific discussions, and his constant support throughout my research. I would also like to sincerely thank Prof. Dr. Gisela Guthausen for agreeing to be my co-referee.

I am profoundly grateful to our collaborators at ETH Zürich, whose contributions were essential to the success of this work. My deepest thanks go to Dr. Alvar Gossert, who has been a second supervisor to me, providing invaluable guidance, constant availability for scientific discussions, and unwavering support throughout this project. I also extend my sincere thanks to Nils Lorz for his key contributions in providing the PHD1 protein and for his collaborative spirit and assistance with the experiments.

My sincere appreciation goes to Dr. Karel Kouřil and Dr. Masoud Minaei, who not only shared their expertise but were also always patient in listening to my questions and offering guidance whenever I felt lost. I also wish to thank my other lab colleagues, Dr. Michael Jurkutat, Dr. Kajum Safiullin, Pooja Singh, and Dmitrii Zasukhin, for their camaraderie and support. A special thanks to Dr. Hana Kouřilová for her unwavering friendship and support, which extended far beyond the laboratory. Her presence has been a constant throughout my journey.

I would like to acknowledge all team members at IBG-4, as well as former members, for many enjoyable hours over coffee and other activities. I am also grateful to Prof. Dr. Burkhard Luy and PD Dr. Claudia Muhle-Goll for providing a productive and supportive research environment at IBG-4.

Finally, I am greatly indebted to my parents and family for their unwavering support over the years. None of this would have been possible without them. I also extend my heartfelt thanks to Nishkarsh Sharma for his understanding and constant support throughout this journey. My gratitude also extends to all my friends, both here in Germany and back home in India.

# Abstract

Nuclear Magnetic Resonance (NMR) spectroscopy is a powerful tool for studying molecular structure, dynamics, and ligand-protein interactions. However, its inherently low sensitivity limits applications involving small sample quantities. This thesis aims to overcome this limitation by employing bullet dissolution dynamic nuclear polarization (bullet-DNP) to enhance NMR sensitivity and enable detection of very small sample amounts.

Optimized sample preparation, including multilayer formulations and solvent systems facilitating spin diffusion, enables efficient hyperpolarization even with sub-microliter volumes. Sensitivity is further improved using indirect proton detection via a $^{13}C \rightarrow ^{1}H$ INEPT transfer a TBI probe, achieving a fourfold enhancement over direct $^{13}C$ detection. Using this approach, 2-$^{13}C$-labeled pyruvate is detected at concentrations as low as 250 nM, corresponding to a total employed mass of only 20 ng.

The enhanced sensitivity is applied to investigate ligand-protein interactions at physiologically relevant concentrations. Using the human PHD1 protein as a model system, a low-field relaxation method is developed that exploits the sensitivity of the longitudinal relaxation rate ($R_1$) to binding at low magnetic fields. Binding is detectable at protein concentrations as low as 2 μM, representing a 10-fold reduction compared to conventional NMR experiments. Quantitative analysis of binding contrast reveals a 5-fold enhancement in $R_1$-based contrast, compared to a 2-3 fold increase for $R_{1\rho}$, establishing $R_1$ relaxometry as a sensitive probe for low-field studies of ligand-protein interactions. This work establishes bullet-DNP enhanced NMR as a versatile platform for studying biomolecular systems with minimal sample requirements, opening new possibilities for investigating metabolic processes and protein-ligand interactions under near-physiological conditions.

# Zusammenfassung

Die Kernspinresonanzspektroskopie (NMR) ist ein leistungsfähiges Werkzeug zur Untersuchung der Struktur und Dynamik von Molekülen, sowie von Wechselwirkungen zwischen Molekülen. Zu diesen Wechselwirkungen zählen insbesondere die Wechselwirkungen zwischen Liganden und Proteinen. Allerdings schränkt die geringe Empfindlichkeit der NMR die Anwendungsmöglichkeiten bei kleinen Probenmengen ein.

Diese Arbeit zielt darauf ab, diese Einschränkung zu überwinden, indem die NMR-Empfindlichkeit durch den Einsatz der sogenannten bullet-DNP (bullet-dynamic nuclear polarization) erhöht und eine massenbegrenzte Detektion erreicht wird.

Eine optimierte Probenvorbereitung, einschließlich mehrschichtiger Formulierungen und Lösungsmittelsysteme, die die Spindiffusion erleichtern, ermöglichte eine effiziente Hyperpolarisation selbst bei Volumina im Submikroliterbereich. Die Empfindlichkeit wurde durch indirekte Protonendetektion mittels $^{13}C \rightarrow ^{1}H$-INEPT-Transfer und den Einsatz eines TBI Probenkopfs weiter verbessert, wodurch eine zusätzliche vierfache Steigerung gegenüber der direkten $^{13}C$-Detektion erreicht wurde. Mit diesem Ansatz wurde 2-$^{13}C$-markiertes Pyruvat in Konzentrationen von nur 250 nM nachgewiesen, was einer insgesamt verwendeten Probenmasse von nur 20 ng entspricht.

Die verbesserte Empfindlichkeit wurde anschließend zur Untersuchung von Liganden-Protein-Wechselwirkungen bei physiologisch relevanten Konzentrationen eingesetzt. Unter Verwendung des menschlichen PHD1-Proteins als Modellsystem wurde eine Niedrigfeld-Relaxationsmethode entwickelt, die die starke Abhängigkeit der longitudinalen Relaxationsrate $R_1$ von der Molekülgröße bei niedrigen Magnetfeldern für die Detektion der Bindung ausnutzt. Eine Ligand-Protein Bindung war bereits bei Proteinkonzentrationen von nur 2 µM nachweisbar, was einer 10-fachen Verringerung im Vergleich zu herkömmlichen NMR-Experimenten entspricht. Die quantitative Analyse des Bindungskontrasts ergab eine durch das Protein verursachte 5-fache Beschleunigung der $R_1$-Relaxation des Liganden im Vergleich zu einer 2- bis 3-fachen Beschleunging der $R_{1\rho}$-Relaxation, wodurch die Eignung von Hyperpolarisation und Niedrigfeld-$R_1$-Relaxometrie für die Bestimmung von Liganden-Protein-Wechselwirkungen gezeigt wurde. Diese Arbeit etabliert die Bullet-DNP-verstärkte NMR als vielseitige Plattform für die Untersuchung biomolekularer Systeme mit minimalen Probenanforderungen und eröffnet neue Möglichkeiten für die Untersuchung von Protein-Ligand-Wechselwirkungen unter nahezu physiologischen Bedingungen.

# Contents

# 1. Introduction

NMR spectroscopy is a highly versatile and non-destructive technique used across a wide range of scientific disciplines, including organic synthesis, polymer chemistry, and studies of ligand binding in drug discovery. Despite its wide applicability, NMR suffers from inherently low sensitivity due to the small thermal equilibrium polarization of nuclear spins. This limitation often requires high sample concentrations (10-100 μM) and long acquisition times, which restricts its use in studies involving scarce or low-concentration samples. To overcome this sensitivity limitation, several hyperpolarization techniques have been developed, which transiently enhance nuclear spin polarization by several orders of magnitude. These methods are briefly discussed in Chapter 2. Among them, the dissolution dynamic nuclear polarization (D-DNP) technique, introduced by Ardenkjær-Larsen and co-workers in 2003, has been very useful[1]. In D-DNP, polarization is transferred from unpaired electron spins (which possess a high gyromagnetic ratio) to neighboring nuclear spins, such as $^{1}$H or $^{13}$C, under cryogenic conditions in the solid state. The hyperpolarized solid sample is quickly dissolved using a solvent to yield a liquid solution with NMR spectra that show signal enhancements of several thousand-fold, providing structural and dynamic information.

However, D-DNP has several practical limitations, including the use of hot solvents, substantial sample dilution during dissolution, and polarization losses during transfer from the polarizer to the NMR spectrometer. To address these challenges, a new variant known as bullet-DNP was introduced by Kouřil and co-workers in 2019[2, 3]. In this method, the hyperpolarized solid sample is enclosed in a small “bullet” and is transported between magnets using pressurized helium gas. This innovation enables rapid and efficient hyperpolarized sample transfer while minimizing polarization losses and dilution, resulting in significantly improved sensitivity and reproducibility.

In this thesis, the bullet-DNP technique has been applied to improve the mass sensitivity of NMR experiments, enabling the detection of extremely small sample amounts down to nanograms or nanomolar concentrations. Achieving such sensitivity required optimizing both the sample formulation for hyperpolarization and the subsequent detection scheme within the existing bullet-DNP setup. The focus of this work is to systematically enhance mass sensitivity for a variety of ligands through a set of complementary strategies. The most straightforward approach involved reducing the sample volume. To achieve efficient hyperpolarization within small volumes, a three-layer sample preparation protocol was developed, as detailed in Chapter 4. However, achieving sufficient polarization also requires effective spin diffusion, which becomes limited in low-concentration samples. Therefore, solvent systems promoting spin diffusion - such as $^{13}$C-labeled DMSO in combination with various co-solvents were investigated and optimized. Once efficient polarization levels were achieved, attention was directed toward improving the detection sensitivity.

Direct $^{1}$H detection was discarded in the liquid-state due to the short $T_1$ relaxation time, whereas direct $^{13}$C detection, although longer-lived, provided limited information for downstream ligand-binding studies. A more effective strategy involved indirect proton detection via $^{13}$C→$^{1}$H INEPT in the liquid state, enabling polarization transfer from $^{13}$C to $^{1}$H. Using a probe optimized for proton detection further enhanced sensitivity, yielding approximately 4-fold higher signal-to-noise ratio compared to

direct $^{13}$C observation. Through these combined improvements, $^{13}$C-labeled pyruvate was detected at concentrations as low as 250 nM, corresponding to only 20 ng of material. To further validate its use for *in vivo* metabolic imaging, experiments with delayed detection (60 s) were conducted, which is more closely related to imaging delays. This experiment yielded strong signals (SNR $\approx$ 58 after $^{1}$H detection via INEPT), indicating that this method could potentially be applied to *in vivo* metabolic imaging. Overall, this work demonstrates that optimized bullet-DNP enables sensitive NMR detection suitable for potentially pre-clinical imaging applications. The developed methodologies are broadly applicable to any molecular system containing long-lived $^{13}$C, such as carbonyl carbons, thus paving the way for studying metabolic transformations and ligand interactions at physiologically relevant concentrations.

To demonstrate the broader applicability of this enhanced sensitivity, the optimized bullet-DNP system was employed to study ligand-protein interactions at low magnetic fields. Ligand-protein complexes typically exhibit faster $R_1$ relaxation compared to free ligands, and this difference becomes more pronounced at lower fields (nearly 1 T). The solvent reservoir in the bullet-DNP setup, situated at this field, allowed ligand-protein mixing immediately after hyperpolarization and prior to detection. In this work, the PHD1 protein, which contains a paramagnetic center, was used to investigate this relaxation behavior. The paramagnetic contribution further accelerated relaxation, enabling experiments with very small protein concentrations (as low as 2 µM). With the previously optimized mass sensitivity and INEPT-based $^{1}$H detection, ligand concentrations of 14 µM and protein concentrations of 2 µM were sufficient to detect binding, representing a 10-fold reduction compared to conventional requirements. The ligand-binding interactions were confirmed using $R_{1\rho}$-based double acquisition experiments combined with competition binding, which provided quantitative binding scores (Q1 and Q2 values).

Further, the detection of binding was based on quantifying changes in relaxation behavior between the free and protein-bound states. Two complementary relaxation rates were examined: the longitudinal rate $R_1$ during low-field evolution, and the effective transverse rate $R_{1\rho}$ during a spin-lock period at high-field. Binding-induced contrast was expressed as $C_R = (R - R_0)/R_0$, where $R_0$ denotes the relaxation rate of the free ligand. This analysis revealed that $R_1$-based contrast exhibited superior sensitivity to binding at low magnetic field, showing a 5-fold enhancement at 2 µM PHD1 compared to a 2-3 fold increase in $R_{1\rho}$ contrast. The practical impact of binding was reflected in the calculated relaxation times. The observed $T_1$ decreases from $\sim$ 46 s for the free ligand to $\sim 8 - 9$ s in the presence of 2 µM PHD1. This value represents the population-weighted average of the free and bound states, indicating a significant fraction of ligand molecules experiencing the fast relaxation environment of the protein complex. Together, these findings confirm that the observed relaxation enhancements are a direct result of binding interactions.

# 2. Theory of Nuclear Magnetic Resonance

## 2.1. Introduction to NMR

In Nuclear Magnetic Resonance (NMR), the intrinsic spin of certain nuclei serves as a probe to study the structure and dynamics of molecules. Many nuclei possess a non-zero spin angular momentum, which gives rise to a magnetic moment. When exposed to an external magnetic field $B_0$, these nuclear spins occupy discrete energy levels, and transitions between them can be induced by radiofrequency (RF) irradiation. The resulting spectra provide detailed information about the chemical and magnetic environment of the nuclei.

The theoretical description of NMR can be approached from two complementary approaches. The "classical picture" describes nuclear spins as tiny bar magnets that rotate in space. When these spins are placed in an external magnetic field, they align along the z-axis, creating a magnetization vector. This framework provides an intuitive understanding for many experiments. Second, the "quantum mechanical description" is required for a rigorous understanding of spin dynamics, energy levels, and relaxation phenomena. In this chapter, both approaches will be introduced: the classical vector model to build intuition, and the quantum mechanical formalism to establish a solid foundation for the more advanced concepts discussed later in this thesis. This chapter is mainly based on the theory outlined in References [4, 5] and should provide the background needed to follow later chapters.

### 2.1.1. NMR-active nuclei: the spin-1/2

A particle such as a proton has a spin angular momentum $\vec{I}$, which does not arise from any physical motion but from an intrinsic property of the nuclei called "spin". This property remains constant and unaffected by the surrounding environment. Spin is quantified by spin-quantum number $I$, which can have integer values (0, 1, 2, ...) or half-integer values (1/2, 3/2, 5/2, ...). Particles with integer spin are called bosons, while those with half-integer spin are known as fermions. Nuclei with $I = 0$ have no spin and are NMR-inactive, whereas those with $I \geq 1/2$ are NMR-active.

In this thesis, we focus primarily on spin-1/2 nuclei, in particular the proton ($^1$H, natural abundance 99.98%) and the carbon isotope $^{13}$C (natural abundance ~1%). Neglecting nuclei with spin greater than 1/2 allows us to avoid the additional complexity of quadrupolar interactions. The magnitude of the nuclear spin angular momentum is given by:

$$|\vec{I}| = \hbar\sqrt{I(I+1)}, \tag{2.1}$$

where $\hbar$ is the reduced Planck constant. For a spin-1/2 nucleus, this corresponds to $|\vec{I}| = \sqrt{3/4}\,\hbar$.

Quantum mechanics restricts the measurable component of $\vec{I}$ to one axis, conventionally chosen as the $z$-axis. The projection of $\vec{I}$ along the $z$-axis, given by:

$$I_z = m_I\hbar, \tag{2.2}$$

where $m_I$ can take $(2I + 1)$ discrete values from $-I$ to $+I$. For $I = 1/2$, there are two possible states, $m_I = \pm 1/2$, corresponding to the "spin-up" and "spin-down" states. In the presence of a magnetic field $B_0$, each $m_I$ orientation corresponds to a unique energy level due to the interaction between the nuclei's magnetic moment and the external field. This is known as the "Zeeman splitting".

$$E = -m_I \gamma \hbar B_0, \tag{2.3}$$

where $\gamma$ is the gyromagnetic ratio of the nucleus, specified in rad $s^{-1}$ $T^{-1}$. It can be positive or negative, depending on the magnetic moment's direction. The magnetic moment of a nuclear spin is defined as:

$$\vec{\mu} = \gamma \hbar \vec{I}, \tag{2.4}$$

which allows it to interact with external magnetic fields. This interaction is known as the Zeeman interaction, and the fundamental basis of NMR

### 2.1.2. Spin Precession

The angular momentum of a particle with spin is a vector that can orient in any direction. When an external magnetic field $B_0$ is applied, the magnetic moment of the spin moves on a cone, keeping a constant angle between the spin magnetic moment and the magnetic field. This motion is known as "spin precession". The frequency of this precession $\omega_0$ is called "Larmor precession frequency" and is given by:

$$\omega_0 = -\gamma B_0 \tag{2.5}$$

High-field NMR experiments typically have Larmor frequencies of hundreds of megahertz.

### 2.1.3. Boltzmann Distribution

In a spin-1/2 system, once the spin states are split by the external magnetic field, their populations are not equally populated at thermal equilibrium. A slight excess of spins occupies the lower-energy $\alpha$ state, while fewer spins remain in the higher-energy $\beta$ state. This population imbalance is small but crucial, as it gives rise to the net magnetization along the $z$-axis. The population ratio is governed by the Boltzmann distribution.

$$\frac{P_\beta}{P_\alpha} = e^{-\Delta E / k_B T} \tag{2.6}$$

where $P_\beta$ and $P_\alpha$ are the populations of the $\beta$ and $\alpha$ states with energy difference of $\Delta E$, $k_B$ is the Boltzmann constant, and $T$ is the absolute temperature, Fig 2.1. At room temperature and typical NMR fields, this imbalance is very small (polarizations on the order of $10^{-5}$ for protons), which explains the inherently low sensitivity of conventional NMR.

The observable NMR signal is proportional to the polarization (P), defined as:

$$P = \frac{P_\alpha - P_\beta}{P_\alpha + P_\beta} \tag{2.7}$$

Since $P_\alpha + P_\beta = 1$, Eq. (2.7) simplifies to

$$P = 1 - 2P_\beta \tag{2.8}$$

A spin ensemble usually tries to achieve thermal equilibrium by exchanging energy with the

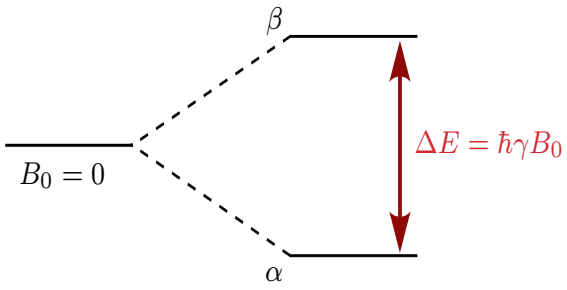


**Figure 2.1.:** Energy levels of a spin-1/2 system in the presence of an external magnetic field.

surrounding, which is called the "lattice". The time constant of the process is called the "spin-lattice" relaxation time constant, $T_1$. Physically, $T_1$ describes how quickly the longitudinal magnetization (along the $z$-axis) returns to its equilibrium value after being perturbed, for example by a radiofrequency pulse. After a few such $T_1$, the ensemble achieves the equilibrium with the lattice, and then the population ratio of these two states is given by Eq. (2.6). To further simplify this expression, we substitute the value of $\Delta E$:

$$\frac{P_\beta}{P_\alpha} = e^{-\gamma\hbar B_0/k_B T} \tag{2.9}$$

Solving the equation for $P_\beta$ gives

$$P_\beta = (1 - P_\beta)e^{-\gamma\hbar B_0/k_B T} \tag{2.10}$$

$$P_\beta = \frac{1}{1 + e^{\gamma\hbar B_0/k_B T}} \tag{2.11}$$

Substituting the $P_\beta$ values in the Eq. (2.8) gives the compact form:

$$P = \tanh\left(\frac{\gamma\hbar B_0}{2k_B T}\right) \tag{2.12}$$

In the high-temperature, low-field limit ( $\gamma\hbar B_0 \ll k_B T$ ), the hyperbolic tangent can be approximated as $\tanh(x) \approx x$, giving

$$P \approx \frac{\gamma\hbar B_0}{2k_B T}$$

Under typical NMR conditions (room temperature, magnetic fields up to 20 T), the polarization of spin-1/2 nuclei is therefore extremely small, on the order of $10^{-5}$.

For electrons, the gyromagnetic ratio is about 660 times larger than that of protons, leading to much higher polarization at the same $B_0$ and $T$. At cryogenic temperatures ($\sim$ 1 K), electron spins are essentially fully polarized, as illustrated in Fig 2.2. This stark difference underlies the principle of Dynamic Nuclear Polarization (DNP), where the spin order of electrons is transferred to nuclei to enhance NMR sensitivity. This will be explained in more detail in later sections.

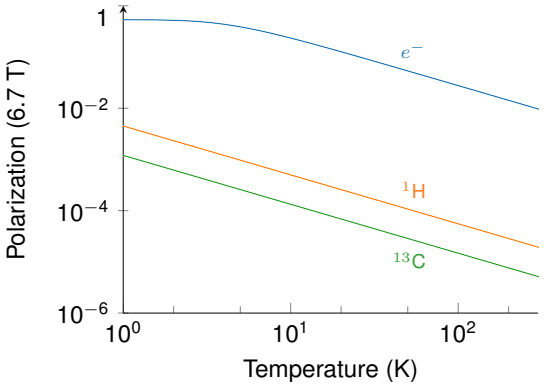


**Figure 2.2.:** Thermal equilibrium polarization for the electron (blue), $^1$H (orange), and $^{13}$C (green) at a magnetic field of 6.7 T with varying temperature from 1 to 300 K. Python code for this is provided in Appendix A.1.

### 2.1.4. Bloch Equations

The net magnetic moment of a spin ensemble can be represented as a vector rotating in real three-dimensional space. Fig 2.3 illustrates this "vector model" of NMR. At thermal equilibrium, the magnetization vector points along the $z$-axis, representing the longitudinal magnetization. Application of a radiofrequency pulse rotates the magnetization into the $xy$-plane, representing "transverse" magnetization. It precesses freely around the magnetic field axis at the Larmor frequency, shown in Fig 2.3

In 1946, Felix Bloch explained this magnetization vector rotation [6]. His approach involved treating the system of linear differential equations describing the time evolution of magnetization along an axis in the presence of the orthogonal magnetic field.

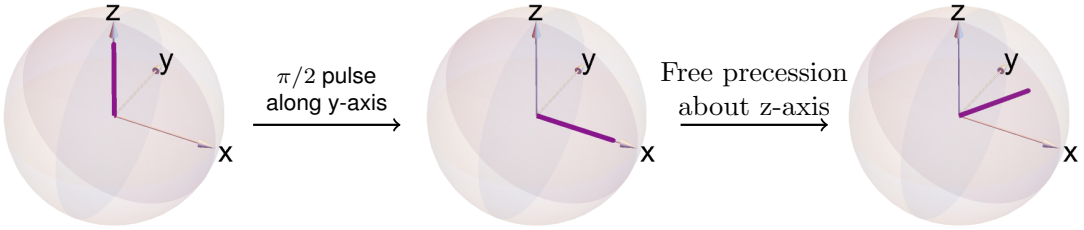


**Figure 2.3.:** The net magnetization vector (in purple) undergoes a hypothetical sequence: a $\pi/2$ pulse rotates the magnetization vector around the y-axis, followed by free precession of the spins around the z-axis. This figure has been produced using spinDynamica, and the corresponding code is provided in the Appendix A.2:

The equations below are known as Bloch equations:

$$\frac{dM_x(t)}{dt} = \gamma(B_z(t)M_y(t) - B_y(t)M_z(t)) - \frac{M_x(t)}{T_2}, \tag{2.13}$$

$$\frac{dM_y(t)}{dt} = \gamma(B_x(t)M_z(t) - B_z(t)M_x(t)) - \frac{M_y(t)}{T_2}, \tag{2.14}$$

$$\frac{dM_z(t)}{dt} = \gamma(B_y(t)M_x(t) - B_x(t)M_y(t)) - \frac{M_z(t) - M_0}{T_1}, \tag{2.15}$$

$B_k$ is the magnetic field along the k-axis, $M_k$ is the magnetization vector along that axis, and $\gamma$ is

the gyromagnetic ratio of the nuclear spin. $T_1$ and $T_2$ are the relaxation time constants. In NMR, the magnetic field is static along one axis, and we choose this axis to be the $z$-axis, which implies:

$$\frac{dM_x(t)}{dt} = \gamma B_0(t) M_y(t) - \frac{M_x(t)}{T_2} \tag{2.16}$$

$$\frac{dM_y(t)}{dt} = -\gamma B_0(t) M_x(t) - \frac{M_y(t)}{T_2} \tag{2.17}$$

$$\frac{dM_z(t)}{dt} = -\frac{M_z(t) - M_0}{T_1} \tag{2.18}$$

The solution of these equations are as follows. For constant $B_0$ define $\omega_0 = \gamma B_0$. With initial values $M_x(0), M_y(0), M_z(0)$, the solutions are:

$$M_x(t) = e^{-t/T_2}\Big[\, M_x(0)\cos(\omega_0 t) + M_y(0)\sin(\omega_0 t)\,\Big], \tag{2.19}$$

$$M_y(t) = e^{-t/T_2}\Big[\, M_y(0)\cos(\omega_0 t) - M_x(0)\sin(\omega_0 t)\,\Big], \tag{2.20}$$

$$M_z(t) = M_0 + \big(M_z(0) - M_0\big)\, e^{-t/T_1} \tag{2.21}$$

In summary, the solutions of the Bloch equations describe the precessional motion of transverse magnetization with an exponential decay governed by $T_2$ and the exponential recovery of longitudinal magnetization toward its thermal equilibrium value $M_0$ with a time constant $T_1$. These two relaxation processes form the basis for understanding signal decay and recovery in NMR experiments.

## 2.2. NMR Signal

The NMR signal originates from the transverse magnetization of an ensemble of nuclear spins. The bulk equilibrium magnetization in the high-temperature limit is given by Curie's law [7]:

$$M = \frac{n\gamma^2\hbar^2 B_0 I(I+1)}{3k_B T}, \tag{2.22}$$

where $n = N/V$ is the spin density, $\gamma$ the gyromagnetic ratio, and $B_0$ the static magnetic field. After a $\pi/2$ pulse, the longitudinal magnetization is tipped into the transverse plane and precesses at the Larmor frequency. According to Faraday's law of induction, the voltage induced in a coil with $N$ turns due to the changing magnetic flux $\phi$ is:

$$V_s = -N\frac{d\phi}{dt} \tag{2.23}$$

Here, $\phi$ is the magnetic flux through the coil. For a simple illustration, if the transverse magnetization produces a flux density $B = \mu_0 M$ over a coil area $A$, then

$$V_s = -NA\mu_0\omega M_z \cos(\omega t), \tag{2.24}$$

This expression emphasizes the proportionality between the induced signal and both the number of turns and the magnetization. While this might encourage us to use many turns, the coil's geometry also affects the noise level.

According to the principle of reciprocity, if a given current at a certain point in space generates a larger magnetic field, then a precessing moment at that point will induce a larger voltage in the same coil [8]. Then the induced voltage ($V$) for all magnetic moments, in a volume can be described as:

$$V = -\frac{d}{dt}\frac{1}{I}\iiint B.M\, dV \tag{2.25}$$

Using the same principle, the coil that detects the signal can also generate an RF field to excite the spins. The strength of the $B_1$ field generated for a given circuit is[9, 10] :

$$B_1 = \sqrt{\frac{\mu_0 QP}{2\omega V_c}} \tag{2.26}$$

In this equation, $\mu_0$ represents the permeability of free space, which relates currents and magnetic field in a vacuum. The variable $P$ denotes the rf power supplied to the circuit, and $\omega$ is the angular frequency of the circuit within the coil volume $V_c$. The quality factor of the circuit is defined by $Q$, which is readily measured by the width of the return loss spectrum 7 dB below the baseline[11]. The electrons in the coil wire also generate a noise voltage called "Nyquist noise" [12] which is given by:

$$V_N = \sqrt{4k_B TR\Delta f} \tag{2.27}$$

The term $\Delta f$ refers to the bandwidth over which noise is measured at the coil's temperature $T$ and resistance $R$. By lowering the temperature of the coil, we can effectively reduce the noise. For this reason, cryoprobes can achieve up to a 4-fold increase in the signal-to-noise ratio (SNR)[13].

Under real experimental conditions, the SNR tends to be lower than the value calculated theoretically due to additional noise from the preamplifiers. The SNR can be increased by averaging more than one scan. The SNR is directly proportional to the square root of the number of scans during acquisition. These scans can take a significant amount of time for low-concentration and small gyromagnetic ratio nuclei at low field. One way to increase SNR is hyperpolarization, which will be discussed in the next chapter.

### 2.2.1. NMR Spectrum

To illustrate how the nuclear spin magnetization can produce the NMR spectrum of a sample in the presence of a magnetic field. The case of uncoupled nuclear spins is considered. A $\pi/2$ pulse is applied along the x-axis, followed by acquisition of the signal. During the pulse, the spins precess in the effective field of the rotating frame, and for sufficiently short pulse durations, the action of the pulse can be approximated as an instantaneous rotation of the magnetization vector. After the pulse, the transverse magnetization precesses about the static magnetic field at its Larmor frequency $\omega_0$ and relaxes back to thermal equilibrium.

The precessing transverse magnetization induces a time-dependent voltage in the detection coil. This signal, once amplified, is referred to as the "free induction decay" (FID). A typical FID contains a superposition of exponentially decaying oscillations from different spins, together with noise and artifacts, which makes direct inspection in the time domain difficult.

To connect the generated voltage to transition energies and the chemical environment, the

signal must be transformed from the time domain to the frequency domain. The frequency domain spectrum can be defined theoretically using the continuous Fourier transformation and written as:

$$f(\omega) = \int_{-\infty}^{\infty} f(t)\, e^{i\omega t}\, dt \tag{2.28}$$

In this expression, $f(t)$ represents the complex NMR free induction decay (FID) acquired in the rotating frame. Since actual NMR signals are sampled at discrete time points over a finite acquisition period, the spectrum is practically calculated using a discrete Fourier transform (DFT), usually implemented through a fast Fourier transform (FFT) algorithm. The real and imaginary parts of $f(\omega)$ are not simply the cosine and sine transforms of a real-valued signal, but rather combinations of contributions from both the real and imaginary parts of $f(t)$. These components correspond to the absorption and dispersion spectra, which can be analyzed in terms of the spectral density function $J_{\omega_0}$.

### 2.2.2. Digitization and Sampling of the NMR Signal

The analogue-to-digital converter (ADC) digitizes the induced voltage into binary form for storage and processing. It samples the FID at regular intervals and quantizes the amplitude into discrete levels determined by its bit depth. For example, a 3-bit ADC provides $2^3 = 8$ levels (000, 001, 010, 011, 100, 101, 110, 111). Increasing the number of bits improves accuracy; currently, ADCs with 16 to 32 bits are standard in NMR spectrometers, although technical limitations restrict further increases.

Because the NMR signal oscillates at high frequencies (10 to 1000 MHz), most spectrometers first mix it down to an intermediate frequency before digitization. This allows accurate capture using standard ADCs without requiring extremely high sampling rates. The sampling rate defines the time interval between data points, known as dwell time ($\Delta$). According to the Nyquist criterion, the sampling frequency needs to be at least twice the highest frequency in the signal to prevent aliasing.

$$\Delta = \frac{1}{2f_{\text{max}}}, \tag{2.29}$$

where $f_{\text{max}}$ is the "Nyquist frequency" and $\Delta$ include frequencies range from - $f_{\text{max}}$ to + $f_{\text{max}}$.

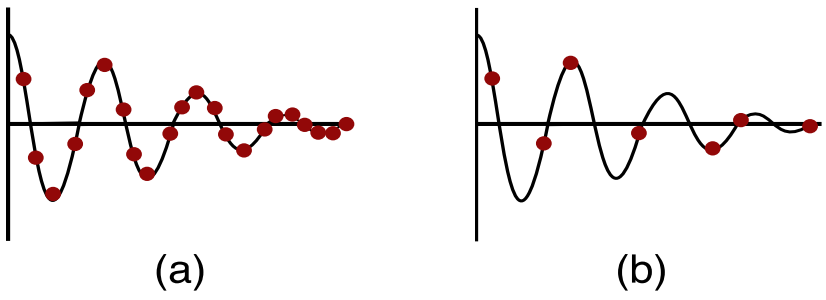


**Figure 2.4.:** Illustration of how sampling rate affects the representation of the FID signal. In (a), the high sampling rate (red dots) closely follows the continuous line, providing a good representation of the signal. In contrast, (b) shows a low sampling rate where the widely spaced data points show poor signal representation.

So far, the discussion has covered the various factors influencing the NMR signal, such as precession, FID acquisition, and digitization, which all need careful consideration during an experiment. To fully understand the measured signal, it is necessary to consider the quantum mechanical behavior of nuclear spins. The following section presents a quantum mechanical description of NMR, providing insight into relaxation processes and their influence on the observed signal.

## 2.3. Quantum Description

Quantum mechanics provides a framework to describe a particle's state, including nuclear spin, and to predict the time evolution of these states. The state of a spin ensemble can be represented by the density operator $\rho$. This formalism allows quantitative predictions of NMR observables and has been confirmed by all experiments to date.

### 2.3.1. Hilbert Space and Eigen-states

In a complex, $N$-dimensional Hilbert space, a "ket" $|\psi\rangle$ represents a quantum state and corresponds to a vector as per Dirac notation. For a spin-1/2, the $|\alpha\rangle$ and $|\beta\rangle$ kets are the "Zeeman basis" of this Hilbert space and represented as:

$$|\alpha\rangle = \begin{bmatrix} 1 \\ 0 \end{bmatrix}, \quad |\beta\rangle = \begin{bmatrix} 0 \\ 1 \end{bmatrix} \tag{2.30}$$

In a magnetic field, the possible energy states with $m_I = \pm 1/2$ are represented as $|I, m_I\rangle$. The spin can exist in either of these states or as a linear combination of the two.

$$|\psi\rangle = C_1 |\alpha\rangle + C_2 |\beta\rangle = \begin{bmatrix} C_1 \\ C_2 \end{bmatrix} \tag{2.31}$$

The "ket" can be easily transformed to "bra" in a dual vector space by taking the conjugate transpose of the corresponding ket, such that:

$$\langle\psi| = C_1^*\langle\alpha| + C_2^*\langle\beta| = \begin{bmatrix} C_1^* & C_2^* \end{bmatrix} \tag{2.32}$$

The spin states form an orthonormal basis, which implies that:

$$\langle\alpha|\alpha\rangle = \langle\beta|\beta\rangle = 1 \tag{2.33}$$

$$\langle\alpha|\beta\rangle = \langle\beta|\alpha\rangle = 0 \tag{2.34}$$

The matrix representation of the three angular momentum operators in Zeeman eigenbasis $|\alpha\rangle$, $|\beta\rangle$ is given by Pauli spin matrices.

$$I_z = \frac{1}{2}\begin{bmatrix} 1 & 0 \\ 0 & -1 \end{bmatrix}, \quad I_x = \frac{1}{2}\begin{bmatrix} 0 & 1 \\ 1 & 0 \end{bmatrix}, \quad I_y = \frac{1}{2i}\begin{bmatrix} 0 & 1 \\ -1 & 0 \end{bmatrix}. \tag{2.35}$$

For a spin-1/2 system, the eigenstates of $I_z$ are conventionally denoted as follows:

$$|\alpha\rangle = \begin{bmatrix} 1 \\ 0 \end{bmatrix}, \quad m_I = +\frac{1}{2}, \qquad |\beta\rangle = \begin{bmatrix} 0 \\ 1 \end{bmatrix}, \quad m_I = -\frac{1}{2} \tag{2.36}$$

Applying the $I_z$ operator to these states gives the corresponding eigenvalues:

$$I_z|\alpha\rangle = \frac{1}{2}|\alpha\rangle, \quad I_z|\beta\rangle = -\frac{1}{2}|\beta\rangle \tag{2.37}$$

Thus, $|\alpha\rangle$ and $|\beta\rangle$ are eigenstates of $I_z$ with eigenvalues $m_I = \pm 1/2$, corresponding to the spin projections along the $z$-axis. Having defined the spin states in Hilbert space, we can now represent measurable quantities as operators acting on these states. Apart from Pauli spin matrices, additional operators are useful for defining the change in spin state. These are called shift operators and act in the following way:

$$I^+ |I, m_I\rangle = \sqrt{I(I+1) - m_I(m_I+1)}\, |I, m_I + 1\rangle \tag{2.38}$$

$$I^- |I, m_I\rangle = \sqrt{I(I+1) - m_I(m_I-1)}\, |I, m_I - 1\rangle \tag{2.39}$$

Here, $I^+$ is the "raising" operator, and $I^-$ is the "lowering" operator. When $I^+$ is applied to $|\beta\rangle$, it transforms to the state $|\alpha\rangle$, but the reverse is not possible.

$$I^+|\alpha\rangle = 0, \quad I^+|\beta\rangle = |\alpha\rangle, \quad I^-|\alpha\rangle = |\beta\rangle, \quad I^-|\beta\rangle = 0 \tag{2.40}$$

Using these $I^+$ can be written as:

$$I^+ = \begin{bmatrix} \langle\alpha|0\rangle & \langle\alpha|\alpha\rangle \\ \langle\beta|0\rangle & \langle\beta|\alpha\rangle \end{bmatrix} = \begin{bmatrix} 0 & 1 \\ 0 & 0 \end{bmatrix} \tag{2.41}$$

The $I^-$ can be calculated by using same operators.

$$I^- = \begin{bmatrix} \langle\alpha|I^-|\alpha\rangle & \langle\alpha|I^-|\beta\rangle \\ \langle\beta|I^-|\alpha\rangle & \langle\beta|I^-|\beta\rangle \end{bmatrix} = \begin{bmatrix} 0 & 0 \\ 1 & 0 \end{bmatrix} \tag{2.42}$$

Any physically measurable quantity in quantum mechanics is represented by a Hermitian operator, i.e. $\hat{A}^\dagger = \hat{A}$, while rotations are represented by unitary operators, which satisfy $\hat{U}\hat{U}^\dagger = \mathbb{I}$, where $\mathbb{I}$ is the identity operator.

The unitary operator, when combined with $\vec{I}_z$ give new projection operators $I^\alpha$ and $I^\beta$, which are also referred as "polarization operators".

$$I^\alpha = \frac{1}{2}\left(\hat{\mathbf{1}} + \hat{I}_z\right), \quad I^\beta = \frac{1}{2}\left(\hat{\mathbf{1}} - \hat{I}_z\right) \tag{2.43}$$

These operators have the properties:

$$I^\alpha|\alpha\rangle = |\alpha\rangle, \quad I^\beta|\alpha\rangle = 0, \tag{2.44}$$

$$I^\alpha|\beta\rangle = 0, \quad I^\beta|\beta\rangle = |\beta\rangle \tag{2.45}$$

The matrix representations are as follows:

$$\hat{I}^\alpha = \begin{bmatrix} 1 & 0 \\ 0 & 0 \end{bmatrix}, \quad \hat{I}^\beta = \begin{bmatrix} 0 & 0 \\ 0 & 1 \end{bmatrix} \tag{2.46}$$

In ket-bra notation, the projection and shift operators can be expressed as follows:

$$\hat{I}^\alpha = |\alpha\rangle\langle\alpha|, \quad \hat{I}^\beta = |\beta\rangle\langle\beta|, \tag{2.47}$$

$$\hat{I}^+ = |\alpha\rangle\langle\beta|, \quad \hat{I}^- = |\beta\rangle\langle\alpha| \tag{2.48}$$

These notations are very useful to express Pauli spin matrices in terms of energy states.

$$\hat{I}_x = \frac{1}{2}\left(\hat{I}^+ + \hat{I}^-\right) = \frac{1}{2}\left(|\alpha\rangle\langle\beta| + |\beta\rangle\langle\alpha|\right), \tag{2.49}$$

$$\hat{I}_y = \frac{1}{2i}\left(\hat{I}^+ - \hat{I}^-\right) = \frac{1}{2i}\left(|\alpha\rangle\langle\beta| - |\beta\rangle\langle\alpha|\right), \tag{2.50}$$

$$\hat{I}_z = \frac{1}{2}\left(\hat{I}^\alpha - \hat{I}^\beta\right) = \frac{1}{2}\left(|\alpha\rangle\langle\alpha| - |\beta\rangle\langle\beta|\right), \tag{2.51}$$

$$\frac{1}{2}\hat{1} = \frac{1}{2}\left(\hat{I}^\alpha + \hat{I}^\beta\right) = \frac{1}{2}\left(|\alpha\rangle\langle\alpha| + |\beta\rangle\langle\beta|\right) \tag{2.52}$$

To predict measurable quantities and the outcomes of NMR experiments, operators and their corresponding expectation values are introduced.

### 2.3.2. Operators and Expectation Values

Spin angular momentum operators obey cyclic commutation relationships, and their complex exponentials are referred to as "rotation operators". These operators, when applied to Cartesian axes, are represented as follows:

$$R_x(\theta) = \exp\left(-i\theta\hat{I}_x\right) \tag{2.53}$$

$$R_y(\theta) = \exp\left(-i\theta\hat{I}_y\right) \tag{2.54}$$

$$R_z(\theta) = \exp\left(-i\theta\hat{I}_z\right) \tag{2.55}$$

These can be applied to the angular momentum operators using the "sandwich" formula. The result is a rotation of $\hat{I}_x$ by an angle $\theta$ around the $z$-axis of the system.

$$\hat{R}_z(\theta)\,\hat{I}_x = \cos(\theta)\,\hat{I}_x + \sin(\theta)\,\hat{I}_y \tag{2.56}$$

Here, $\theta$ represents the angle of rotation. If we apply the $R_x(\pi/2)$ operator, it will rotate an object about the x-axis by an angle of $\pi/2$. To predict outcomes, we calculate the expectation value, which reflects the experimental results. Let us consider the function $|\psi\rangle$ representing the state of the system.

$$|\psi\rangle = C_\alpha|\alpha\rangle + C_\beta|\beta\rangle \tag{2.57}$$

The state of an ensemble of spins in a system is defined by the density operator.

$$\hat{\rho} = |\psi\rangle\langle\psi| = \begin{array}{c} \\ \langle\alpha| \\ \langle\beta| \end{array} \begin{array}{c} \begin{array}{cc} |\alpha\rangle & |\beta\rangle \end{array} \\ \begin{bmatrix} C_\alpha^* C_\alpha & C_\beta^* C_\alpha \\ C_\beta^* C_\alpha & C_\beta^* C_\beta \end{bmatrix} \end{array} \tag{2.58}$$

The diagonal elements of the density operator $\rho$ represent "state populations," while the off-diagonal elements indicate "coherences" between states. The expectation value of any spin operator $\hat{O}$ is calculated as below:

$$\langle\hat{O}\rangle = \mathrm{Tr}(\rho\hat{O}), \tag{2.59}$$

where Tr denotes the trace of the matrix. For a spin-1/2 particle, the $I_x$ operator is:

$$\hat{I}_x = \frac{1}{2}\begin{bmatrix} 0 & 1 \\ 1 & 0 \end{bmatrix} \tag{2.60}$$

Consider the system in the pure state $|\alpha\rangle$, represented by the density operator.

$$\rho = |\alpha\rangle\langle\alpha| = \begin{bmatrix}1\\0\end{bmatrix}\begin{bmatrix}1 & 0\end{bmatrix} = \begin{bmatrix}1 & 0\\0 & 0\end{bmatrix} \tag{2.61}$$

The expectation value of $I_x$ is then

$$\begin{aligned}\langle I_x\rangle &= \mathrm{Tr}(\rho\hat{I}_x)\\ &= \mathrm{Tr}\left(\begin{bmatrix}1 & 0\\0 & 0\end{bmatrix}\frac{1}{2}\begin{bmatrix}0 & 1\\1 & 0\end{bmatrix}\right) = 0\end{aligned} \tag{2.62}$$

This shows that in the $|\alpha\rangle$ state, the expectation value of $I_x$ is zero. Similarly, the expectation value of $I_z$ is:

$$\begin{aligned}\langle I_z\rangle &= \mathrm{Tr}(\rho\hat{I}_z)\\ &= \mathrm{Tr}\left(\begin{bmatrix}1 & 0\\0 & 0\end{bmatrix}\frac{1}{2}\begin{bmatrix}1 & 0\\0 & -1\end{bmatrix}\right) = \frac{1}{2}\end{aligned} \tag{2.63}$$

Thus, in the $|\alpha\rangle$ state, the transverse components $I_x$ and $I_y$ average to zero, while the longitudinal component maintains a finite value of $+1/2$, reflecting the spin-1/2 projection along the $z$-axis. In summary, the expectation values connect the abstract operator formalism to observable spin states. Next, we examine the eigenvalues and eigenvectors of spin operators.

### 2.3.3. Eigenvalues and vectors

Hermitian operators correspond to measurable quantities in quantum mechanics, and their eigenvalues are always real. To illustrate this, we can compute the eigenvalues of the operator $I_x$ for spin-1/2 using the characteristic equation.

$$|\, I_x - \lambda I\,| = 0 \tag{2.64}$$

$$\left|\frac{1}{2}\begin{bmatrix}0 & 1\\1 & 0\end{bmatrix} - \lambda\begin{bmatrix}1 & 0\\0 & 1\end{bmatrix}\right| = 0 \tag{2.65}$$

Solving Eq. (2.65) for $\lambda$ we will get, $\lambda = \pm 1/2$ which are the real eigenvalues of $I_x$. Using these values, we can determine the corresponding eigenvectors in its orthonormal eigenbasis as follows:

$$|V_1\rangle = \frac{1}{\sqrt{2}}\begin{bmatrix}1\\1\end{bmatrix}, \quad |V_2\rangle = \frac{1}{\sqrt{2}}\begin{bmatrix}1\\-1\end{bmatrix} \tag{2.66}$$

From Eq. (2.66), the corresponding bra vector can be expressed as:

$$\langle V_1| = \frac{1}{\sqrt{2}}\begin{bmatrix}1 & 1\end{bmatrix}, \quad \langle V_2| = \frac{1}{\sqrt{2}}\begin{bmatrix}1 & -1\end{bmatrix} \tag{2.67}$$

The eigenvectors of a Hermitian operator form an orthonormal basis; the operator $I_x$ can be represented in terms of this basis as follows:

$$I_x = \begin{bmatrix}\langle V_1|I_x|V_1\rangle & \langle V_1|I_x|V_2\rangle\\ \langle V_2|I_x|V_1\rangle & \langle V_2|I_x|V_2\rangle\end{bmatrix} \tag{2.68}$$

Upon solving Eq. (2.68), we get Eq. (2.69). In this equation, $I_x$ is expressed in the basis of its own eigenket vectors ($\lambda = \pm 1/2$). The diagonal elements correspond to the eigenkets of $|V_1\rangle$ and $|V_2\rangle$.

$$I_x = \frac{1}{2}\begin{bmatrix} 1 & 0 \\ 0 & -1 \end{bmatrix} \tag{2.69}$$

### 2.3.4. Liouville-von Neumann equation

The time evolution of the state vector $|\psi(t)\rangle$ follows the Schrödinger equation.

$$i\hbar\frac{d|\psi(t)\rangle}{dt} = \hat{H}|\psi(t)\rangle \tag{2.70}$$

In this context, the symbol $\hat{H}$ denotes the "Hamiltonian operator", which corresponds to the total energy. If $|\psi_\alpha\rangle$ and $|\psi_\beta\rangle$ are eigenstates of the Hamiltonian $\hat{H}$ then,

$$\hat{H}|\psi_\alpha\rangle = E_\alpha|\psi_\alpha\rangle \tag{2.71}$$

$$\hat{H}|\psi_\beta\rangle = E_\beta|\psi_\beta\rangle \tag{2.72}$$

where $E_\alpha$ is the energy eigenvalue corresponding to the state $|\psi_\alpha\rangle$, and $E_\beta$ is the energy eigenvalue corresponding to the state $|\psi_\beta\rangle$. In matrix representation, the diagonal entries correspond to the state energies when the Hamiltonian is expressed in the eigenbasis.

$$\hat{H} = \begin{array}{c} \\ \langle\psi_\alpha| \\ \langle\psi_\beta| \end{array} \begin{array}{c} \begin{array}{cc} |\psi_\alpha\rangle & |\psi_\beta\rangle \end{array} \\ \begin{bmatrix} E_\alpha & 0 \\ 0 & E_\beta \end{bmatrix} \end{array} \tag{2.73}$$

The density operator for a pure state $|\psi\rangle = c_\alpha|\psi_\alpha\rangle + c_\beta|\psi_\beta\rangle$ is:

$$\hat{\rho} = |\psi\rangle\langle\psi| = \begin{bmatrix} C_\alpha C_\alpha^* & C_\alpha C_\beta^* \\ C_\beta C_\alpha^* & C_\beta C_\beta^* \end{bmatrix} \tag{2.74}$$

The dynamics of a spin system can be understood by using the evolution of the density operator rather than states, as follows:

$$\frac{\partial}{\partial t}\hat{\rho} = \frac{\partial}{\partial t}\left(|\psi\rangle\langle\psi|\right) \tag{2.75}$$

$$\frac{\partial}{\partial t}\hat{\rho} = \left(\frac{\partial}{\partial t}|\psi\rangle\right)\langle\psi| + |\psi\rangle\left(\frac{\partial}{\partial t}\langle\psi|\right) \tag{2.76}$$

$$\frac{\partial}{\partial t}|\psi\rangle = -i\hat{H}|\psi\rangle, \quad \frac{\partial}{\partial t}\langle\psi| = i\langle\psi|\hat{H} \tag{2.77}$$

By substitiing Eq. (2.77) in Eq. (2.76) we will get:

$$\begin{aligned} \frac{\partial}{\partial t}\hat{\rho} &= -i\hat{H}|\psi\rangle\langle\psi| + i|\psi\rangle\langle\psi|\hat{H} \\ &= -i\hat{H}\hat{\rho} + i\hat{\rho}\hat{H} = -i[\hat{H},\hat{\rho}] \end{aligned} \tag{2.78}$$

where the commutator is defined as:

$$[\hat{H},\hat{\rho}] = \hat{H}\hat{\rho} - \hat{\rho}\hat{H} \tag{2.79}$$

This is called the "Liouville-von Neumann" equation. The density operator evolves under a Hamiltonian as follows:

$$\hat{\rho}(t) = e^{-i\hat{H}t}\,\hat{\rho}(0)e^{i\hat{H}t} \tag{2.80}$$

The evolution of the density operator $I_x$ i.e $\hat{\rho}(0) = I_x$ under the Hamiltonian $\hat{H} = \omega\hat{I}_z$ is calculated as follows.

$$\hat{\rho}(t) = e^{-i\omega t\hat{I}_z}\,\hat{I}_x\,e^{i\omega t\hat{I}_z} = \cos(\omega t)\,\hat{I}_x + \sin(\omega t)\,\hat{I}_y \tag{2.81}$$

This evolution is only possible if $[\hat{H}, \hat{\rho}] \neq 0$, and there will be no evolution if $[\hat{H}, \hat{\rho}] = 0$

So far, we have described the coherent evolution of spin systems under a Hamiltonian. In practice, however, spins interact with their environment, leading to a gradual loss of coherence and energy redistribution. These processes are known as "spin relaxation".

## 2.4. Relaxation in NMR

There are two main relaxation processes: longitudinal relaxation ($T_1$), which describes how magnetization returns to the z-axis after a pulse, and transverse relaxation ($T_2$), which governs the return of the magnetization vector to equilibrium from the xy-plane. The theory is mainly based on Ref [4].

To develop an intuitive understanding of relaxation, a simple model is considered: a spin-1/2 nucleus in a static magnetic field $B_0$ (aligned with the z-axis) that is perturbed by a small, randomly fluctuating magnetic field $B_x$(t) along the x-axis. While $B_0$ is constant and identical for all spins, the transverse field $B_x$(t) fluctuates in time and varies from spin to spin. To characterize such a random field, we adopt the following assumptions.

1. The fluctuating field average is zero.

$$\langle B_x(t)\rangle = 0 \tag{2.82}$$

2. Since the average of the field is zero, it indicates that we cannot determine magnitude based on the average; instead, we calculate it using the mean square of the fluctuating field, which is non-zero and always positive, as shown below.

$$\langle B_x^2(t)\rangle > 0 \tag{2.83}$$

3. The rate of field fluctuations can be quantified by the autocorrelation function, which is defined as follows:

$$G(\tau) = \langle B_x(t)B_x(t+\tau)\rangle \neq 0 \tag{2.84}$$

Here, $\tau$ represents the decay time interval of the autocorrelation function for the fluctuating field. If $\tau$ = 0, then this function can be written as:

$$G(0) = \langle B_x^2(t)\rangle \tag{2.85}$$

4. The autocorrelation function is independent of the absolute time $t$, depending only on the delay $\tau$.

5. For primarily qualitative analysis, the fluctuating fields are assumed independent of the spin orientation and unaffected by the neighbouring spin. However, this assumption fails for relaxation

mechanisms such as dipole-dipole coupling.

This function makes a comparison of the value of the field at time $t$ and $(t + \tau)$. It is highly dependent on the $\tau$ value. If $B_x$(t) is positive, then $B_x$ $(t + \tau)$ will also likely be positive for small values of $\tau$, and the same holds for negative values.

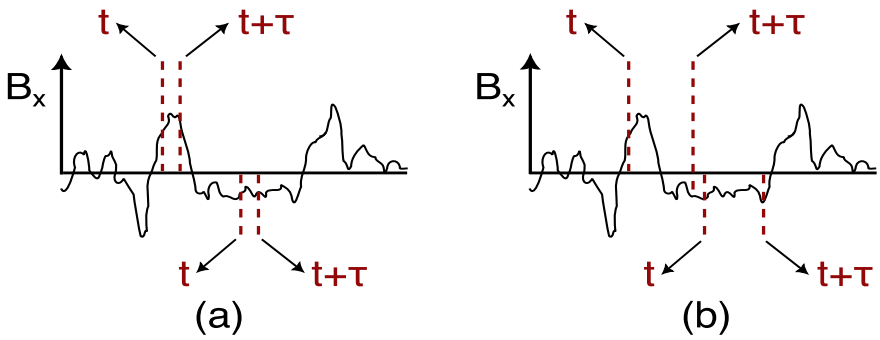


**Figure 2.5.:** Illustration of fluctuating rate of transverse $B_x$ field. In (a), comparison of fluctuating rates at close time intervals and (b) at the long time interval $\tau$.

As a result, the product of these two values will likely be positive and closely related to $\langle B_x^2(t)\rangle$ as shown in Fig. 2.5 (a). In contrast, the statement may not hold for large values of $\tau$ as shown in (b). In this case, the value of $B_x$ is positive at time $t$ but more likely to be negative at $(t + \tau)$. Consequently, the average of the ensemble of spins will now correspond to zero.

Physically, $G(\tau)$ compares the value of the random field at time $t$ and at $t + \tau$. For short $\tau$, the two values are similar, giving a positive product, while at longer delays the correlation is lost, leading to $G(\tau) \longrightarrow 0$ (Fig. 2.5). A common model assumes an exponential decay:

$$G(\tau) = \langle B_x^2(t)\rangle e^{-|\tau|/\tau_c} \tag{2.86}$$

Here $\tau_c$ is called the "molecular correlation time" of fluctuations. Smaller values of $\tau_c$ indicate rapid fluctuations, while larger values correspond to slower ones. This parameter represents the time required for a random field to change its sign and is influenced by various physical parameters, including temperature. For a rotating molecule in a liquid, $\tau_c$ typically ranges from tens of picoseconds to nanoseconds.

With this foundation, the spectral density function is introduced, which directly connects these field fluctuations to relaxation rate constants.

### 2.4.1. Spectral Density function

The spectral density $J(\omega)$ describes how the strength of field fluctuations is distributed over different frequencies. It is defined as twice the Fourier transform of the autocorrelation function.

$$J(\omega) = 2\int_0^\infty G(\tau)\, e^{-i\omega t}\, d\tau \tag{2.87}$$

The spectral density function can be written as follows for a fluctuating field along the $x$-axis, by substituting values from Eq. (2.86)

$$J(\omega) = 2\,\langle B_x^2(t)\rangle \frac{\tau_c}{1 + \omega^2\tau_c^2} \tag{2.88}$$

This is a Lorentzian function, where the width is determined by the correlation time $\tau_c$. For rapidly fluctuating fields (short $\tau_c$), $J(\omega)$ is broad, while for slow fluctuations (long $\tau_c$) the function is narrow. Nevertheless, the area under the curve remains constant in both cases and is given by $\langle B_x^2 \rangle$, independent of $\tau_c$.

### 2.4.2. Transition Probabilities

The fluctuating transverse field induces transitions between spin eigenstates $|\,\alpha\,\rangle$ and $|\,\beta\,\rangle$. If a spin starts in state $|\,\alpha\,\rangle$ at time $t$, it evolves to $|\,\alpha'\,\rangle$ at time $(t+\tau)$, often corresponding to superposition of $|\,\alpha\,\rangle$ and $|\,\beta\,\rangle$. Consequently, further measurements may yield outcomes to $|\,\beta\,\rangle$. The probability of transitioning from $|\,\alpha\,\rangle$ to $|\,\beta\,\rangle$ and $|\,\beta\,\rangle$ to $|\,\alpha\,\rangle$ is:

$$\begin{aligned} W_{\boxed{-}} &= \tau^{-1}\overline{|\langle\beta|\alpha'\rangle|^2} \\ W_{\boxed{+}} &= \tau^{-1}\overline{|\langle\alpha|\beta'\rangle|^2} \end{aligned} \tag{2.89}$$

Here $W_{\boxed{-}}$ describes the transition from $|\,\alpha\,\rangle$ to $|\,\beta\,\rangle$ (a decrease in spin angular momentum along the $z$-axis), while $W_{\boxed{+}}$ represents the reverse process. The overbar denotes the ensemble average.

For nuclei with $\gamma > 0$, the energy of the state $|\,\beta\,\rangle$ will be higher than that of the state $|\,\alpha\,\rangle$. To establish the Boltzmann distribution, the probability of transition $W_{\boxed{+}}$ from $|\,\beta\,\rangle$ to $|\,\alpha\,\rangle$ must be greater than the probability $W_{\boxed{-}}$ for the transition from $|\,\alpha\,\rangle$ to $|\,\beta\,\rangle$. Under equilibrium conditions, the flow of populations in both directions should be equal.

$$\rho_\alpha^{\mathrm{eq}}\, W_{\boxed{-}} = \rho_\beta^{\mathrm{eq}}\, W_{\boxed{+}} \tag{2.90}$$

Here $\rho_\alpha^{\mathrm{eq}}$ and $\rho_\beta^{\mathrm{eq}}$ are the thermal equillibribium populations, Fig. 2.6. Since the population difference is only on the order of $10^{-4}$, the transition probabilities differ only slightly.

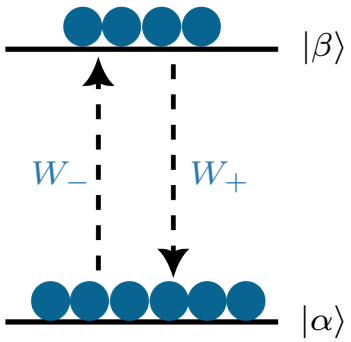


**Figure 2.6.:** Dynamic equilibrium of populations at thermal equilibrium.

The values of $W_{\boxed{+}}$ and $W_{\boxed{-}}$ can be expressed as:

$$W_{\boxed{-}} = W\left(1 - \frac{1}{2}B\right), \quad W_{\boxed{+}} = W\left(1 + \frac{1}{2}B\right) \tag{2.91}$$

The mean transition probability $W$ is:

$$W = \frac{1}{2}\gamma^2\langle B_x^2\rangle J(\omega_0) \tag{2.92}$$

### 2.4.3. Spin-Lattice Relaxation

A simple model, in which the nuclear spin interacts with random fluctuating magnetic fields, provides a useful starting point for describing spin-lattice relaxation. In this framework, the populations of the spin states change due to transition processes. For the state $|\,\alpha\,\rangle$, the kinetic equation for the population can be expressed as:

$$\frac{d}{dt}\rho_\alpha = -W_{\boxed{-}}\rho_\alpha + W_{\boxed{+}}\rho_\beta \tag{2.93}$$

and, correspondingly, for the state $|\,\beta\,\rangle$:

$$\frac{d}{dt}\rho_\beta = +W_{\boxed{-}}\rho_\alpha - W_{\boxed{+}}\rho_\beta \tag{2.94}$$

The spin magnetization vector along the $z$-axis is proportional to the difference in population between two states given by:

$$M_z = 2B^{-1}\left(\rho_\alpha - \rho_\beta\right) \tag{2.95}$$

And the $z$-component of the magnetization vector has the following equation of motion:

$$\frac{d}{dt}M_z = 2B^{-1}\left(\frac{d}{dt}\rho_\alpha - \frac{d}{dt}\rho_\beta\right) \tag{2.96}$$

$$= 4B^{-1}\left(-W_{\boxed{-}}\rho_\alpha + W_{\boxed{+}}\rho_\beta\right) \tag{2.97}$$

Substituting Eqs. (2.91) in (2.97) we get:

$$= 4B^{-1}\left(-W\left(1-\frac{1}{2}B\right)\rho_\alpha + W\left(1+\frac{1}{2}B\right)\rho_\beta\right) \tag{2.98}$$

$$= 4B^{-1}\left[-W\left(\rho_\alpha - \rho_\beta\right) + \frac{WB}{2}\left(\rho_\alpha + \rho_\beta\right)\right] \tag{2.99}$$

Then, by using the value $\rho_\alpha + \rho_\beta = 1$ and substituting $M_z$ values from (2.95)

$$\frac{d}{dt}M_z = -2W\left(M_z - 1\right) \tag{2.100}$$

By integrating this equation, we get:

$$M_z\left(\tau\right) = \left(M_z\left(0\right) - 1\right)e^{-2W\tau} + 1 \tag{2.101}$$

For this simple system, the spin-lattice relaxation rate constant is given by ($T_1^{-1} = 2\,W$), which is twice the mean transition probability between states. This relaxation rate constant for a fluctuating random field along the $x$-axis is given by:

$$T_1^{-1} = \gamma^2\left\langle B_x^2\right\rangle J(\omega_0) = \gamma^2\left\langle B_x^2\right\rangle \frac{\tau_c}{1+(\omega^0\tau_c)^2} \tag{2.102}$$

From Eq. (2.102) it is evident that $T_1^{-1}$ has a strong dependence on the external magnetic field $B_0$ (through Larmor frequency) as shown in Fig. 2.7

In this plot, the critical Larmor frequency ($\omega_{\text{crit}}$) is defined as the frequency at which the relaxation rate, $T_1^{-1}$, reaches its maximum for a given correlation time. The flat portion of the graph represents the region where the relaxation rate $T_1^{-1}$ is independent of the magnetic field, known as the "extreme narrowing" region when $\omega_0^2\,\tau_c^2 \ll 1$. Another key observation from the plot is that nuclei with a higher

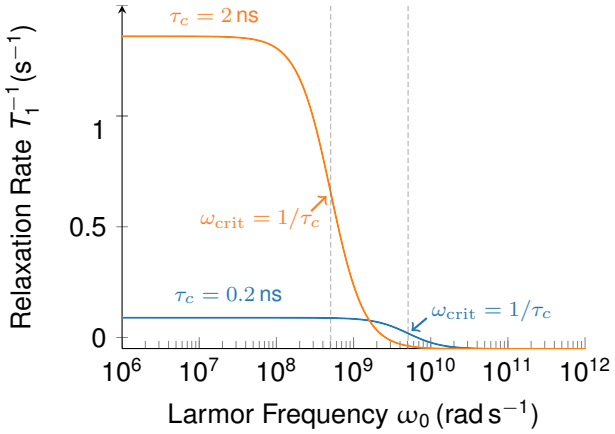


**Figure 2.7.:** Calculation of $T_1^{-1}$ for proton as a function of Larmor frequency for two $\tau_c$ values, $\tau_c = 0.2$ ns (Blue) and $\tau_c = 2$ ns shown in orange color. The mean value of the fluctuating field was assumed $\langle B_x^2 \rangle = 1^{-4}$ T, and the code for this calculation is in Appendix A.3 (code A.4).

gyromagnetic ratio, such as $^1$H, leave the extreme narrowing region at lower magnetic fields compared to other nuclei, like $^{13}$C and $^{15}$N.

The rotational correlation time significantly influences the $T_1^{-1}$, and is itself affected by factors such as solution viscosity, temperature, and molecular size. In 1948, Bloembergen, Purcell, and Pound proposed a theory that explains the effect of molecular tumbling on the local fluctuating field. Using the Stokes-Einstein-Debye relation, the correlation time ($\tau_c$) can be defined as follows:[14]

$$\tau_c = \frac{4\,\pi\,\eta\,a^3}{k_b\,T} = \frac{3\,V\,\eta}{k_b\,T} \tag{2.103}$$

Here, $\eta$ represents the viscosity of the solution, while $V$ denotes the volume of the molecule. Assuming the molecule is spherical with a radius of $a$, then $V = 4\,\pi\,a^3/3$. Consequently, $\tau_c$ is directly proportional to $a^3$, which means the molecular size. For instance, proteins with a higher molecular mass exhibit a larger value of $\tau_c$, resulting in slower molecular tumbling. The relationship between the relaxation rate $T_1^{-1}$ on $\tau_c$ is shown below in Fig. 2.8:

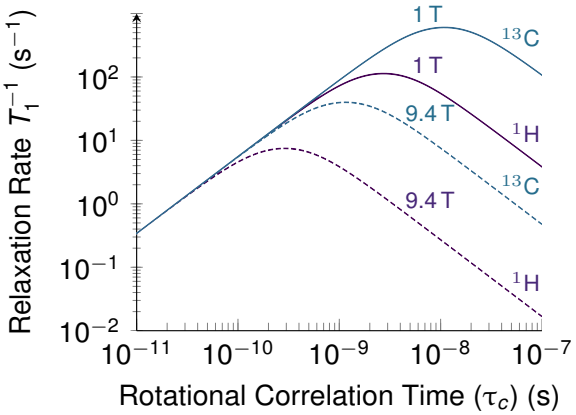


**Figure 2.8.:** Plot of $T_1^{-1}$ vs. correlation time $\tau_c$ for $^1$H (purple) and $^{13}$C represented in (cyanblue) color. The solid and dashed lines represent the 1 T and 9.4 T magnetic fields. Detailed python code is in Appendix A.3 (code A.5)

The plot shows that the relaxation rate $T_1^{-1}$ changes significantly for larger $\tau_c$ values and in low

field (1 T) it's faster than the high field (9.4 T). Additionally, nuclei with higher $\gamma$ values, such as $^{1}$H, exhibit a faster relaxation rate than those with lower $\gamma$ nuclei, such as $^{13}$C. The discussion thus far has been restricted to a simple single-spin system in a randomly fluctuating field. In more realistic cases, relaxation arises from dipole-dipole interactions among multiple spins, which will be addressed in the following section.

### 2.4.4. Dipolar Interactions

Consider a system of two isolated spins, $I$ and $S$ (e.g., $^{1}$H and $^{13}$C), in a solid crystal lattice. In the presence of a strong external magnetic field, the Zeeman interaction dominates. Using the "secular approximation", we focus on Hamiltonian terms that commute with the Zeeman Hamiltonian. The dipole-dipole Hamiltonian is then defined as:

$$\hat{H}_{DD}^{sec} = b_{IS} \left(3\cos^2\theta - 1\right) \hat{I}_z \hat{S}_z \tag{2.104}$$

where $\theta$ denotes the angle between the axis connecting the two dipolar-coupled spins and the direction of the external magnetic field ($z$-axis). The angle $\phi$ defines the orientation of the projection of the $IS$ axis onto the xy-plane, as illustrated in Fig. 2.9.

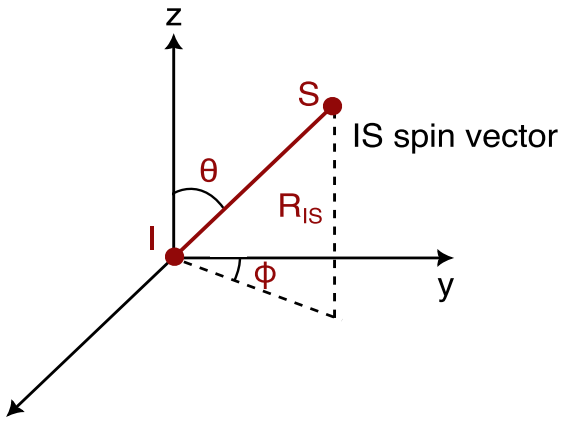


**Figure 2.9.:** In laboratory frame, the orientation of the coupled spin $IS$ vector, defined by the angles $\theta$ and $\phi$.

If the separation between the $I$ and $S$ spins is constant and defined as $r_{IS}$, then the dipolar coupling constant $b_{IS}$ can be expressed as:

$$b_{IS} = -\frac{\mu_0 \gamma_I \gamma_S \hbar}{4\pi r_{IS}^3} \tag{2.105}$$

If $\left(3\cos^2\theta - 1\right) = 0$, then the dipolar coupling vanishes. This occurs when $\theta = 54.7°$, and it is referred to as the "magic angle". In isotropic liquids, the molecular tumbling changes the orientation of the $IS$-spin axis on a time scale that is very rapid compared to dipole-dipole couplings. This averages the secular dipolar interaction to zero; nonetheless, the non-secular component can still contribute to relaxation.

In the case of a two-spin system, these dipolar interactions play a significant role in relaxation, as described in the following section.

### 2.4.5. Relaxation Dynamics in a Two-Spin System

#### 2.4.5.1. Solomon Equation

In 1955, Solomon described the dipolar spin-lattice relaxation for two mutually interacting spin-1/2[15]. In a liquid, consider two distinct isolated spins, $I$ and $S$, such as $^{1}$H and $^{13}$C. Let's assume that two spins of the same type experience only relaxation due to dipole-dipole interactions. This system exhibits four Zeeman energy levels, leading to a total of 12 transition probabilities as shown in Fig. 2.10.

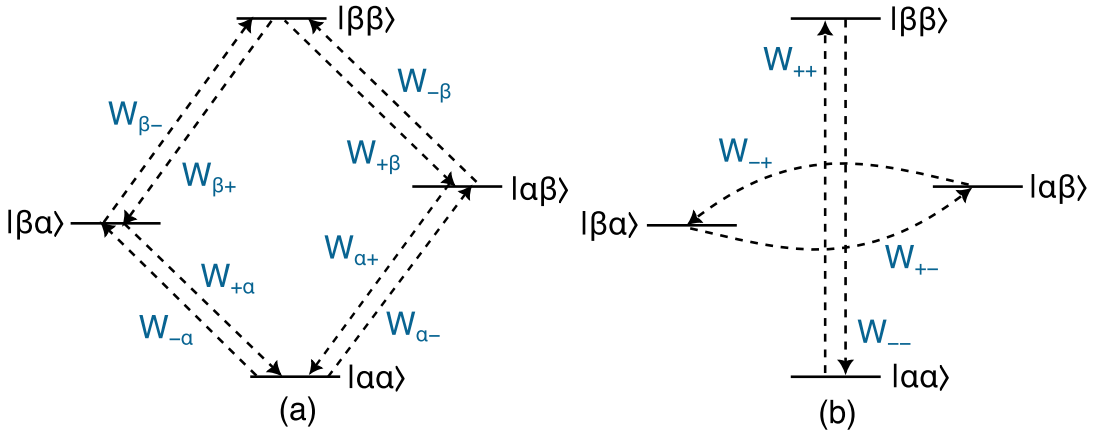


**Figure 2.10.:** Single-quantum transition probabilities total 8, as shown in (a), while there are four zero and double-quantum transitions in (b) system.

To simplify the notation, the transition probabilities that are equally likely when only S-spin changes are redefined as follows:

$$W_{\beta-} = W_{\beta+} = W_{1S}, \quad W_{\alpha-} = W_{\alpha+} = W_{1S}, \tag{2.106}$$

Similarly, when I-spin flips, the transitions can be written as:

$$W_{-\beta} = W_{+\beta} = W_{1S}, \quad W_{-\alpha} = W_{+\alpha} = W_{1I}, \tag{2.107}$$

Other zero and double-quantum transitions can be defined as:

$$W_{++} = W_{--} = W_2, \quad W_{-+} = W_{+-} = W_0, \tag{2.108}$$

The population kinetics of this four-energy-level system for the state $|\,\alpha\alpha\,\rangle$ in Fig. 2.10 can be written as:

$$\begin{aligned}\frac{dN_{\alpha\alpha}}{dt} = &-\left(W_{1I} + W_{1S} + W_2\right)\left(n_{\alpha\alpha} - n_{\alpha\alpha}^{eq}\right) + W_2\left(n_{\beta\beta} - n_{\beta\beta}^{eq}\right) \\ &+ W_{1I}\left(n_{\beta\alpha} - n_{\beta\alpha}^{eq}\right) + W_{1S}\left(n_{\alpha\beta} - n_{\alpha\beta}^{eq}\right)\end{aligned} \tag{2.109}$$

A similar equation can be formulated for the other three energy levels. The $z$-magnetization of these spins can be expressed through the following population difference:

$$\langle\,\hat{I}_z\,\rangle \propto n_I = \left(n_{\alpha\alpha} - n_{\beta\alpha}\right) + \left(n_{\alpha\beta} - n_{\beta\beta}\right) \tag{2.110}$$

$$\langle \hat{S}_z \rangle \propto n_S = \left(n_{\alpha\alpha} - n_{\alpha\beta}\right) + \left(n_{\beta\alpha} - n_{\beta\beta}\right) \tag{2.111}$$

As we know, longitudinal relaxation is proportional to the expectation value of $\hat{I}_z$ and $\hat{I}_z$ operators, which represent the population of the set of two coupled spins.

$$\frac{d\langle \hat{I}_z \rangle}{dt} = -\ (W_0 + 2W_{1I} + W_2)\left(\langle \hat{I}_z \rangle - \hat{I}_z^{\mathrm{eq}}\right) -\ (W_2 - W_0)\left(\langle \hat{S}_z \rangle - \hat{S}_z^{\mathrm{eq}}\right) \tag{2.112}$$

$$\frac{d\langle \hat{S}_z \rangle}{dt} = -\ (W_2 - W_0)\left(\langle \hat{I}_z \rangle - \hat{I}_z^{\mathrm{eq}}\right) -\ (W_0 + 2W_{IS} + W_2)\left(\langle \hat{S}_z \rangle - \hat{S}_z^{\mathrm{eq}}\right) \tag{2.113}$$

These equations can be defined in a simplified way as:

$$\frac{d}{dt}\begin{pmatrix}\langle \hat{I}_z \rangle \\ \langle \hat{S}_z \rangle\end{pmatrix} = -\begin{pmatrix}\rho_{\mathrm{I}} & \sigma_{\mathrm{IS}} \\ \sigma_{\mathrm{IS}} & \rho_{\mathrm{I}}\end{pmatrix}\begin{pmatrix}\langle \hat{I}_z \rangle - I_z^{\mathrm{eq}} \\ \langle \hat{S}_z \rangle - S_z^{\mathrm{eq}}\end{pmatrix} \tag{2.114}$$

In this context, the equilibrium longitudinal magnetization for two spins is denoted as $I_z^{\mathrm{eq}}$ and $S_z^{\mathrm{eq}}$. The spin-lattice relaxation rates are represented by $\rho_I$ and $\rho_S$, where $\sigma_{IS}$ denotes the cross-relaxation rate. Here, $\rho_I$ and $\rho_S$ are defined in terms of the spectral density functions $J(\omega)$, which reflect the frequency components of the fluctuating dipolar fields due to molecular motion. The cross-relaxation term $\sigma_{IS}$ represents mutual spin interactions, but it does not contribute when one spin remains in thermal equilibrium.

$$\rho_{\mathrm{I}} = W_0 + 2W_{1I} + W_2 \tag{2.115}$$

$$\rho_{\mathrm{S}} = W_0 + 2W_{1S} + W_2 \tag{2.116}$$

$$\sigma_{\mathrm{IS}} = W_2 - W_0 \tag{2.117}$$

The relaxation rate constants can also be expressed in terms of the spectral density function.

$$W_{1I} = \frac{3}{20} b_{IS}^2\, J(\omega_I), \qquad W_{1S} = \frac{3}{20} b_{IS}^2\, J(\omega_S), \tag{2.118}$$

$$W_2 = \frac{3}{5} b^2\, J(\omega_I + \omega_S), \qquad W_0 = \frac{1}{10} b^2\, J(\omega_I - \omega_S), \tag{2.119}$$

By substituting these values into Eqs. (2.115)–(2.117), the parameters $\rho_I$, $\rho_S$ and $\sigma_{IS}$ are obtained. The cross-relaxation rate is:

$$\sigma_{\mathrm{IS}} = \frac{b_{IS}^2}{10}\left(6\, J(\omega_I + \omega_S) - J(\omega_I - \omega_S)\right) \tag{2.120}$$

In Case I, if the S-spin (carbon) relaxes more rapidly than the I-spin (proton), the S-spin remains effectively in thermal equilibrium and no RF is applied, while the I-spin relaxes. Under these conditions, the longitudinal relaxation rate of the I-spin is given by:

$$T_{1I}^{-1} = \rho_I = \frac{b_{IS}^2}{10}\left(J(\omega_I - \omega_S) + 3\, J(\omega_I) + 6\, J(\omega_I + \omega_S)\right) \tag{2.121}$$

In Case II, considering the S-spin (carbon) in the presence of I-spin (proton) relaxation, the longitudinal relaxation rate of the S-spin is similarly expressed as:

$$T_{1S}^{-1} = \rho_S = \frac{b_{IS}^2}{10}\left(J(\omega_I - \omega_S) + 3\,J(\omega_S) + 6\,J(\omega_I + \omega_S)\right) \tag{2.122}$$

The transverse relaxation rate $T_2^{-1}$ is governed by the same dipole-dipole interactions and can be expressed as:

$$T_2^{-1} = \frac{b_{IS}^2}{20}\Big(4\,J(0) + J(\omega_H - \omega_C) + 3\,J(\omega_C) + 6\,J(\omega_H) + 6\,J(\omega_H + \omega_C)\Big) \tag{2.123}$$

Under extreme narrowing conditions, $T_1 = T_2$. The dependence of carbon-13 relaxation rates on correlation time at two fields, according to a simple isotropic rigid model, is shown in Fig. 2.11.

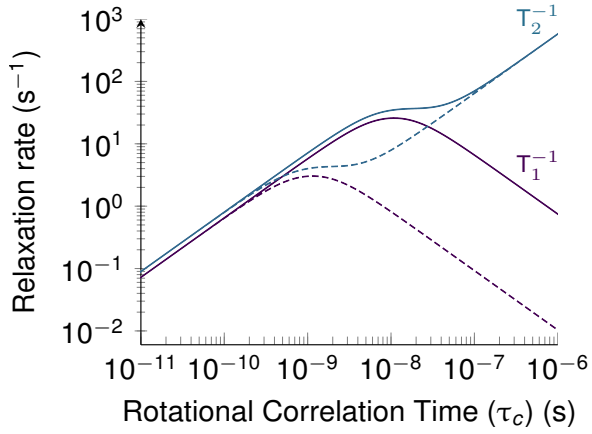


**Figure 2.11.:** Plot of $T_1^{-1}$ and $T_2^{-1}$ rates vs $\tau_c$ for a $^1$H - $^{13}$C spin pair at two magnetic fields 1 T (solid line) and 9.4 T (dashed line). Python code is provided in Appendix A.4 (code A.6).

### 2.4.6. Experimental Determination of Relaxation Times

The longitudinal relaxation time constant $T_1$ arises from energy exchange between spins and their surrounding (the lattice), which occurs most efficiently when local magnetic fields fluctuate at or near the Larmor frequency. These fluctuating fields act like small pulses on spins, causing random rotations (see section 2.4.3). Over time, this leads to the restoration of the thermal equilibrium. From the solution of bloch euqations, $T_1$ can be simply defined as:

$$M_z(t) = M_z^{\text{eq}} - \left(M_z^{\text{eq}} - M_z(0)\right) e^{-t/T_1} \tag{2.124}$$

where $M_z^{\text{eq}}$ is the thermal equilibrium magnetization along the $z$-axis and $M_z(t)$ is the longitudinal magnetization at time $t$. The transverse relaxation time constant $T_2$ describes the decay of coherences due to dephasing, which can arise from spin-spin interactions or inhomogeneous magnetic fields, including gradients. It is expressed phenomenologically as below:

$$M_{xy}(t) = M_{xy}(0)\, e^{-t/T_2} \tag{2.125}$$

Here, $M_{xy}(t)$ represents the transverse magnetization, and $M_{xy}^{\text{eq}} = 0$. To illustrate the magnetization vector in 3D space and its evolution with relaxation, a simple case is considered: a $(\pi/2)$ pulse is applied along the $x$-axis to a spin system at thermal equilibrium.

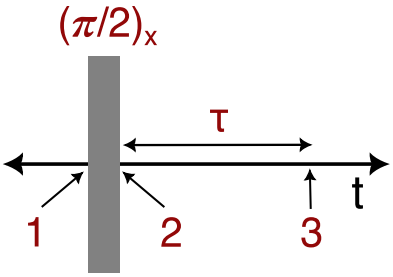


**Figure 2.12.:** Evolution of magnetization by a $(\pi/2)_x$ pulse, during a free precession interval of time $\tau$.

The evolution of the spin density operator can be written as[4]:

$$\hat{\rho}_1 = \hat{\rho}_{\text{eq}} = \frac{1}{2}\hat{1} + \frac{1}{2}B\hat{I}_z$$

$$\downarrow (\pi/2)_x$$

$$\hat{\rho}_2 = \frac{1}{2}\hat{1} - \frac{1}{2}B\hat{I}_y$$

$$\downarrow \tau$$

$$\hat{\rho}_3 = \frac{1}{2}\hat{1} + \frac{1}{2}B\left(1 - e^{-\tau/T_1}\right)\hat{I}_z + \frac{1}{2}B\left(-\hat{I}_y\cos(\Delta\omega\tau) + \hat{I}_x\sin(\Delta\omega\tau)\right)e^{-\tau/T_2}, \tag{2.126}$$

where $\Delta\omega$ represents the resonance offset and $B$ is proportional to the equilibrium magnetization. The corresponding magnetization vector components are:

$$M_x(\tau) = \sin(\Delta\omega\,\tau)\,e^{-\tau/T_2}, \tag{2.127}$$

$$M_y(\tau) = -\cos(\Delta\omega\,\tau)\,e^{-\tau/T_2}, \tag{2.128}$$

$$M_z(\tau) = 1 - e^{-\tau/T_1}. \tag{2.129}$$

The relaxation motion of the magnetization vector can be visualized as shown in Figure 2.11 (blue), after a $(\pi/2)_x$ pulse for using different values of $T_1$ and $T_2$:

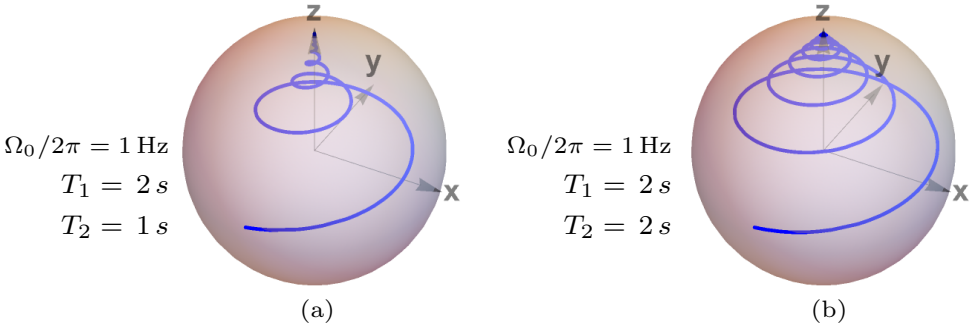


**Figure 2.13.:** Trajectory of the tip of the magnetization vector after a $(\pi/2)_x$ pulse for various values of $T_1$ and $T_2$. The images were generated using the SpinDynamica package in Mathematica, and the corresponding code is provided in the Appendix. A.5 (code A.7)

### 2.4.7. $T_1$ Measurement

Generally, there are two techniques to measure $T_1$ of a sample: inversion recovery and saturation recovery.

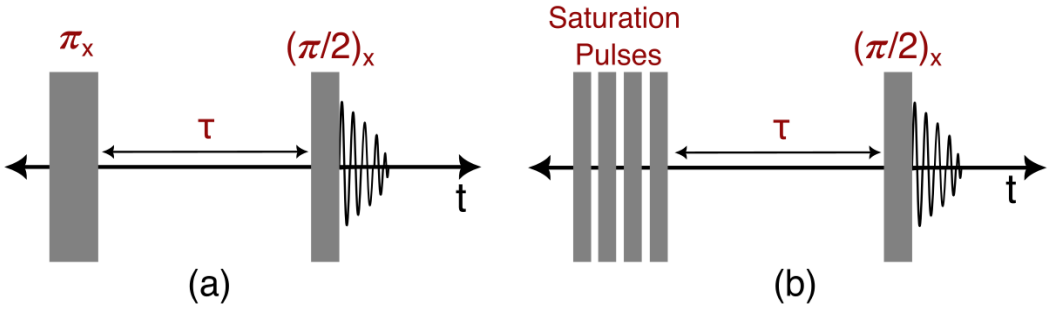


**Figure 2.14.:** (a) Schematic representation of the inversion recovery pulse sequence with a delay ($\tau$), corresponding to the magnetization recovery period. (b) Saturation recovery pulse sequence with delay ($\tau$) allowing longitudinal magnetization to recover to equilibrium.

In inversion recovery, the entire magnetization is inverted with a $\pi$ pulse, and then the signal is observed after a recovery time until the magnetization returns to equilibrium[16], as shown in Fig. 2.14 (a). The evolution of magnetization during different time periods $\tau$ in 3D space is shown in Fig. 2.15. This method is preferred for samples with short $T_1$ values, and it requires an initial guess of the values.

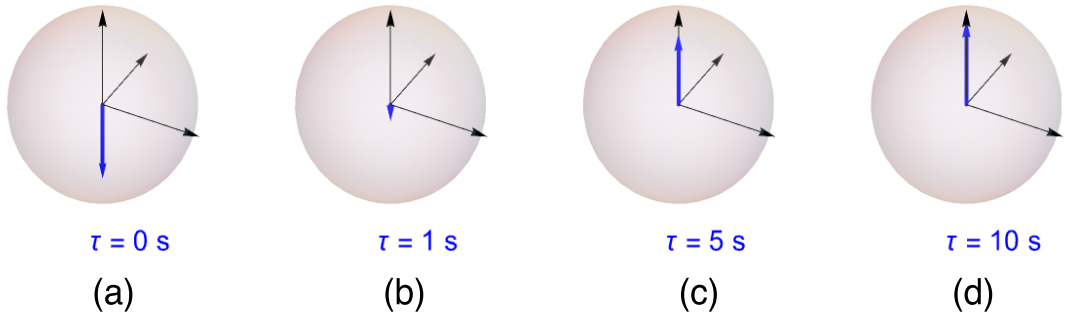


**Figure 2.15.:** Inversion recovery pulse sequence. The Bloch spheres illustrate the evolution of the magnetization vector for four different values of the delay time $\tau$ for $T_1 = 2$ s. (a) Immediately after the $\pi$ pulse ($\tau = 0$), the magnetization is inverted. (b-d) Recovery of the magnetization at $\tau = 1$ s, $\tau = 5$ s, and $\tau = 10$ s, respectively. The images were generated using the SpinDynamica package in Mathematica, and the corresponding code is provided in the Appendix. A.6 (code A.8).

For $T_1 = 2$ s, full recovery of the magnetization was observed at $\tau = 10$ s, corresponding to five times the $T_1$ value. Saturation recovery involves applying a sequence of pulse trains to saturate the signal, which means we can start from zero magnetization and use various delay times to recover the magnetization[17], as shown in Fig. 2.14 (b). Both of these methods are used for measuring $T_1$ at thermal equilibrium.

### 2.4.8. $T_2$ Measurement

Transverse relaxation ($T_2$) can in principle be measured directly from the decay of the free induction decay (FID). However, in practice, this decay often contains additional contributions from static

field inhomogeneities, leading to a shorter apparent time constant ($T_2^*$). To eliminate the effects of such inhomogeneities and chemical shift dispersion, spin-echo-based methods are used.

The Carr-Purcell-Meiboom-Gill (CPMG) sequence is the most widely employed method to measure $T_2$[18]:

$$\mathrm{CPMG}(t) = 90^\circ_x - \sum_{n=1}^{N} \left(\tau - 180^\circ_y - \tau\right), \tag{2.130}$$

In this experiment, a $90^\circ_x$ pulse first flips the magnetization into the transverse plane. A train of $180^\circ_y$ refocusing pulses then generates a series of spin echoes. Here, $N$ denotes the number of echoes, and the amplitude of successive echoes decreases due to transverse relaxation, providing a direct measure of $T_2$. By refocusing chemical shift evolution, CPMG typically provides a more accurate estimate of ($T_2$), often longer than the apparent value obtained directly from the FID decay.

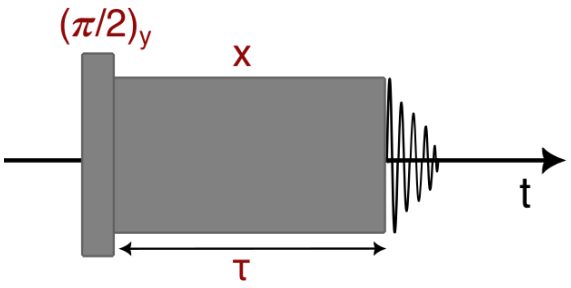


**Figure 2.16.:** Pulse sequence for a spin-locking experiment to measure $T_{1\rho}$.

For very slow molecular motions or exchange processes, CPMG-type experiments may be less effective because the refocusing condition is not fully satisfied and relaxation is dominated by different mechanisms. In such cases, spin-locking methods are often employed. Spin-locking uses a resonant RF field to suppress free precession and to lock the magnetization along a chosen axis in the rotating frame[19]. A typical spin-locking sequence is shown in Fig. 2.16.

The initial $(\pi/2)_y$ pulse converts the equilibrium $z$-magnetization to the transverse plane. The phase of the subsequent RF locking field is set to $\phi = 0$, aligning it with the transverse magnetization. If the locking field is sufficiently strong, the magnetization remains aligned with this field. After a locking period of duration $\tau$, the field is turned off, and the remaining transverse magnetization produces an NMR signal. The locked magnetization decays exponentially with a time constant $T_{1\rho}$, known as the spin-lattice relaxation time in the rotating frame.

# 3. Hyperpolarization

## 3.1. Introduction

NMR spectroscopy is inherently constrained by the low nuclear spin polarization, which follows the Boltzmann distribution within an applied magnetic field. As discussed in the previous chapter, this limits NMR sensitivity, even with optimal hardware settings. One straightforward strategy to improve sensitivity is to increase the magnetic field strength of the spectrometer. However, even the highest field NMR magnet, a 1.3 GHz instrument, provides a proton polarization of only $\sim 10^{-4}$ at thermal equilibrium despite its enormous cost. Without a radical breakthrough in magnet technology, field strength alone cannot provide the order-of-magnitude improvement required to approach unity polarization.

A more promising approach is "hyperpolarization", a family of techniques that transiently boost nuclear spin polarization far beyond thermal equilibrium. Hyperpolarization methods have found wide applications in drug discovery[20–22], medical imaging[23–25], material science[26–28], reaction monitoring[29–31], and many other fields. The common principle behind these methods is a perturbation of the Boltzmann distribution, followed by a return to equilibrium governed by the spin-lattice relaxation time constant $T_1$. Consequently, hyperpolarized states are transient, with lifetimes typically ranging from seconds to minutes.

## 3.2. Hyperpolarization Techniques

Several hyperpolarization techniques have been developed, each exploiting unique principles to boost nuclear spin polarization beyond thermal equilibrium, despite their differences in mechanism and practical implementations. The major hyperpolarization approaches are briefly discussed below.

### 3.2.1. Brute-Force Polarization

Brute-force hyperpolarization is the simplest approach, achieved by cooling a sample to cryogenic temperatures in the presence of magnetic fields. At such low temperatures, the population difference between nuclear spin states increases significantly, boosting polarization. The sample can then be rapidly warmed or transferred to lower field conditions for detection while retaining enhanced polarization for a short period. A key advantage of this method is its universal applicability, since it can be used on any sample without the need for radicals, catalysts, microwaves, or RF irradiation[32]. Although conceptually simple, it is hindered by long relaxation times ($T_1$), slow polarization buildup, and the need for specialized cryogenic equipment. To achieve 1% polarization, millikelvin temperatures are required. Studies on metabolites such as 1-$^{13}$C pyruvic acid demonstrate modest solution-state polarization of approximately 0.1%[33]. Consequently, brute-force hyperpolarization cannot be used for routine applications.

### 3.2.2. Parahydrogen-Induced Polarization (PHIP) and SABRE

Another method to generate hyperpolarization exploits the unique spin properties of molecular hydrogen ($H_2$). Due to the Pauli exclusion principle, $H_2$ exists in two nuclear spin isomers: *parahydrogen* ($I = 0$, singlet) and *orthohydrogen* ($I = 1$, triplet). The nuclear spin state is coupled to the rotational quantum number $J$, such that parahydrogen is associated with even rotational levels ($J = 0, 2, 4, \ldots$), while orthohydrogen corresponds to odd rotational levels ($J = 1, 3, 5, \ldots$)[34]. The energy difference between the lowest ortho and para states is significant ($\Delta E \sim 170$ K), which ensures that at low temperatures the equilibrium strongly favors the para form[35].

Parahydrogen can be enriched by cooling $H_2$ gas in the presence of paramagnetic catalysts such as $Fe_2O_3$ or charcoal, which speed up the typically slow ortho-para conversion[36]. The fraction of parahydrogen increases as temperature decreases, approaching nearly 100% at cryogenic conditions. Once enriched, parahydrogen remains remarkably long-lived and can be stored for long periods under ambient conditions because the spin symmetry forbids spontaneous conversion[34]. This non-equilibrium singlet spin order provides a valuable source of hyperpolarization for NMR applications.

Parahydrogen-induced polarization (PHIP) exploits this spin order by chemically adding parahydrogen to unsaturated substrates via a transition-metal-catalyzed hydrogenation[37]. During the pairwise addition, the protons become magnetically inequivalent, breaking the singlet state. This population imbalance among the spin states generates hyperpolarization, resulting in NMR signal enhancements of several orders of magnitude[32]. The hyperpolarization can further be transferred to nearby nuclei (e.g., $^{13}C$) for *in vivo* imaging[38]. PHIP has been successfully used for analyzing complex mixtures through chemosensing NMR[39]. However, the requirement for chemical modification of the substrate restricts its applicability to molecules that can undergo hydrogenation without losing their chemical properties or biological relevance.

A significant development from PHIP is "Signal Amplification by Reversible Exchange" (SABRE), which overcomes the limitation of permanent chemical modification [40]. In SABRE, both the substrate and p-$H_2$ bind transiently to a transition metal complex (often iridium catalysts)[41, 42]. Through scalar couplings within the complex, polarization is transferred from the parahydrogen-derived hydrides to the substrate nuclei ($^1H$, $^{13}C$, or $^{15}N$)[43]. Because the exchange is reversible, the substrate is released in its original chemical form but with enhanced polarization. This mechanism allows repeated polarization transfer, enabling continuous hyperpolarization under mild conditions.

SABRE provides several advantages: (i) it does not require permanent chemical modification of the substrate, (ii) hyperpolarization can be continuously regenerated as long as parahydrogen is supplied, and (iii) it is particularly effective for substrates containing coordinating groups such as nitrogen heterocycles[44]. These variants broaden the range of applicable target drug molecules and open opportunities in metabolic imaging and in vivo studies. SABRE has been shown to successfully hyperpolarize a variety of drugs, such as pyrazinamide, isoniazid[45], and dalfampridine[46, 47].

Despite their advantages-fast polarization buildup, low cost, room-temperature operation, and the potential for continuous polarization, PHIP and SABRE still face practical limitations. PHIP requires chemical transformation of the substrate, which restricts its generality, while SABRE relies on transition metal catalysts that may limit biocompatibility and raise concerns about purification. Nevertheless, these parahydrogen-based methods are highly complementary to other hyperpolarization approaches and an active area of methodological development.

### 3.2.3. Photochemically Induced Dynamic Nuclear Polarization (Photo-CIDNP)

Photo-CIDNP is another hyperpolarization technique in which light-driven chemical reactions generate non-equilibrium nuclear spin populations, resulting in enhanced NMR signals for specific nuclei[48, 49]. During this process, a photoactive chromophore absorbs light and is excited to a singlet or triplet state. Once excited, the species can then interact with a nearby electron donor or acceptor, forming a short-lived radical pair through electron transfer reactions. Hyperfine interactions within the radical pair induce spin sorting, selectively enhancing the nuclear polarization of nuclei nearby the radicals[50, 51]. Upon recombination or separation of the radicals, these nuclei exhibit non-Boltzmann spin populations, which are detected as NMR signals. Photo-CIDNP provides site-selective hyperpolarization and operates under ambient conditions, making it especially useful for studying protein structures, reaction intermediates in photochemical and biochemical systems[32, 51].

### 3.2.4. Dynamic Nuclear Polarization (DNP)

The following discussion is based on the ref.[32, 52]. DNP is a method for polarizing nuclei via electron thermal spin polarization. By irradiating electron spin transitions with microwaves, polarization is transferred to nearby nuclei through hyperfine interactions. As outlined in section 2.1.3, electrons have a gyromagnetic ratio that is 660 times higher than protons, resulting in a stronger Zeeman interaction. Consequently, in DNP, the resonance frequencies are around 100 GHz, necessitating the use of microwave transmitters to excite electron transitions and microwave receivers for direct detection of these transitions. Electrons can attain complete polarization by cooling to temperatures between 1-2 K in a magnetic field of 6.7 T or higher, as shown in Fig. 2.2. To achieve significant nuclear polarization, the nuclear spin temperature must be below 10 mK. Solid-state DNP, often combined with magic-angle spinning (MAS), is widely used for studying protein structure, biomolecular assemblies, and materials[53–55].

In experimental setups, the sample is placed in a liquid helium cryogenic magnet under high-field conditions, which may or may not be homogenous, accompanied by a nearby microwave source. To provide electrons, free radicals have been used. These molecules with unpaired electrons that are evenly distributed throughout the sample. The most frequently used radicals in this process are (2,2,6,6-Tetramethylpiperidin-1-yl)oxyl, commonly known as TEMPO, and Trityl Ox063. The choice of radical and its concentration depends on the type of nuclei to be hyperpolarized. For optimal polarization transfer, glassy matrix solvents such as DMSO or glycerol, which form a homogeneous glass upon freezing, are commonly used, as illustrated in Fig. 3.1.

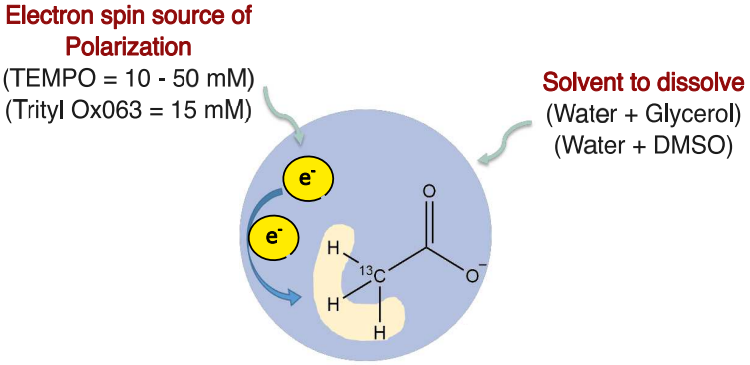


**Figure 3.1.:** Illustration of a DNP sample composition.

By saturating electron transitions at a specific microwave frequency, polarization can be transferred to surrounding spins. Since the electron's $T_1$ is much shorter than that of nuclei, the electron polarization can be quickly restored and transferred to neighboring nuclei, shown in Fig. 3.1. The depolarized electron can then be polarized quickly again due to its short $T_1$. This cycle continues until the non-equilibrium polarization disperses through the samples, at which point it becomes sufficiently polarized. The transfer occurs due to hyperfine interactions between nuclear and electron spins.

The transfer of polarization from electrons to nuclei is fundamentally governed by the interaction of the electron magnetic moment with the external magnetic field. To describe this interaction quantitatively, it is necessary to introduce the **g**-tensor formalism, which captures the anisotropic nature of the electron Zeeman effect. The magnetic moment of the electron spin is defined similarly to the NMR magnetic moment discussed earlier, with an additional factor **g**[56]:

$$\mu = -\mu_B \, \mathbf{g} \, \hat{\mathbf{S}} \tag{3.1}$$

In this context, **g** represents a tensor quantity expressed as a 3 x 3 matrix. This factor determines the spectral width and shape. The angle between **g** and the applied magnetic field defines the interaction energy of the magnetic moment with the magnetic field. Therefore, the Zeeman interaction Hamiltonian can be written as:

$$\hat{H} = -\mathbf{B}\,\mu = \mu_B \, \mathbf{B} \, \mathbf{g} \, \hat{\mathbf{S}} \tag{3.2}$$

Since **g** is a matrix here, the magnetic moment and spin **S** are not necessarily aligned. For a free electron, the **g**-tensor is isotropic and written:

$$\mathbf{g} = g_s \begin{pmatrix} 1 & 0 & 0 \\ 0 & 1 & 0 \\ 0 & 0 & 1 \end{pmatrix} \tag{3.3}$$

For the free electron, $g_s = 2.0023$[57]. The magnetic field direction with respect to the **g**-tensor is defined using spherical angles $\phi$ and $\theta$. The Hamiltonian in the principal axis frame is defined as below:

$$\begin{aligned} \hat{H} &= \mu_B \, B_0 \, (\sin\theta\cos\phi,\ \sin\theta\sin\phi,\ \cos\theta) \begin{pmatrix} g_x & 0 & 0 \\ 0 & g_y & 0 \\ 0 & 0 & g_z \end{pmatrix} \begin{pmatrix} \hat{S}_x \\ \hat{S}_y \\ \hat{S}_z \end{pmatrix} \\ &= \mu_B \, B_0 \left( \sin\theta\cos\phi \, g_x \, \hat{S}_x + \sin\theta\sin\phi \, g_y \, \hat{S}_y + \cos\theta \, g_z \, \hat{S}_z \right) \end{aligned} \tag{3.4}$$

In Eq. (3.4), $\sin\theta\cos\phi = \ell$, $\sin\theta\sin\phi = m$, and $\cos\theta = n$ denote the direction cosines, following the notation of Abragam and Bleaney[58]. To simplify the expressions, $\ell' = g_x\ell$, $m' = g_y m$, and $n' = g_z n$ are defined as the direction cosines in the principal axes of the **g**-tensor. Using these definitions, the Hamiltonian can be rewritten as

$$\hat{H} = g \, \mu_B \, B_0 \left( \ell' \, \hat{S}_x + m' \, \hat{S}_y + n' \, \hat{S}_z \right) \tag{3.5}$$

Recall from Eq. (2.43) Pauli's spin operators, which are analogous to $S_x$, $S_y$, and $S_z$. Consequently, the electron spin Hamiltonian in the Zeeman basis can be represented as follows:

$$\hat{H} = \frac{\mu_B B_0}{2} \begin{bmatrix} n g_z & l g_x - i m g_y \\ l g_x - i m g_y & -n g_z \end{bmatrix} \tag{3.6}$$

The energy eigenvalues $E$ of the Hamiltonian $\hat{H}$ can be determined as:

$$\det(\hat{H} - E\,I) = 0 \tag{3.7}$$

$$\det\left(\frac{\mu_B B_0}{2}\begin{bmatrix} ng_z & lg_x - img_y \\ lg_x - img_y & -ng_z \end{bmatrix} - E\begin{bmatrix} 1 & 0 \\ 0 & 1 \end{bmatrix}\right) = 0 \tag{3.8}$$

$$\det\left(\frac{\mu_B B_0}{2}\begin{bmatrix} ng_z - E & lg_x - img_y \\ lg_x - img_y & -ng_z - E \end{bmatrix}\right) = 0 \tag{3.9}$$

$$\frac{\mu_B B_0}{2}\left((ng_z - E)\,(ng_z - E) - \left(lg_x - img_y\right)\left(lg_x - img_y\right)\right) = 0 \tag{3.10}$$

This can be simplified to:

$$E^2 = \left(\frac{\mu_B B_0}{2}\right)^2 \left(l^2 g_x^2 + m^2 g_y^2 + n^2 g_z^2\right) \tag{3.11}$$

$$E = \frac{\mu_B B_0}{2}\sqrt{l^2 g_x^2 + m^2 g_y^2 + n^2 g_z^2} \tag{3.12}$$

These are the energy levels associated with this Hamiltonian, which can also be expressed in the following way in spherical coordinates:

$$E_i = \pm\frac{1}{2}\, g_{\text{eff}}(\phi, \theta)\, \mu_B B_0, \tag{3.13}$$

where $g_{\text{eff}}$ represents the effective **g** factor of a free spin with direction cosines determined by the orientation of the electron in the magnetic field. This factor is the essential connection between a molecule's quantum mechanical properties and its observable EPR spectrum. It determines the resonance frequency at which an unpaired electron absorbs microwave radiation within a magnetic field.

$$g_{\text{eff}} = \sqrt{(g_x \ell)^2 + (g_y m)^2 + (g_z n)^2} \tag{3.14}$$

In practice, TEMPO, a broadband radical, is used for polarizing $^1$H, and Trityl (Ox063), a narrow-band radical, is used for $^{13}$C. Radicals can also be produced by exposing carbon containing a ketonic group to UV light, which can then be used for DNP[59]. Representative $g_{\text{eff}}$ values are given in the Table 3.1[60, 61].

| **Radical** | $g_{\mathbf{x}}$ | $g_{\mathbf{y}}$ | $g_{\mathbf{z}}$ |
|---|---|---|---|
| Tempo | 2.0094 | 2.0065 | 2.0017 |
| Trityl (OX063) | 2.0031 | 2.0031 | 2.0025 |
| Keto-UV | 2.0036 | 2.0027 | 2.0007 |

**Table 3.1.:** g-values for selected radicals.

By using all the parameters for simulation for $10^5$ orientations, such as the rotation matrix followed by $g_{\text{eff}}$, and converting the simulated data to frequencies, the powder EPR spectra of TEMPO and Trityl at high field are shown in Figure 3.2. This illustrates the distinct line shape due to g-tensor anisotropy. For EPR spectra, the details of the full Hamiltonian derivation and rotation matrices are provided in Appendix A.7. To understand DNP, it is necessary to consider the nuclear spin interaction and how it couples to the electron spin.

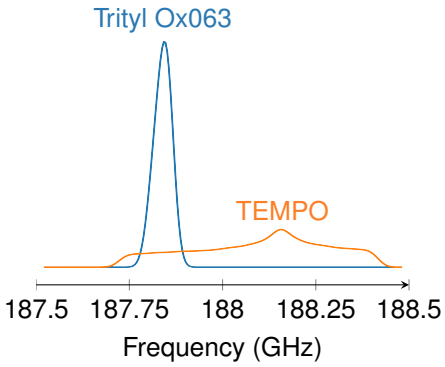


**Figure 3.2.:** EPR powder spectrum of Trityl Ox063 and TEMPO at the constant field of 6.7 T

In any given sample, the presence of both electron and nuclear spins is observed in close proximity. The electron, which is a spin-1/2, interacts not only with the magnetic field but also with the nuclear spin $I$ (spin-1/2). This interaction can be expressed as hyperfine coupling in the Hamiltonian.

$$H = \frac{\mu_B\, g\, B}{\hbar}\hat{S}_z + \mathbf{A}\,\hat{S}_z\,\hat{I}_z - \gamma_I\, B\,\hat{I}_z \tag{3.15}$$

The largest interaction in this Hamiltonian is the electron Zeeman interaction. Here, $\mathbf{A}$ is the hyperfine coupling tensor, a (3×3) matrix. The corresponding energy levels of this Hamiltonian are given by:

$$E = \frac{\mu_B\, g\, B}{\hbar} m_s + \mathbf{A}\, m_s\, m_I - \gamma_I\, B\, m_I \tag{3.16}$$

with basis states

$$|1\rangle = (\uparrow_e, \uparrow_n), \quad |2\rangle = (\downarrow_e, \uparrow_n), \quad |3\rangle = (\uparrow_e, \downarrow_n), \quad |4\rangle = (\downarrow_e, \downarrow_n) \tag{3.17}$$

The transitions between energy states through various mechanisms result in nuclear polarization and are discussed in the subsequent section.

## 3.3. DNP Mechanisms

For solid-state DNP, there are four mechanisms that explain these interactions: the Overhauser effect, the solid effect, the cross-effect, and thermal mixing.

### 3.3.1. Overhauser Effect (OE)

In 1953, Overhauser introduced the idea of enhancing the NMR signal in the presence of free electrons using microwave irradiation [62]. Both this effect and the solid-state effect involve interactions between a nuclear spin and an electron spin. The Hamiltonian is shown in Eq. (3.15). The Overhauser effect relies on saturating an allowed electron paramagnetic resonance (EPR) transition and cross-relaxation pathways that transfer polarization from electrons to nuclei.

Microwave irradiation equalizes the populations of two spin states $|1\rangle$ & $|2\rangle$, and then, through electron-nuclear flip-flops $W_{14}$ and $W_{41}$ mediated through hyperfine coupling Fig 3.3 (a), nuclear polarization is enhanced. The effect is most efficient in liquids or conductors and at relatively low

fields, where molecular motion effectively modulates the hyperfine interaction and electron relaxation is sufficiently rapid. In the high-temperature limit, the enhancement factor is:

$$\varepsilon_{\mathrm{OE}} = \frac{\gamma_e}{\gamma_n}, \tag{3.18}$$

which is $\approx 660$ for protons and even larger for low-$\gamma$ nuclei. The OE is most effective in liquids or metals with fast electron relaxation.

### 3.3.2. Solid Effect (SE)

The solid effect occurs in insulating solids where electron-nuclear cross relaxation, as required for the Overhauser effect, is inefficient or absent. Here, microwave irradiation directly drives the forbidden electron-nuclear transitions, made allowed by hyperfine-induced state mixing. Irradiating at microwave frequencies offset from the EPR resonance by the nuclear Larmor frequency ($\omega_e \pm \omega_n$) induces the nominally forbidden transitions with $\Delta m_S = \pm 1$ and $\Delta m_I = \pm 1$, resulting in either positive or negative nuclear polarization, as illustrated in Fig. 3.3(b).

$$\begin{cases} \omega_e - \omega_n : & \Delta m_S = -1,\ \Delta m_I = +1 \quad \text{(flip–flop)} \ \rightarrow \text{positive DNP}, \\ \omega_e + \omega_n : & \Delta m_S = +1,\ \Delta m_I = +1 \quad \text{(flip–flip)} \ \rightarrow \text{negative DNP}. \end{cases}$$

The efficiency of the solid effect depends strongly on the degree of hyperfine mixing and the linewidth of the EPR spectrum. It is most pronounced at low to moderate magnetic fields and in systems with narrow EPR lines, such as trityl radicals, where the microwave frequency can selectively address the $\omega_e \pm \omega_n$ transitions.

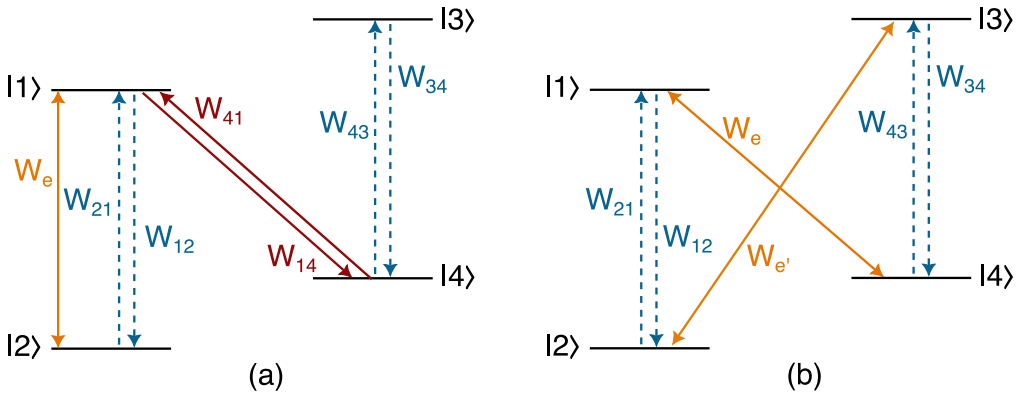


**Figure 3.3.:** Energy levels of an electron spin and a nuclear spin which are coupled by a hyperfine coupling shown by states $|1\rangle$ & $|2\rangle$, $|3\rangle$ & $|4\rangle$. In EPR, one observes electron spin flips (blue dashed transitions). Note that the hyperfine interaction splits the electron spin resonance and shifts the nuclear spin transitions. The electron Zeeman interaction is orders of magnitude larger than the other interactions - the drawing is not to scale. (a) In the Overhauser effect, the $W_{14}$ and $W_{41}$ (shown in red) are the electron-nuclear flip-flops due to the Fermi contact interaction. (b) shows the solid-effect due to microwave irradiation, depending on microwave frequency, the positive $W_e$ or negative DNP $W_{e'}$ are shown in orange.

Another class of DNP mechanisms involves three-spin processes comprising two electrons and one nucleus. These are known as the cross-effect and thermal mixing. They become particularly important in multi-electron systems with strong couplings, and are especially relevant in high-field DNP. A detailed discussion of these mechanisms will be provided in the following section.

### 3.3.3. Cross-Effect (CE) and Thermal Mixing (TM)

In systems containing two or more coupled unpaired electrons, additional DNP mechanisms become active. Consider two electron spins ($S_1$ and $S_2$) that have slightly different resonance frequencies due to differences in $g$-tensors, local fields, and other factors, along with one nuclear spin ($I$). The electrons are coupled via dipolar interactions, and the nuclear spin interacts with one or both electrons via hyperfine couplings. An effective Hamiltonian can be expressed as:

$$H = \omega_{S1} S_{1z} + \omega_{S2} S_{2z} - \omega_I I_z + \mathbf{S}_1 \mathbf{A}_1 \mathbf{I} + \mathbf{S}_2 \mathbf{A}_2 \mathbf{I} + \mathbf{S}_1 \mathbf{D} \mathbf{S}_2 \tag{3.19}$$

Here, $\mathbf{D}$ denotes the dipolar coupling between the electrons, and $\mathbf{A}_1$, $\mathbf{A}_2$ are the hyperfine couplings to the nucleus. The vectors $\mathbf{S}_1$ and $\mathbf{S}_2$ represent the spin operators of the electrons. The cross effect (CE) occurs when the difference between the resonance frequencies of these electrons matches the nuclear Larmor frequency, i.e., $|\omega_{S1} - \omega_{S2}| = \omega_I$. Under microwave irradiation, a simultaneous flip-flop of the two electrons accompanied by a nuclear spin flip enables polarization transfer from the electrons to the nucleus. This three-spin process effectively couples the electron and nuclear spin reservoirs, making CE particularly efficient at high magnetic fields[52, 63]. Although this mechanism can function with many radicals, it is most effective when using biradicals like AMUPol or TEMTriPol. These molecules are optimized for electron-electron couplings and linewidths, ensuring that the CE matching condition is met and polarization transfer is maximized[64].

Thermal mixing (TM) is a polarization transfer mechanism that requires a network of strongly dipolar-coupled electron spins, often referred to as a "spin reservoir." This reservoir can be characterized by a well-defined spin temperature. TM is most efficient at low temperatures and high radical concentrations, where the electrons achieve a high degree of polarization. Microwave irradiation saturates a part of the electron spectrum, pushing the reservoir out of equilibrium and creating a non-equilibrium spin temperature. Nuclear spins, dipolarly coupled to the electron reservoir, then partially equilibrate with it, leading to the transfer of polarization from electrons to nuclei. Unlike the cross effect (CE), which relies on a precise matching of electron frequency differences to the nuclear Larmor frequency and is most efficient with biradicals, TM is a collective, many-spin process that benefits from broad EPR linewidths. In modern high-field DNP, both CE and TM are the dominant mechanisms under cryogenic conditions and typical radical concentrations.[52, 63]

One major drawback of conventional DNP is that the enhanced polarization remains confined to the solid matrix at cryogenic temperatures. A breakthrough came with the introduction of dissolution-DNP by Ardenkjær-Larsen and co-workers, which enables transfer of this polarization into the liquid state for high-sensitivity liquid-state NMR and MRI experiments[1].

### 3.3.4. Dissolution-DNP (D-DNP)

In the D-DNP process, a hyperpolarized solid sample is rapidly dissolved with a hot solvent and then transferred from the cryogenic magnet to the NMR spectrometer. The resulting solution is then transferred to a high-field magnet for liquid-state detection. This approach enables signal enhancements exceeding four orders of magnitude, with SNR improvements greater than 10,000 in liquid-state NMR[1]. These hyperpolarized solutions can also be injected into living systems for metabolic imaging[65], used *in vivo* preclinical studies to probe cellular metabolism[66], and applied to ligand-binding studies for screening[67].

### 3.3.5. Limitations of D-DNP

While D-DNP has transformed the field of hyperpolarized NMR, it remains fundamentally constrained by several limitations:

- The need for several milliliters of hot solvent for dissolution, resulting in large dilution factors (typically ~100-fold).
- Hot solvent can denature sensitive samples, such as proteins, leading to loss of biological activity.
- Limited applicability to mass-limited biological samples, the large solvent volumes cause significant dilution, which substantially reduces sensitivity and limits achievable signal enhancement.
- Significant polarization loss during transfer due to finite $T_1$ relaxation times.

Despite its transformative impact, D-DNP remains limited by large dissolution volumes, substantial dilution, and polarization loss during transfer. These constraints have motivated the search for alternative hyperpolarization approaches capable of achieving comparable sensitivity with smaller sample volumes and simplified instrumentation.

Several techniques have been developed in this context, including chemically induced dynamic nuclear polarization (CIDNP)[68, 69], parahydrogen-induced polarization (PHIP)[70], and signal amplification by reversible exchange (SABRE)[42]. These methods have extended the detection limits of NMR down to sub-micromolar or even picomolar concentrations[71, 72]. However, they are generally constrained to specific chemical systems requiring parahydrogen incorporation or catalyst compatibility. In contrast, DNP remains broadly applicable because it functions via electron-nuclear spin diffusion instead of relying on specific molecular requirements.

One such strategy is the recently developed "bullet-DNP" technique, which reverses the conventional D-DNP workflow by transporting the hyperpolarized solid directly to the NMR magnet before dissolution. Dissolving the sample immediately prior to detection minimizes polarization loss and dilution, while offering excellent repeatability and automation potential. This innovation directly addresses the bottlenecks of conventional D-DNP and opens new possibilities for studying biomolecules at nanomolar to micromolar concentrations.

The following sections describe the principles and implementation of bullet-DNP, forming the basis for the experimental work presented in subsequent chapters.

## 3.4. Bullet-DNP Instrumentation

In the conventional D-DNP approach, the hyperpolarized sample is dissolved with hot solvent before being transferred to the secondary magnet for liquid-state detection. Typically, this requires dilutions on the order of 100-fold, using several milliliters of solvent. The transfer time is a few seconds, which again leads to loss of polarization due to $T_1$ relaxation. These limitations restrict the applicability of conventional D-DNP for studying biological samples[73–75] where the sample quantity is limited and high sensitivity is necessary. Additionally, they also have very short $T_1$ relaxation times.

The "bullet-DNP" approach, developed by Kouřil and co-workers[2, 3], addresses these challenges by inverting the sequence of dissolution and transfer. The overall polarizer design follows conventional dissolution-DNP systems, but with key modifications: (i) the ability to eject samples rapidly in frozen

form using pressurized helium gas, (ii) a magnetic transfer tunnel that preserves polarization during transport to the detection magnet, and (iii) an automated injector that enables dissolution with a minimal amount of solvent needed for NMR. For hyperpolarization, the sample is placed in a miniature cylindrical container made with PTFE (Teflon) material called a “bullet” with an opening at the top and an internal volume of approximately 50 µL. This approach requires a specialized cryogenic polarizer, described in a later section.

The operation of the bullet-DNP setup proceeds in a sequence of well-defined steps. First, the sample is polarized in the solid state under microwave irradiation at cryogenic temperatures inside the DNP insert until the desired polarization is achieved. After the DNP step, instead of dissolving the hyperpolarized solid inside the polarizer, the solid sample is ejected in frozen form using a short burst of pressurized helium gas and rapidly transported through a magnetically shielded tunnel to the NMR detection magnet. Dissolution then occurs inside a liquid-state NMR magnet, immediately prior to acquisition. This scheme is known as "bullet-DNP". Using this method has a major benefit: it requires only approximately 700 µL or less of solvent, without needing to heat it, since the solvent was never exposed to a cryogenic environment. This makes it a better fit for biological samples. The low dilution results in high magnetization in the liquid state.

### 3.4.1. Bullet-DNP Polarizer

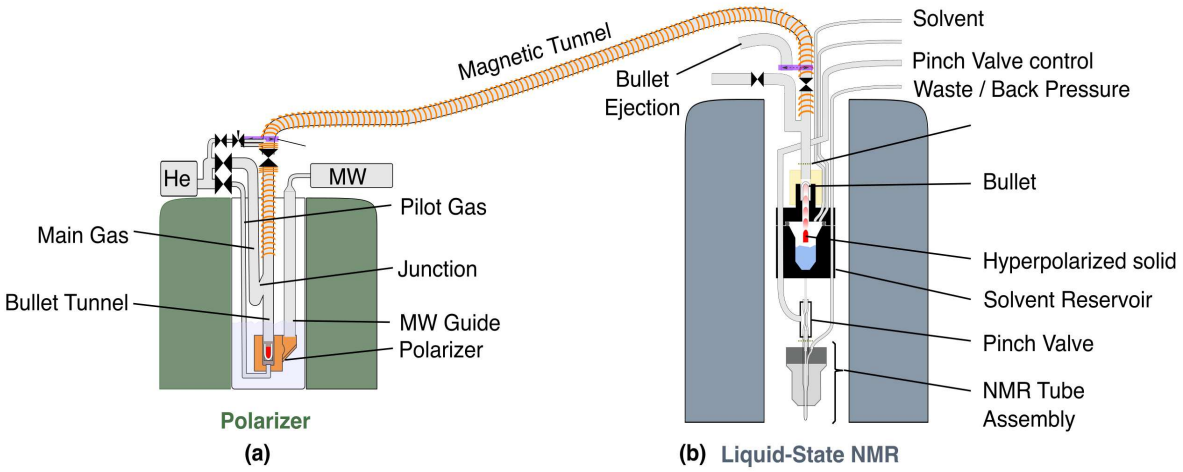


**Figure 3.4.:** Schematic representation of the bullet-DNP setup, adapted from [2, 3]. (a) Overview of the apparatus, including the polarizer magnet with cryostat and DNP insert, the transfer tube equipped with a solenoid along its length, and (b) the injection device inside the liquid-state NMR magnet. During operation, the hyperpolarized solid sample (red) passes through the magnetic tunnel and dissolves upon impact with the solvent (blue) in the reservoir. The reservoir is then pressurized, and the pinch valve is opened to allow the liquid into the NMR flow tube via its inner capillary. After a short delay, back pressure is applied to stabilize the sample, and NMR acquisition is triggered. Following the measurement, the empty bullet is removed by pressurizing the solvent reservoir.

The bullet-DNP polarizer used in this work is based on the design of Kouřil and co-workers [2], with subsequent improvements to the magnet system, cryogenic handling, and injection device [3]. The polarizer employs a superconducting magnet system (Cryogenic Ltd., UK) cooled by a closed helium cycle. The sample space can be cooled to a base temperature of 1.4 K by condensing gaseous helium. The magnet has a bore diameter of 50 mm and operates at 6.7 T, corresponding to a microwave frequency of 188 GHz. Microwave irradiation is supplied by a source with an effective output power of up to ~150 mW.

The DNP insert consists of channels for sample loading, helium drive gas, and microwave delivery, shown in Fig 3.4 (a). A gold-plated mirror and RF saddle coil (mounted on a PEEK support) enable microwave irradiation and in situ monitoring of polarization. The samples are contained in PTFE bullets. A burst of helium gas propels the frozen sample through a 3.2 m long transfer tunnel. The transfer path is surrounded by a solenoid energized with 50-60 A, producing a guiding field of 60-75 mT, ensuring that nuclear spin polarization is effectively preserved during transfer. To match the polarities of the polarizer and the secondary magnet, Helmholtz coils at the exit of the DNP insert adiabatically invert the field direction, maintaining spin quantization throughout the transfer[2, 3].

### 3.4.2. Injection Device

The injection device represents one of the most significant improvements in the updated bullet-DNP system[3]. It consists of three main elements: a solvent reservoir, a gas-actuated pinch valve, and a flow NMR tube, Fig 3.4 (b). The bullet arrives through the transfer tunnel and is stopped in a constriction in the reservoir lid. The hyperpolarized solid pellet continues into the reservoir, where it dissolves upon contact with 700 µL of solvent. The solvent reservoir, made of titanium, is rapidly pressurized to 3 bar with helium.

The solution is then directed into a 3 mm flow NMR tube via the pinch valve, which consists of a short section of silicone tubing compressed under 8 bar air pressure to control flow. This flow tube offers improved handling of aqueous samples and enables sample removal by applying back-pressure through the inner capillary. Upon arrival of the sample in the magnet, the NMR signal is detected within approximately ~1 s of dissolution, synchronized with the spectrometer triggers. After the experiment, the injection device is automatically cleaned and dried using pulses of helium pressure, preparing the system for the next run.

## 3.5. Scope of the Thesis

The bullet-DNP method offers several advantages over conventional dissolution-DNP (D-DNP). It achieves high spectral resolution, with $^{13}C$ and $^{1}H$ linewidths as narrow as 2 Hz[3] and 4 Hz[76], and enables rapid, semi-automated operation. A major advantage is the ability to work with extremely small sample volumes. While standard D-DNP typically requires tens to hundreds of milligrams of sample frozen with radicals, and subsequent dissolution in milliliters of hot solvent, this results in large dilution factors of ~100-fold[77, 78]. In contrast, bullet-DNP can operate with sample volumes as low as 2 µL. Although the numerical dilution factor can be as high as ~250, the absolute amount of material consumed remains orders of magnitude lower, on the order of a few nanograms. Careful optimization of sample formulation and the choice of efficient spin-diffusion agents enables high polarization levels even in such small sample masses. This makes bullet-DNP uniquely suited for experiments with nanomolar substrate concentrations, where conventional D-DNP would be impractical.

Furthermore, bullet-DNP eliminates the need for hot solvents, allowing sensitive biological samples such as proteins to be studied without compromising their structure or activity. This capability has been leveraged to extend bullet-DNP to ligand-protein binding studies, particularly under low-field conditions where $T_1$ relaxation of large biomolecules provides favorable sensitivity. The following chapters present the experimental implementation and results obtained with bullet-DNP.

# 4. Boosting Mass and Concentration Sensitivity with Bullet-DNP

The content of this chapter is based in part on the publication in Ref. [76].

## 4.1. Introduction

NMR spectroscopy provides valuable insights into molecular structure, dynamics, and interactions, but its sensitivity is inherently limited by weak thermal spin polarization. As a result, the concentration sensitivity typically lies in the range of 10-100 μM[79]. Several hyperpolarization methods have reported sensitivity gains down to the picomolar range, though each approach faces certain limitations[32]. For instance, nanomolar concentrations of tryptophan have been detected using chemical-induced dynamic nuclear polarization, a technique that has recently shown efficacy for several hundred molecules[68, 69]. Additionally, if the target molecule can be synthesized from a precursor through hydrogenation with parahydrogen[70], or if it can bind to a suitable catalyst[42], parahydrogen-induced polarization can enhance concentration sensitivity to the sub-micromolar range[71] and mass-sensitivity to the picomolar range.[72] Attempts to apply DNP to mass-limited samples using an immiscible heat-carrying co-solvent[80], or performing in situ detection with a rapid-melt procedure within the polarizing device[81, 82], have failed to produce high-resolution liquid-state spectra.

To overcome this limitation, the bullet-DNP method has been used in this study. It reverses the sequence of the conventional D-DNP step. It transfers the hyperpolarized material from the cryogenic system in the solid state and dissolves directly inside the NMR magnet. Chapter 2 described the principle, instrumentation, and potential of bullet-DNP. This chapter demonstrates the capability of bullet-DNP to achieve high mass sensitivity with broad applicability. It further advances the method toward practical use by demonstrating improved reproducibility, spectral resolution, and sensitivity, enabling detection down to the nanomolar range.

In addition to improving sensitivity, it is equally important to evaluate how these methods perform under conditions representative of clinical applications. In metabolic imaging, signal detection does not occur immediately after dissolution but rather after a delay corresponding to the time required for metabolic conversion.

The objectives of this study were:

1. To optimize bullet-DNP experiments for improved repeatability, spectral resolution, and sensitivity.
2. To achieve high mass sensitivity by combining refined sample preparation with reverse INEPT ($^{13}C \rightarrow {}^{1}H$) detection.
3. To demonstrate the detection of pyruvate at nanomolar concentrations as a benchmark case.

4. To extend the methodology to mixtures of amino acids, illustrating its applicability to more complex biological systems.
5. To evaluate the feasibility of the method under conditions mimicking clinical requirements, such as delayed detection after dissolution.

The following sections describe the experimental setup, DNP optimization, sample preparation, and detection strategies employed to achieve these goals.

## 4.2. Experimental Setup

The bullet-DNP setup consists of three key components:

1. **Polarizer:** Operates at a magnetic field of 6.7 T and a temperature of approximately 1.5 K, where frozen samples are hyperpolarized in the presence of radicals.
2. **Magnetic Tunnel:** Transfers the hyperpolarized sample from the polarizer to the secondary NMR detection magnet.
3. **Injection Device:** Located within the secondary magnet at 9.4 T, where the solid hyperpolarized bullet is dissolved in a pressurized solvent reservoir and injected directly into the NMR tube for signal acquisition.

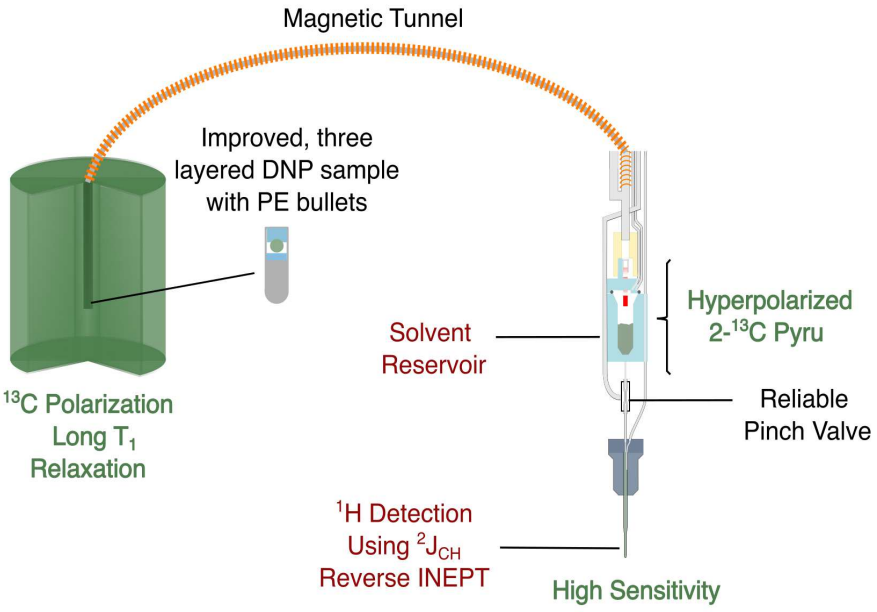


**Figure 4.1.:** Schematic overview of the bullet-DNP setup with instrumental improvements (bullet material, optimized bullet composition, and pinch valve).

The experimental setup shown in Fig 4.1 was used throughout this study. Over time, several instrumental improvements were implemented, including optimization of the bullet sample composition and a reliable pinch valve. These modifications were part of the ongoing methodological developments in the laboratory and significantly improved the reliability of the experiments described in this chapter. This improved the reproducibility, resolution, and sensitivity of the Bullet-DNP system. After these improvements, first step involves the selection of the DNP sample, discussed in the following section.

### 4.2.1. Choice of Detection Nucleus and $T_1$ Considerations

To improve sensitivity, one key factor is the choice of detection nucleus. Efficient liquid-state detection in DNP depends critically on both the polarization achievable in the solid state and the ability to preserve this polarization during transfer and dissolution. Although $^{1}$H offers a higher intrinsic SNR due to its larger gyromagnetic ratio, its much shorter $T_1$ compared to $^{13}$C often results in substantial polarization loss during transfer and dissolution. In contrast, $^{13}$C nuclei exhibit long $T_1$ values even in the presence of radicals, making them ideal targets for DNP experiments.

To quantify these effects, the longitudinal relaxation time constants ($T_1$) of 2-$^{13}$C-pyruvate were measured for both $^{13}$C and $^{1}$H nuclei under thermal polarization conditions. Since DNP requires the presence of radicals, the dependence of pyruvate $^{1}$H and $^{13}$C $T_1$ values on the concentration of trityl OX063 in aqueous solution was also measured at 9.4 T using an inversion recovery sequence (described in Section 2.4.7). The results are presented in Figure 4.2.

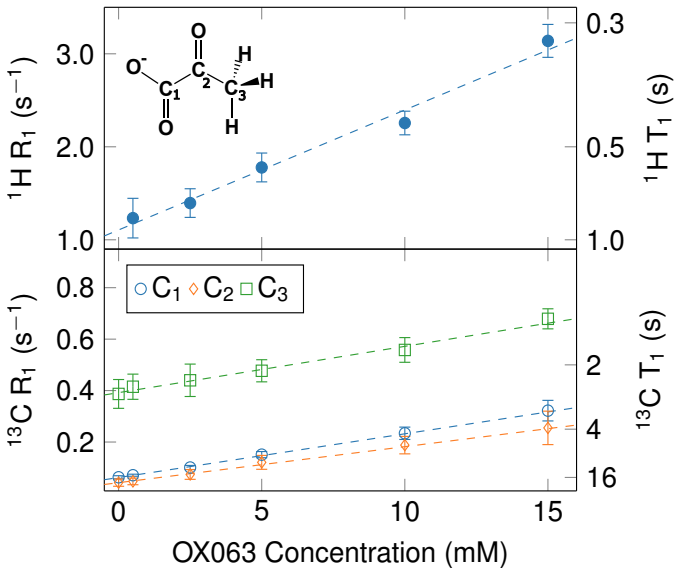


**Figure 4.2.:** This figure has been adapted from publication[76]. Spin-lattice relaxation rates ($R_1$) for pyruvate as a function of OX063 radical concentration, measured at 9.4 T in tris-buffer (pH 7.2). While $^{1}$H relaxation rates exceed 1 s$^{-1}$ and increase rapidly with radical concentration, $^{13}$C relaxation rates remain below 0.6 s$^{-1}$. Dotted lines represent linear fits to the data.

The relaxation rate at each concentration was calculated according to:

$$R(c) = R_0 + m \times c \tag{4.1}$$

where $c$ is the trityl concentration in mmol. The resulting fit parameters and zero-radical $T_1$ values are summarized in Table 4.1.

From these measurements, it is evident that $^{13}$C nuclei, particularly $C_2$, exhibit long $T_1$ even in the presence of trityl radicals, making them ideal targets for DNP. In contrast, $^{1}$H nuclei relax much more rapidly, with $T_1$ values on the order of a few hundred milliseconds in the presence of radicals, limiting their utility for direct detection. In literature, 15 mM of trityl is typically used for DNP. After dilution, this corresponds to approximately 1.5 mM in solution, which is unlikely to induce significant relaxation compared to TEMPOL radicals commonly used at 50 mM. After dilution, the

| Nucleus | $R_0$ ($s^{-1}$) | $m$ ($s^{-1}$/mmol) | $T_1^0$ (s) |
|---|---|---|---|
| $^{1}H$ | 1.106 | 0.129 | 0.904 |
| $^{13}C_1$ | 0.062 | 0.017 | 16.205 |
| $^{13}C_2$ | 0.042 | 0.014 | 23.828 |
| $^{13}C_3$ | 0.392 | 0.018 | 2.550 |

**Table 4.1.:** Fit results from $T_1$ measurements of pyruvate at various OX063 radical concentrations. $T_1^0$ represents the relaxation time in the absence of a radical.

TEMPOL concentration will be 5 mM, which can strongly accelerate relaxation at low millimolar concentrations[83]. These measurements guided the selection of $^{13}C$ as the detection nucleus and the choice of radical concentration for subsequent DNP experiments. Under these considerations, the following section details the optimization of sample formulations and solvent conditions to maximize $^{13}C$ polarization efficiency.

### 4.2.2. DNP Polarization Conditions

Based on the considerations from the previous section, experiments were carried out on $^{13}C$ nuclei of pyruvate. Samples were hyperpolarized in a polarizer (Cryogenic Ltd., UK). Microwave irradiation was provided by a source (Virginia Diodes Inc.) with a nominal output power of 150 mW. The choice of microwave frequency, power, and polarization time depends on the radical type and the target nucleus[67]. In the solid state, DNP spectra were recorded by varying the microwave frequency to identify the optimal irradiation condition, corresponding to the maximum (positive or negative) DNP. For trityl OX063, an optimal microwave frequency of 187.65 GHz was determined for positive DNP. At the chosen frequency, polarization build-up curves were measured to characterize the time dependence of the NMR signal and to define the polarization time required for maximum signal enhancement.

### 4.2.3. DNP Sample Composition

One approach to hyperpolarize nuclei such as $^{13}C$, which are low in abundance and have low $\gamma$ values, was to initially hyperpolarize high-$\gamma$ nuclei like $^{1}H$. This polarization was then transferred to $^{13}C$ using adiabatic transfer[84, 85] or Hartmann-Hahn cross-polarization[86]. Typically, a broadband radical such as 4-Hydroxy-TEMPO (TEMPOL) was used for these methods. However, as previously discussed, this radical causes rapid relaxation during hyperpolarized solid transfer, making it less efficient than a narrow-band radical like trityl OX063[87, 88]. Therefore, the preferred method is to directly polarize $^{13}C$ nuclei with this radical. Additionally, the optimal trityl concentration for $^{13}C$-DNP is one-third of the optimal TEMPOL concentration for $^{1}H$ DNP.

Achieving maximum polarization efficiency in $^{13}C$ DNP depends on effective carbon-carbon spin diffusion, which requires a sufficiently high $^{13}C$ concentration. However, for the Bullet-DNP experiments, highly concentrated samples were intentionally avoided, as the ultimate aim was to detect pyruvate at very low concentrations in the liquid state. Consequently, the sample composition needed to balance two competing requirements: maintaining sufficient $^{13}C$ spins to ensure efficient spin diffusion in the solid state, and keeping the overall ligand concentration low. To identify an optimal formulation, a series of DNP buildup experiments was conducted using different solvent mixtures and spin-diffusing agents, systematically evaluating their influence on polarization level and buildup time.

**Observation** : The following sample and solvent combinations were tested:

In first test (Sample 1), a 1 M solution of 2-$^{13}$C Na-pyruvate in $D_2O$:DMSO-$d_6$ (2:1) was directly polarized. After a buildup period of six hours, the polarization reached approximately 25% (green curve in Fig. 4.4) and the corresponding DNP spectrum is shown in Fig. 4.3 in the same color. However, to attain low concentrations after dilution, only very small (picolitre-sized) samples could be used, since a high initial pyruvate concentration was required for efficient spin diffusion in DNP. However, handling such small samples with precision was not possible in practice. To address this problem, $^{13}$C-labeled spin-diffusion agents were tested. These agents were expected to help transfer polarization across the frozen matrix and allow the use of lower pyruvate concentrations without reducing the overall polarization efficiency.

In second test (Sample 2), 1-$^{13}$C sodium acetate was introduced as a spin-diffusion agent at concentrations up to 1.6 M. At higher concentrations, acetate performed well, but when the pyruvate concentration was kept below 100 µM, the solid-state polarization decreased to about 15% (red curve in Fig. 4.4), and the corresponding DNP spectrum is shown in Fig. 4.3 in the same color. The buildup curve showed a rapid initial increase followed by an early saturation, which was likely caused by partial aggregation of acetate in solution. Although acetate was intended to enhance spin diffusion, the resulting pyruvate polarization indicated that most polarization transfer still occurred primarily between pyruvate molecules. This suggests that acetate was not an effective spin-diffusion agent in the $D_2O$:DMSO-$d_6$ matrix at such low concentrations. The reduced efficiency was likely due to the inhomogeneous distribution of acetate within the frozen glass. Consequently, a different spin-diffusing agent was required to achieve efficient polarization transfer.

In (Sample 3), doubly-labeled $^{13}$C DMSO was employed as a spin-diffusion agent to achieve a more homogeneous distribution of the diffusion species. The pyruvate concentration was maintained at 100 µM, while $^{13}$C DMSO was used at 1 M, and the DNP buildup was recorded under these conditions. This modification significantly improved spin diffusion and increased the $^{13}$C polarization to approximately 35% (blue curve in Fig. 4.4) and corresponding DNP spectra in Fig. 4.3 in the same color.

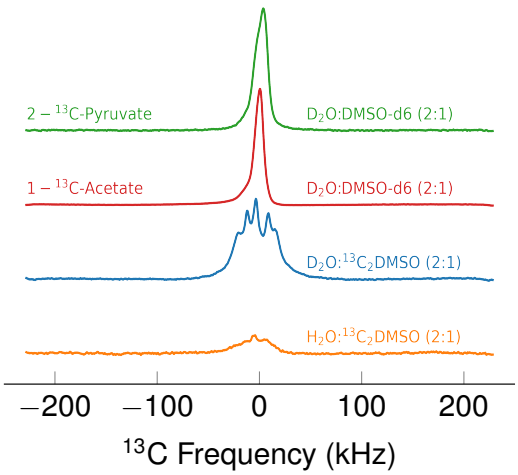


**Figure 4.3.:** $^{13}$C NMR spectra of hyperpolarized 2-$^{13}$C pyruvate samples at the end of the DNP buildup process (6.7 T, 15 mM OX063, 1.5 K). Different solvent formulations are shown, using the same color coding as in Fig. 4.3. Spectra were normalized to sample volume and molarity. Broader lines are observed for $^{13}$C-labeled DMSO compared to 1-$^{13}$C acetate or pyruvate, while deuteration of the water fraction shows only minor effects on lineshape but a pronounced effect on buildup dynamics. This figure has been adapted from publication[76].

Finally, in (Sample 4), $H_2O$ was substituted with $D_2O$ in the formulation used for Sample 3 to investigate the influence of protonation on $^{13}C$ polarization. Since trityl OX063 does not efficiently polarize protons, partial deuteration was expected to reduce the heat load during hyperpolarization and potentially enhance $^{13}C$ polarization. The resulting buildup curve (orange, Fig. 4.4) confirms a modest improvement in achievable polarization levels. The corresponding DNP spectra are shown in Fig. 4.3 in the same color. However, the buildup dynamics were considerably slower in the protonated sample, and even after eight hours, the polarization remained below that of the deuterated counterpart. In contrast, under magic angle spinning (MAS) NMR conditions, these weaker and averaged dipolar interactions facilitate spin diffusion by mediating energy exchange during flip-flop transitions between carbons with different chemical shifts.[89, 90]. These observations indicate that strong proton-carbon dipolar couplings hinder efficient $^{13}C$ spin diffusion. They also highlight the importance of solvent-dependent spin diffusion in efficiently transferring polarization through the frozen matrix.

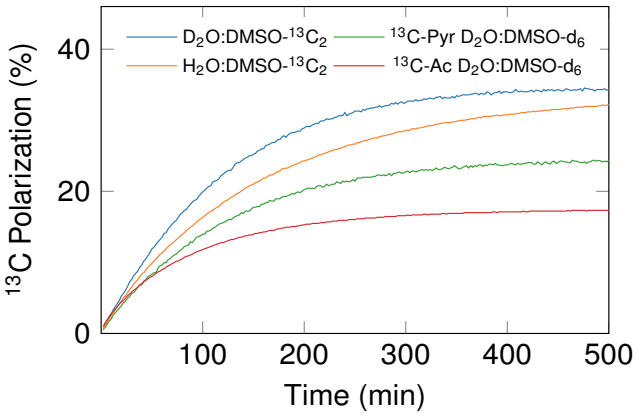


**Figure 4.4.:** This figure has been adapted from publication[76]. DNP buildup curves for 2-$^{13}C$ pyruvate at 6.7 T with 15 mM trityl OX063 at 1.5 K. The curves correspond to different sample formulations: 1 M pyruvate in $D_2O$:DMSO-$d_6$ (Sample 1 = green), 84 mM pyruvate with 1.6 M 1-$^{13}C$ acetate in $D_2O$:DMSO-$d_6$ (sample 2 = red), 100 µM pyruvate in $D_2O$:DMSO-$^{13}C_2$ (sample 3 = blue), and 100 µM pyruvate in $H_2O$:DMSO-$^{13}C_2$ (sample 4 = orange).

In Fig. 4.4, all polarization levels were estimated by comparing the integrated spectral intensities to the thermal equilibrium signal of a 30 µL sample of 1-$^{13}C$ pyruvic acid with 15 mM trityl at 1.5 K, and normalizing for both the $^{13}C$ concentration and sample volume across all four formulations. These buildup curves were repeated to confirm the effect, shown in Fig. 4.5.

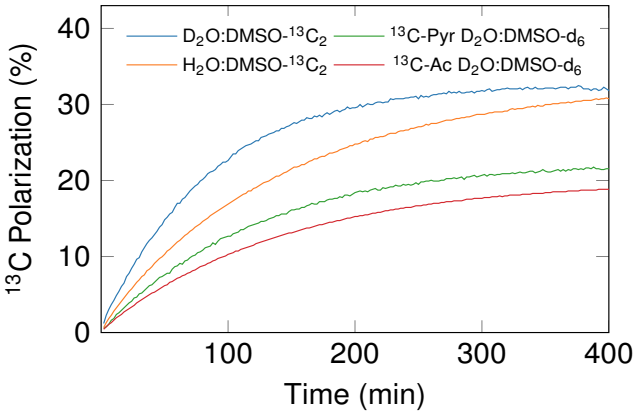


**Figure 4.5.:** Repeat DNP buildup experiments for 2-$^{13}C$ pyruvate under the same experimental conditions and sample formulations as in Fig. 4.4.

**Interpretation:** The results demonstrate a clear dependence of achievable polarization on the choice of spin-diffusion agent and solvent composition:

- Sample 1: Showed high polarization but required impractically small sample volumes to achieve low final concentrations.
- Sample 2: Demonstrated that 1-$^{13}$C acetate was ineffective at low pyruvate concentrations, likely due to inhomogeneous distribution and limited spin diffusion.
- Sample 3: Using $^{13}$C-labeled DMSO, provided both high polarization and improved homogeneity, indicating more efficient spin diffusion through the frozen matrix.
- Sample 4: Partial deuteration slightly enhanced polarization by reducing proton-carbon dipolar interactions, but the buildup was slower due to weaker spin interactions.

The results, shown in Fig. 4.4 and Fig. 4.5, reveal a strong dependence of the attainable polarization level on the choice of diffusion agent, as well as a clear effect of sample deuteration on the buildup dynamics. The corresponding DNP spectra of these buildups are displayed in Fig. 4.3, using the same color coding as the buildup curves. These spectra show the dipolar coupling effect seen in $^{13}$C-labeled DMSO solvents, which is less pronounced in the case of Sample 4. Overall, Sample 3 was identified from these experiments as the optimal formulation for bullet-DNP, balancing polarization efficiency, reproducibility, and minimal sample volume.

### 4.2.4. Sample Preparation

The sample composition optimized in Sample 3 was employed for subsequent DNP experiments, with the aim of detecting pyruvate at sub-micromolar concentrations in a single acquisition. Samples of 2-$^{13}$C sodium pyruvate were prepared at concentrations ranging from 100 µM to 5 mM, depending on the experimental requirements. Radical concentrations of 15 mM OX063 were used, representing an optimized compromise between efficient polarization transfer and minimized relaxation losses. Since the sample also contained $^{13}$C-labeled DMSO. High polarization due to $^{13}$C-DMSO limits the receiver gain during acquisition, making low-concentration pyruvate difficult to detect both the $^{13}$C and $^{1}$H signals in the liquid state.

To minimize this effect, the concentration of the spin-diffusion agent was reduced by preparing small beads of the sample using a sequential layering procedure for liquid-state NMR. This process involved freezing and stacking the layers inside the bullet as described below and shown in Fig. 4.6:

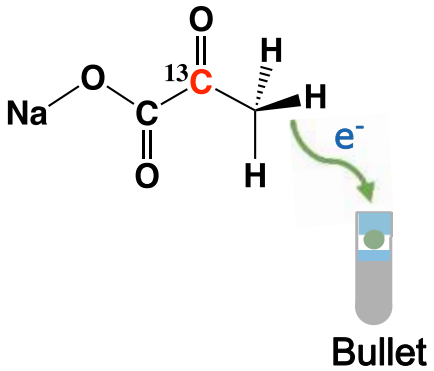


**Figure 4.6.:** Schematic representation of three-layer Bullet sample preparation for DNP

- **Layer 1:** A 5 µL water:glycerol (1:1) bumper layer was first inserted into the bullet and frozen in liquid nitrogen to ensure reliable ejection.
- **Layer 2:** An aliquot (1.5-5 µL) of the pyruvate DNP sample composition was pipetted directly into liquid nitrogen to form a bead, which was then placed as a second layer on top of the first frozen layer.
- **Layer 3:** A final 10 µL of the same solvent composition as the bumper layer was added as a sealing layer to prevent overheating due to microwave during DNP. Care was taken to avoid mixing of the three layers.

These prepared samples were then hyperpolarized and transferred for liquid-state detection afterwards. The detection scheme is described in the following section.

### 4.2.5. Detection Scheme

After completion of the DNP buildup, the bullet was automatically ejected from the polarizer and transferred into an injection device located inside the 9.4 T liquid-state NMR magnet. The bullet's hyperpolarized material was dissolved in 700 µL of buffer and, following a delay of 1 s, the solution was pushed into the NMR tube assembly, and back pressure was applied.

Following dissolution, signal detection was performed in the liquid state. Conventional liquid-state detection in DNP experiments relies on direct observation of the hyperpolarized $^{13}$C nucleus. However, the low gyromagnetic ratio of $^{13}$C limits sensitivity compared to $^{1}$H. To overcome this limitation, a reverse INEPT sequence was implemented to transfer polarization from $^{13}$C to J-coupled protons, enabling indirect $^{1}$H detection. For the substrate 2-$^{13}$C-pyruvate, polarization transfer to the neighbouring methyl protons was simulated using this scheme. The simulations (neglecting relaxation effects) predicted a significantly higher signal-to-noise ratio for indirect $^{1}$H detection via INEPT compared to direct $^{13}$C detection. The corresponding pulse sequence and simulation parameters are described in the following section.

### 4.2.6. Role of $^{13}$C-$^{1}$H Reverse INEPT

The polarization transfer pathway from $^{13}$C to $^{1}$H in 2-$^{13}$C-pyruvate is illustrated in Fig. 4.7.

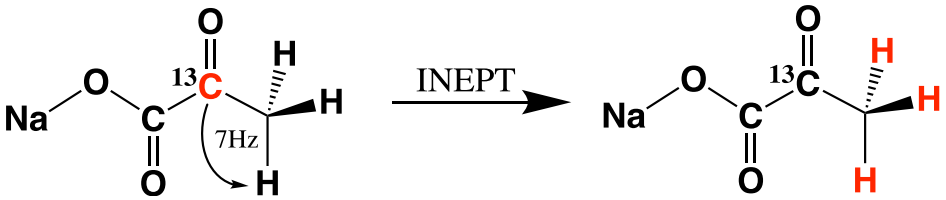


**Figure 4.7.:** Polarization transfer from the $C_2$ carbon of [2-$^{13}$C] pyruvate to the J-coupled (7 Hz) methyl protons in a reverse INEPT experiment.

To transfer the longitudinal polarization of a spin-1/2 nucleus of an isotopic species ($S$ =$^{13}$C) to the transverse magnetization of a set of $N = 3$ magnetically equivalent spin-1/2 nuclei ($I$ =$^{1}$H), the INEPT pulse sequence can be expressed as follows[91]:

$$90_x(S) - \mathrm{DEL1}/2 - 180_x(I,S) - \mathrm{DEL1}/2 - 90_y(I,S) - \mathrm{DEL2}/2 - 180_x(I,S) - \mathrm{DEL2}/2 \tag{4.2}$$

In the absence of relaxation and assuming ideal, instantaneous RF pulses, the polarization transfer from the $S$ spin to $N$ magnetically equivalent $I$ spins can be described by the function[4, 91]:

$$f_N(\theta_1, \theta_2) = (\cos\theta_1)^{N-1} \sin\theta_1 \sin\theta_2, \tag{4.3}$$

where $\theta_1$ and $\theta_2$ represent the flip angles of the $S$ and $I$ spins, respectively. The corresponding heteronuclear Hamiltonian under the high-field, weak-coupling approximation is:

$$H = 2\pi J_{14} I_{1z} S_z + 2\pi J_{24} I_{2z} S_z + 2\pi J_{34} I_{3z} S_z, \tag{4.4}$$

where $I_{kz}$ and $S_z$ are the spin operators of the $^1$H and $^{13}$C, respectively. For the methyl group, all three couplings are equal: $J_{14} = J_{24} = J_{34} = J$. The weak-coupling approximation is valid when the difference in Larmor frequencies of the coupled spins is much larger than the scalar coupling constant:

$$|\nu_i - \nu_j| \gg J_{ij} \tag{4.5}$$

Under these conditions, only the secular $I_z S_z$ terms contribute significantly to the spin evolution, while the non-secular terms ($I_x S_x$, $I_y S_y$) are averaged out in the rotating frame. This approximation simplifies the description of polarization transfer in the INEPT sequence. The detailed derivation and operator evolution using the product operator formalism under this Hamiltonian are provided in Appendix A.8. In addition to this, polarization transfer was also evaluated through simulations performed in SpinDynamica.

Simulations were performed using the SpinDynamica platform (available at www.spindynamica.soton.ac.uk) within Wolfram Mathematica (version 13.0.1; Wolfram Research, Champaign, Illinois, USA). This model shows the evolution of $^{13}$C and $^1$H polarizations during the reverse INEPT preparation block. The DEL1 and DEL2 denote the center-to-center delays of the first and second spin echoes in the sequence. The delays in the sequence were set to DEL1 = $1/(10J)$ and DEL2 = $1/(4J)$, which are appropriate for refocused INEPT transfer from a single carbon spin to the three methyl protons[92]. It should be noted that these delay values depend on the spin system. These values are only relevant when transferring to three protons of the $CH_3$ group. The $CH_2$ and CH groups require different optimal settings.[4]. The code for this simulation is provided in Appendix A.8.

The pulse sequence used for this transfer is illustrated in Fig. 4.8 (a) and (b), showing the simulated coherence transfer pathways from $^{13}$C to $^1$H. Panel (c) presents the simulated expectation values of the transverse magnetizations, $I_y$ and $S_y$, during the transfer. These values are normalized to the thermal equilibrium longitudinal magnetization of $^{13}$C and $^1$H, respectively.

Since the gyromagnetic ratio of $^{13}$C is approximately one-fourth that of $^1$H, the maximum polarization transfer efficiency is correspondingly limited. In a methyl group, this transferred magnetization is further distributed among three magnetically equivalent protons, so that each proton receives roughly one-twelfth of the initial $^{13}$C polarization (i.e., a factor of 1/4 from the gyromagnetic ratio and 1/3 from the spin multiplicity). When summed over all three protons, the total $^1$H magnetization becomes comparable to that of the initial $^{13}$C spin, consistent with the relative amplitudes shown in Fig. 4.8(c), where the simulated $I_y$ signal was scaled by a factor of 10 for visual comparison.

After simulating these values, the next step was to experimentally verify the expectation values, as explained in the following section.

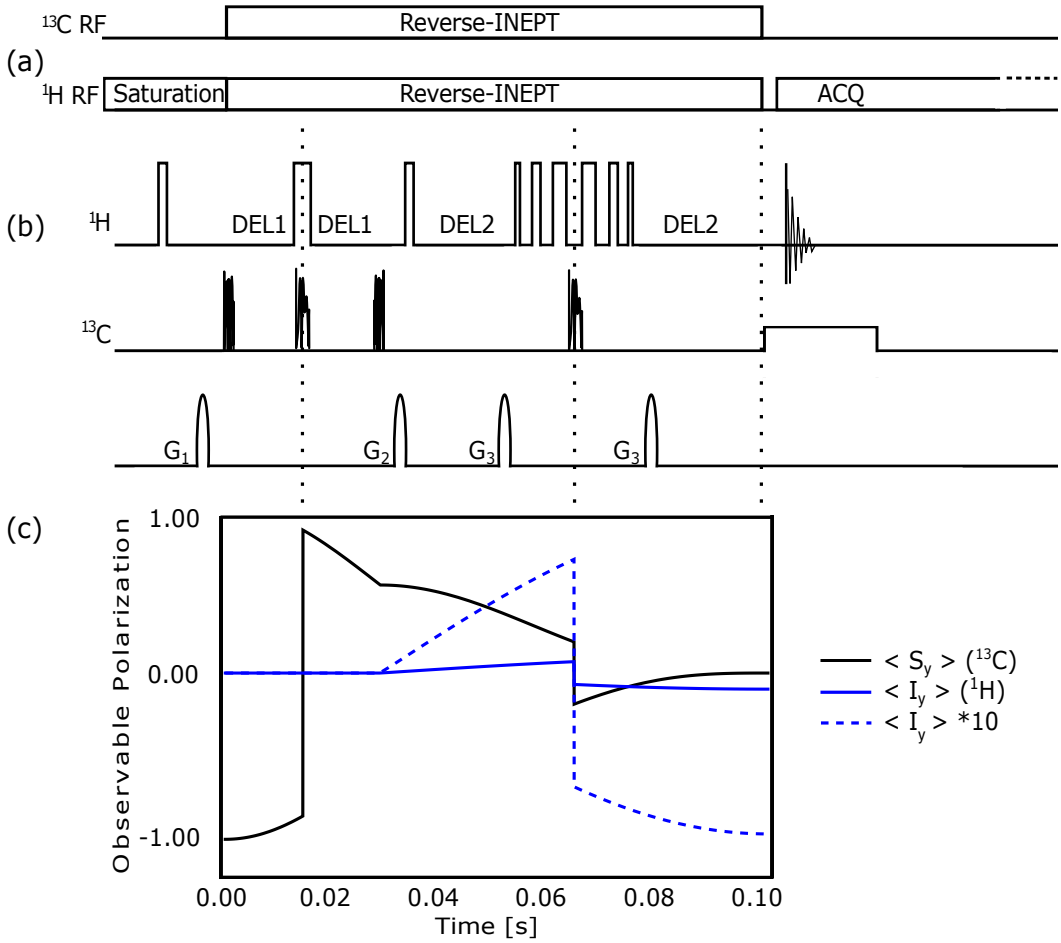


**Figure 4.8.:** This figure has been adapted from publication[76]. Reverse INEPT pulse sequence. (a) The INEPT pulse sequence used in this work comprises a saturation block, in which the proton spins are saturated, a reverse INEPT block, in which polarization is transferred from carbon to protons, and an acquisition block. Panel (b) shows the pulse sequence for the reverse-INEPT module shown in panel (a). The broader bars are 180° and the narrow ones represent 90° pulse, respectively. In order to suppress water, the WG3919 pulse was used as a second 180° on $^{1}$H. On the $^{13}$C channel, the first and second 90° shape pulses are excitation and flip-back pulses. The first 180° shape pulse was the refocussing pulse. Band-selective pulses of the Q5 sebop (350 µs) and Q3 surop (270 µs), both with approximately 8 kHz excitation bandwidth as implemented in the Bruker library, were used for selective excitation and inversion of methyl and carbonyl nuclei. Pulsed-field gradients were applied with the following relative strengths: G1: 61%, G2: 35%, G3: 79%. Phase cycling was not used in this single scan experiment with DNP enhancement. Panel (c) shows a SpinDynamica[93] simulation of the expectation values of the transverse magnetization during the reverse INEPT block[4, 91].

## 4.3. Results

### 4.3.1. Sensitivity gain of INEPT

The sensitivity of $^{13}$C detection was compared directly to that achieved by transferring polarization to protons via the reverse INEPT sequence. The corresponding spectra for 2-$^{13}$C pyruvate are shown in Fig. 4.9. At 9.4 T and thermal equilibrium, a $\pi/2$ pulse was applied for direct $^{13}$C detection, yielding an SNR of 27. Similarly, for the$^{1}$H detection yielded an SNR of 2900. When starting from $^{13}$C polarization, reverse INEPT transfer produced an $^{1}$H signal with an SNR of 230, i.e., an approximately 12-fold reduction with respect to the $^{1}$H thermal equilibrium signal, but an approximately 8-fold increase over the $^{13}$C SNR.

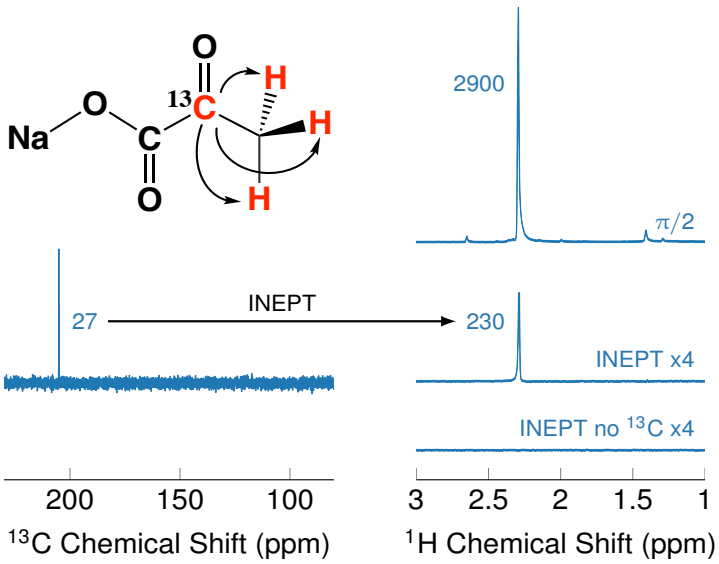


**Figure 4.9.:** This figure has been adapted from publication[76]. Sensitivity comparison for 2-$^{13}$C pyruvate. Direct $^{13}$C spectrum (SNR = 27). Proton detection: thermal $^{1}$H (top, SNR = 2900), reverse INEPT transfer (middle, SNR = 230), and signal disappearance when carbon RF is turned off (bottom). Eight scans were acquired for each trace, the receiver gain was kept constant, and a 1 Hz exponential line broadening was applied during processing.

The signal indeed originates from the $^{13}$C magnetization, as it vanishes when the carbon RF power is set to zero. Both the INEPT-transferred and control spectra (no carbon RF) were scaled by a factor of four. The experimentally observed sensitivity gain closely matches theoretical predictions and SpinDynamica simulations. While the reverse INEPT sequence provides a significant enhancement in sensitivity for indirect $^{1}$H detection compared to direct $^{13}$C observation, the overall performance also depends strongly on the probe design.

#### 4.3.1.1. Sensitivity Gain of INEPT for Different Probes

The sensitivity of an NMR experiment depends critically on the probe's coil geometry, tuning configuration, and RF efficiency. Using the principle of reciprocity[7, 94], the SNR can be estimated from the RF pulse duration and applied power. Therefore, to accurately assess the INEPT sensitivity gain, it is essential to account for the characteristics of the probe used for detection.

Commercial probes from Bruker are typically available in two configurations: **TBI** and **BBO**. The TBI (Triple-resonance Broadband inverse) probe features an inner coil optimized for $^{1}$H detection and an outer coil for broadband nuclei such as $^{13}$C, providing excellent proton sensitivity but reduced efficiency for direct $^{13}$C detection. In contrast, the BBO (Broadband Observe) probe places the $^{13}$C coil in the inner position, thereby offering improved performance for carbon detection at the expense of slightly lower proton sensitivity.

In our setup, the 400 MHz BBO probe exhibits a $^{13}$C $\pi/2$ pulse duration of 10 µs at 50 W. However, the data shown in Fig. 4.9 were acquired using a TBI probe, which requires a $^{13}$C $\pi/2$ pulse of 15.8 µs at 75 W. Since the RF field strength $B_1$ scales with $\sqrt{P}$[7], the expected $\pi/2$-pulse duration of the TBI probe at 50 W is:

$$\tau_{\pi/2} = \frac{15.8}{\sqrt{50/75}}\,\mu\text{s} \approx 19.4\,\mu\text{s}.$$

Thus, for the same RF power, the TBI probe produces a $B_1$ field approximately half as strong as the BBO probe. Consequently, the induced voltage and hence the attainable $^{13}$C signal-to-noise ratio on the TBI probe is about half that of the BBO probe. Considering this difference, the measured INEPT sensitivity gain of $230/27 \approx 8.6$ on the TBI probe corresponds to an effective gain of roughly $8.6/2 \approx 4$ when compared to direct $^{13}$C detection on a BBO probe. This sensitivity can be further enhanced by using a cryoprobe; a detailed comparison of TBI, BBO, and cryoprobe performance is provided in Appendix A.9. Building on these sensitivity optimizations, the next step is to apply the INEPT sequence to hyperpolarized samples, which is discussed in the following section.

### 4.3.2. Hyperpolarized INEPT Experiments and Clinical Relevance

While hardware improvements such as cryoprobes can significantly boost sensitivity, the ultimate relevance of hyperpolarization strategies is determined by their performance under conditions that mimic clinical requirements. In particular, studies of pyruvate metabolism demand sufficient sensitivity not immediately after dissolution, but after a delay period, for instance, one minute, during which metabolic conversion can take place.

In the hyperpolarized experiment described here, the $^{13}$C concentration was relatively high, so sensitivity was not limiting. Therefore, the BBO probe was sufficient to obtain high SNR data. For the experiment, a 4.5 µL bead of 2-$^{13}$C-pyruvate (5 mM) was hyperpolarized, rapidly transferred, dissolved in 700 µL buffer, and subjected to a one-minute delay prior to INEPT-based polarization transfer and $^{1}$H detection. The corresponding spectrum is shown in Fig. 4.10.

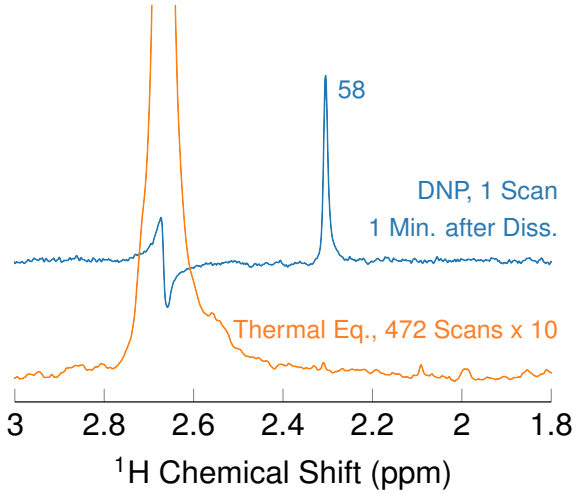


**Figure 4.10.:** This figure has been adapted from publication[76]. $^{1}$H spectrum of 2-$^{13}$C-pyruvate following $^{13}$C hyperpolarization, transfer, dissolution, a delay of 1 minute, and subsequent polarization transfer to protons via INEPT. A line broadening of 1 Hz was applied. The 4.5 µL bead of 2-$^{13}$C-pyruvate (5 mM) yielded a final concentration of 32 µM after dissolution in 700 µL of buffer.

An SNR of 58 was obtained for a final pyruvate concentration of 32 µM. This corresponds to a $^{1}$H signal enhancement of approximately 350, implying a $^{13}$C enhancement of $\sim$ 4000 one minute after dissolution. With a measured $^{13}$C $T_1$ of 24 s, the corresponding initial $^{13}$C polarization at dissolution is estimated to be about 40 %. These results highlight the advantage of the carbon-polarized, proton-detected strategy. After a 1 minute delay, essentially no hyperpolarization would remain in a directly proton-polarized experiment, and direct $^{13}$C detection would yield SNR values 4-8 times lower,

depending on the probe. The use of $^{13}C$ polarization combined with $^{1}H$ detection, therefore, appears to be a great approach for such time-resolved metabolic studies.

It is worth noting that the INEPT strategy has previously been reported to be less effective for imaging applications of hyperpolarized 1-$^{13}C$-lactate at high fields. This limitation arises from the rapid proton $T_2$ relaxation observed *in vivo* (100 ms at 7 T), which causes significant loss of magnetization before INEPT transfer is complete[91]. In contrast, 2-$^{13}C$-pyruvate is more favorable: the $J$-coupling (7 Hz) between its methyl protons and the $^{13}C$ nucleus is nearly twice that of the 1-$^{13}C$-methyl system (4.1 Hz), improving transfer efficiency and making it well suited for the present detection strategy. Having established that a $^{1}H$-based detection strategy provides robust sensitivity even after a 1 minute delay, the next goal was to evaluate the detection limits achievable with the present setup.

### 4.3.3. Pyruvate Detection at Nanomolar Concentrations

For experiments at lower concentrations, where sensitivity becomes more critical, both TBI and BBO probes were compared to evaluate the benefits of probe optimization. The 2-$^{13}C$-pyruvate samples (100 µM) were prepared in Sample 3 solvent for DNP. Bullets were prepared using the bead volumes ranging from 1.5 to 3 µL, following the procedure described in Section 4.2.4. After dissolution, the samples were detected via the INEPT sequence in the liquid state.

The resulting $^{1}H$ spectra acquired with the BBO probe are shown in Fig. 4.11. The methyl signal of pyruvate appears at 2.3 ppm, while an antiphase signal originating from the DMSO solvent used as a spin-diffusing agent is observed at 2.6 ppm. Line broadening of 2 Hz was applied during processing. Pyruvate signals were clearly detectable at concentrations of 420 nM and 350 nM, whereas at 100 nM only a weak indication of the signal could be observed.

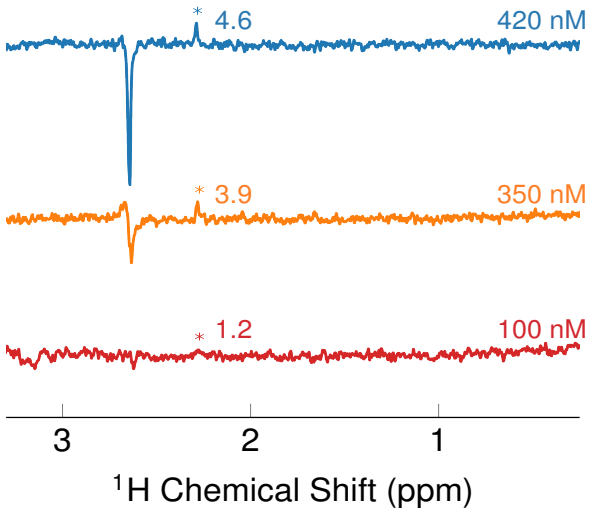


**Figure 4.11.:** This figure has been adapted from publication[76]. Hyperpolarized $^{1}H$ spectrum of 2-$^{13}C$-pyruvate acquired with a BBO probe. The methyl resonance appears at 2.3 ppm; the antiphase peak at 2.6 ppm corresponds to the DMSO solvent. From top to bottom, the spectra correspond to: a 3 µL bead of 100 µM pyruvate (after dilution 420 nM); a 2.5 µL bead of 100 µM pyruvate (after dilution 350 nM); and a 1.5 µL bead of 50 µM pyruvate (after dilution 100 nM).

To further improve sensitivity, identical experiments were performed using the TBI probe, which is more favorable for $^{1}H$ detection. As discussed earlier, this probe is expected to increase the signal by

approximately 1.5 times, providing a clearer comparison of detection performance at low concentrations. The pyruvate methyl peak was observed at 2.3 ppm, with an antiphase DMSO signal at 2.6 ppm, illustrated in Fig. 4.12. A 2 Hz line broadening was applied during processing,

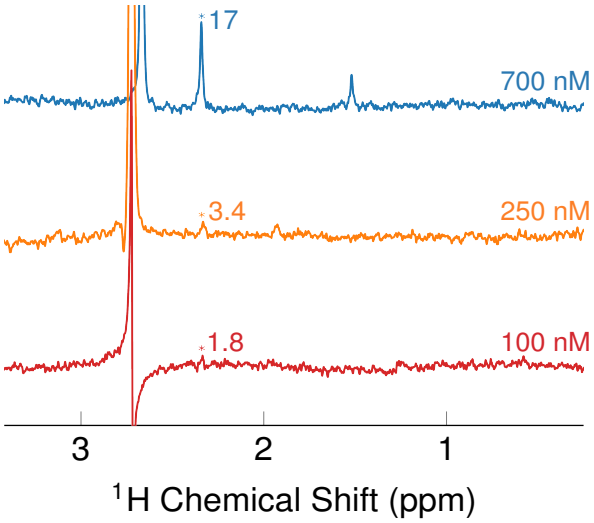


**Figure 4.12.:** $^1$H spectra of 2-$^{13}$C-pyruvate recorded with a TBI probe following $^{13}$C hyperpolarization, dissolution, and INEPT-based polarization transfer. From top to bottom, the spectra correspond to: a 5 µL bead of 100 µM pyruvate (final concentration 700 nM); a 1.75 µL bead of 100 µM pyruvate (final concentration 250 nM); and a 1.5 µL bead of 50 µM pyruvate (final concentration 100 nM). Adapted from Narwal et al.[76].

These spectra demonstrate the detection of pyruvate at lower nanomolar concentrations. The use of the TBI probe approximately doubled the SNR ratio compared to the BBO probe. Using the TBI probe, pyruvate was reliably detected at concentrations approximately 700 nM with an SNR of 10 and at as low as 250 nM with an SNR of 3.4, which corresponds to a detection mass of just 20 ng (180 pmol). At 100 nM, a weak peak was still visible, though the calculated SNR fell below the detection threshold of 3[95]. The spectra also revealed the pyruvate methyl resonance at 2.3 ppm and a small antiphase signal from DMSO near 2.6 ppm. The SNR was not strictly proportional to the concentration, which can be attributed to differences in shimming conditions across experiments. These results are consistent with the sensitivity comparison summarized in Appendix (Table A.1), confirming the expected two-fold improvement of the TBI probe over the BBO probe.

In summary, the optimized bullet-DNP protocol and detection strategy enable single-shot measurements of sub-micromolar pyruvate, with robust detection achieved down to 250 nM. At higher concentrations, such as 32 µM, hyperpolarized pyruvate remains observable even 1 minute after dissolution with SNR > 50 (Section 4.3.2). These results highlight the broad potential of bullet-DNP for studying *in vivo* imaging processes at extremely low concentrations, extending well beyond the capabilities of conventional DNP or dissolution-based methods. To further explore the applicability of INEPT and this method, a complex mixture of amino acid samples was chosen for analysis, as discussed in the following section.

### 4.3.4. Extension to Amino Acid Mixtures

For the experiment, a mixture of four amino acids was selected: 1-$^{13}$C Glycine, 6-$^{13}$C Isoleucine, 6-$^{13}$C Leucine, and 1-$^{13}$C Alanine. The amino acids are shown in Fig. 4.13, (a) $^{13}$C-labeled carbons

are highlighted in red, from which the polarization will be transferred, while panel (b) indicates the corresponding $^{1}$H nuclei to which polarization is transferred via INEPT.

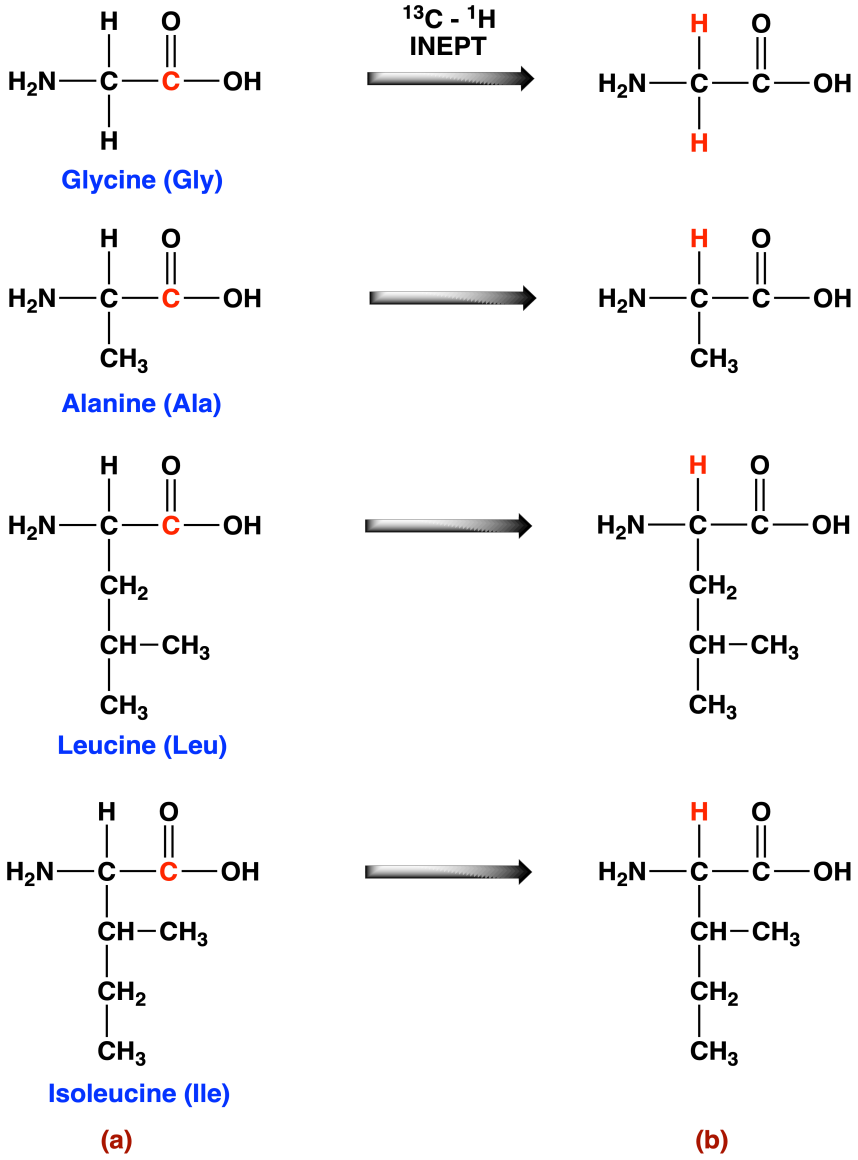


**Figure 4.13.:** (a) Representation of the amino acids showing the $^{13}$C carbon from which the polarization will be transferred (red) and the protons detected via INEPT transfer (blue arrows).

A sample mixture containing 1-$^{13}$C Glycine (1.3 mM), 6-$^{13}$C Isoleucine (1.2 mM), 6-$^{13}$C Leucine (1.7 mM), and 1-$^{13}$C Alanine (1.1 mM) in $D_2O$/DMSO (2:1) was prepared for the DNP step. The narrow-band radical trityl was again used at a concentration of 15 mM, and carbon spin diffusion was again facilitated by adding 1 M doubly labelled DMSO-$^{13}$C same solvent composition as used for pyruvate. A volume of 10 µL of the sample was used as the first layer. For the second layer, water : glycerol (1:1) was replaced with 10 µL $D_2O$ : DMSO (2:1), which was added on top to seal the sample and limit sample heating during transfer. The reason behind this modification was the overlapping of the $^{1}$H signal of glycerol with amino acid signals. Care was taken to prevent mixing of the sample and the final layer during freezing the sample.

The bullet was hyperpolarized for approximately 6 h and subsequently transferred into an injection device inside the 9.4 T liquid-state NMR magnet, as described earlier. The volume of liquid used for dissolution was 700 µL, resulting in concentrations of the amino acids of approximately 20 µM. For liquid-state detection, the INEPT sequence was modified to refocus all the $J$-coupling in a single experiment.

The four amino acids exhibit different $J$ couplings and proton multiplicities, which require careful optimization of the INEPT transfer delays. To achieve efficient polarization transfer, the delays were set to DEL1 = 1/6 $J$ and DEL2 = 1/4 $J$, with $J$ = 7 Hz. The shorter DEL1 = 1/6,$J$ was chosen to achieve selective polarization transfer to a single proton in CH moieties and to the equivalent protons in the $CH_2$ group of glycine.

The experiment was conducted using the BBO probe, which is more sensitive to $^{13}C$. A $^{13}C$ spectrum and a $^{1}H$ spectrum were recorded sequentially on a single hyperpolarized sample. A 15° flip angle pulse was used for $^{13}C$ excitation. After acquiring the $^{13}C$ signal, an INEPT transfer was performed, and the proton signals were observed. The resulting spectra are shown in Fig. 4.14. The amino acids are readily detected both in the proton and the carbon spectra at low micromolar concentrations. The signal intensities are within the expected range for the $^{13}C$ spectrum as well as for the $^{1}H$ spectrum.

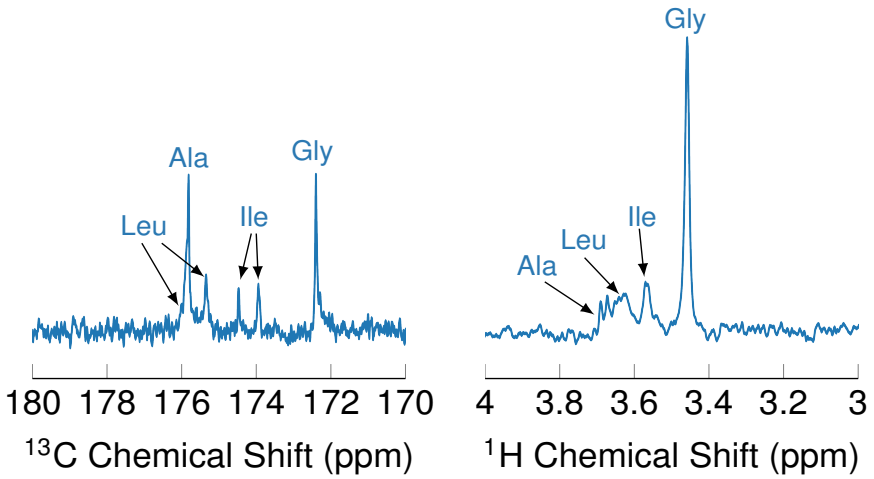


**Figure 4.14.:** This figure has been adapted from publication[76]. $^{13}C$ (left) and $^{1}H$ (right) spectra of a hyperpolarized amino acid mixture. The amino acid concentrations after dissolution are: Gly (19 µM), Ile (17 µM), Leu (24 µM), and Ala (16 µM).

Due to different numbers of nuclear spins that are coupled to the detected $^{13}C$ and $^{1}H$, different multiplicities in the signal were observed. The $^{13}C$ signal assignment is Gly (172.4 ppm), Ile (doublet, 174.47, 174.97), Leu (doublet, 175.88, 175.35), and Ala (175.82 ppm). The observed doublets arise from scalar coupling with neighboring carbons. One of the Leu doublet peaks is masked by the Ala peak. The $^{1}H$ INEPT spectrum shows a singlet due to the two Gly-$C_\alpha$ protons (3.44 ppm), a doublet for Ile-$C_\alpha$ proton (3.55 ppm), a triplet due to the Leu-$C_\alpha$ proton (3.61 ppm) and a quartet due to the Ala-$C_\alpha$ proton (3.66 ppm).

This experiment demonstrates that direct $^{13}C$ detection combined with INEPT-based $^{1}H$ detection allows sensitive and simultaneous observation of multiple $^{13}C$-labeled amino acids in a complex mixture at low micromolar concentrations. The approach provides a clear resolution of individual compounds, enabling detailed analysis of mixtures.

## 4.4. Conclusion and Outlook

In conclusion, this work has demonstrated that bullet-DNP, combined with $^{13}C \rightarrow ^{1}H$ polarization transfer, enables highly sensitive NMR detection of mass-limited samples down to the nanomolar regime. The developed methodology provides reproducible and efficient hyperpolarization, facilitating the detection of 2-$^{13}$C-pyruvate and amino acid mixtures at sub-micromolar concentrations. Furthermore, the approach retains sufficient polarization for time-resolved measurements, even after delay periods relevant to physiological processes.

While the present study establishes the experimental framework and demonstrates its applicability, several avenues exist for further improvement. Detection at higher magnetic fields and the use of cryoprobes could further enhance sensitivity, potentially reducing the detection limit to approximately 30 nM. Moreover, automated and serial implementations of the bullet-DNP process could substantially increase experimental throughput and repeatability. The improved sensitivity of bullet-DNP also opens possibilities for metabolic imaging applications, allowing longer observation times for *in vivo* processes, enabling investigations of biomolecules.

In addition to these methodological advances, the results demonstrated here provide promising opportunities for ligand-protein binding studies that are relevant to drug discovery. Bullet-DNP's ability to detect NMR signals at nanomolar concentrations makes it a powerful tool for probing low-affinity complexes that are typically difficult to conventional NMR techniques. In the following chapter, this potential is demonstrated through the investigation of pyruvate binding to target proteins using field-dependent relaxation measurements. This bridges the methodological developments reported here to their broader application in drug discovery.

# 5. Bullet-DNP and Low-Field Relaxation for the Detection of Ligand-Binding

The content of this chapter is based in part on the publication in Ref. [96].

## 5.1. Introduction

Ligand-protein interactions are fundamental to nearly all biological processes and are central to the field of drug discovery. Detecting and characterizing these interactions requires methods capable of probing binding even at low ligand concentrations, preferably in solution and without chemical modification of the binding partners. NMR spectroscopy is particularly effective for this purpose, as it can provide atomic-level insights into weak and transient binding events. Over the years, numerous ligand-observed NMR techniques have been developed that exploit changes in relaxation or NOE-based magnetization transfer upon binding.

The most commonly used methods include saturation-transfer difference (STD), water-LOGSY, and transverse relaxation-based methods such as $T_2$/CPMG. In STD, magnetization is transferred from a saturated protein to a bound ligand. If binding occurs to the protein, the ligand will be affected by the protein saturation, leading to a decrease in the signal of the free ligand[97]. Water-LOGSY distinguishes free and bound ligands via the NOE sign arising from water saturation[98]. $T_2$-based methods, including CPMG, exploit the faster transverse relaxation of bound ligands[92].

A major limitation of these techniques is their inability to reliably identify ligands with very high affinity, as such interactions do not involve the rapid exchange upon which these methods depend. To address this, competition-based methodologies were developed, in which a low-affinity, observable "reporter ligand" is displaced by a high-affinity ligand.[99] This indirect detection strategy significantly broadens the range of ligands that can be identified by NMR screening, including otherwise "invisible" tight binders, and has proven especially useful in high-throughput applications. Despite these methodological advances, ligand-observed techniques typically depend on strong ligand signals, typically requiring ligand concentrations $\geq 200$ µM and protein concentrations of approximately 20 µM. These requirements present challenges, particularly for proteins that are difficult to express in large quantities and incur high costs, such as those produced in mammalian or insect cell systems.[100]

Several methods have been developed to reduce these concentration requirements. For instance, the PEARLScreen method lowers the protein requirement to 1 µM, but still demands high ligand concentrations (~200 µM) and high-field instrumentation ( $\geq 600$ MHz ) for sufficient sensitivity.[101] Hyperpolarization methods provide another promising avenue. SABRE-based approaches, for e.g, have enabled fluorine-detected binding studies at low micromolar concentrations, where changes in $^{19}$F or $^{13}$C relaxation upon binding could be monitored.[102, 103] Despite these advances, challenges remain for non-fluorinated ligands or for site-specific studies at natural isotopic abundance. Moreover, the use of

$^{1}$H detection has been limited by the intrinsically fast relaxation of protons in the hyperpolarized state. This is a significant drawback, since $^{1}$H detection provides intrinsically greater sensitivity and small fractions of bound ligand can induce measurable changes in proton transverse relaxation rates ($T_2^{-1}$).

Chapter 4 demonstrated that bullet-DNP hyperpolarization, combined with $^{13}$C-$^{1}$H polarization transfer, enables highly sensitive detection of hyperpolarized pyruvate. Using this approach, hyperpolarization survives on $^{13}$C even after clinically relevant delays. These results established the feasibility of carbon-polarized, $^{1}$H-detected strategies for imaging applications and suggested that such approaches could be extended to ligand-protein interaction studies. Building on this foundation, the present chapter explores how $^{13}$C hyperpolarization with $^{13}$C-$^{1}$H INEPT transfer and low-field relaxation can be exploited to probe ligand-protein binding.

At low field, the bound ligand relaxes more rapidly due to its slower tumbling (longer correlation time, $\tau_c$) compared to the free ligand[104]. This can cause rapid relaxation and produce a strong signal contrast between free and bound ligand. This contrast improves the detectability of binding, enabling measurements at concentrations as low as 2 µM protein and 14 µM ligand: a 10-fold decrease in protein requirement compared to conventional methods. This strategy combines $^{13}$C selective labeling with the sensitivity of $^{1}$H detection, and can be further exploited using competition-binding experiments, which provide an indirect confirmation of high-affinity ligand interactions. Together, these approaches allow probing interactions at biologically and pharmaceutically relevant concentrations.

To establish the theoretical framework for these experiments, the role of $^{13}$C relaxation due to dipolar interactions with nearby protons, as discussed in Chapter 2, is first reviewed. This concept is then extended to describe how these mechanisms affect ligand relaxation in the bound state. The following sections present both the theoretical considerations and the experimental results for pyruvate-protein interaction studies under hyperpolarized conditions. The theoretical foundation of this chapter relies primarily on the concepts introduced in Refs.[4, 105].

## 5.2. Carbon-13 Relaxation

For $^{13}$C nuclei ($S$-spin), dipolar interactions with directly bonded or nearby protons ($I$-spins) are the main source of relaxation in small molecules. For example, sodium pyruvate contains three carbon atoms, and the longitudinal relaxation rate ($T_1^{-1}$) of the 2-$^{13}$C labeled carbon (carbonyl) is influenced primarily by the three protons of the neighboring methyl group ($C_3$). The $T_1^{-1}$ rate of $^{13}$C can be described by a simple exponential function, as shown in Section 2.4.5. Small molecules such as pyruvate, due to their fast rotational motion, lie within the extreme narrowing regime ($\omega_0\tau_c \ll 1$). In this regime, the relaxation rate for a single $^{13}$C-$^{1}$H spin pair is given by:

$$T_1^{-1} = 3\, b_{IS}^2\, 2\tau_c \tag{5.1}$$

Here, $b_{IS} = \frac{\mu_0}{4\pi}\frac{\gamma_C\gamma_H\hbar}{r^3}$ is the heteronuclear dipolar coupling constant, $\tau_c$ is the rotational correlation time, and the factor 3 arises from the isotropic averaging of the dipolar Hamiltonian in the extreme narrowing regime. For multiple nearby protons, as in the methyl group of pyruvate, the total relaxation rate is obtained by summing over all contributing protons:

$$T_1^{-1} = \sum_{i=1}^{N} 3\, b_{IS,i}^2\, 2\tau_c \tag{5.2}$$

Outside this regime, the spectral density depends on the field. Information about the molecule can now be extracted not only through $\tau_c$ but also regarding the rapid local dynamics at each measured site. When the small ligand binds to biomolecules like proteins, its $\tau_c$ increases, which makes it behave like a protein molecule. Proteins lie outside the extreme narrowing regime. A model-free approach defines relaxation dynamics by incorporating an amplitude factor "$S^2$" into a rigid-rotor spectral density function[106, 107].

The $S^2$ value ranges from 0 to 1, with 0 indicating a completely disordered and anisotropic molecule, while 1 represents an entirely rigid structure with no internal motions. According to Lipari and Szabo, the spectral density can be defined as[105]:

$$J(\omega) = \frac{1}{2\pi}\left[S^2\,\frac{\tau_M}{1+\omega^2\tau_M^2} + \left(1-S^2\right)\frac{\tau}{1+\omega^2\tau^2}\right] \tag{5.3}$$

Here, $(1/\tau = 1/\tau_M + 1/\tau_c)$ represents the effective correlation time for the internal motion. $\tau_M$ is the globular correlation time (e.g., tumbling of proteins), and $\tau_c$ is the internal motion correlation time ( ligand motion, local side chain). The $T_1^{-1}$ and $T_2^{-1}$ relaxation rate for this model without considering chemical shift anisotropy can be given as :

$$T_1^{-1} = \frac{b_{CH}^2}{10}\Big(J(\omega_H-\omega_C) + 3\,J(\omega_H) + 6\,J(\omega_H+\omega_C)\Big) \tag{5.4}$$

$$T_2^{-1} = \frac{b_{CH}^2}{20}\Big(4\,J(0) + J(\omega_H-\omega_C) + 3\,J(\omega_C) + 6\,J(\omega_H) + 6\,J(\omega_H+\omega_C)\Big) \tag{5.5}$$

The relaxation rates for different protein-bound fractions can be calculated as discussed in the following section.

### 5.2.1. Calculation of Binding Fraction Effects

The effect of molecular binding on relaxation behavior was evaluated by modeling the system as a weighted average of free and bound states under fast-exchange conditions. For a given bound fraction $f_{\text{bound}}$, the observed longitudinal and transverse relaxation rates were calculated as:

$$T_{1,2}^{-1,\text{obs}}(B_0) = (1-f_{\text{bound}})\,T_{1,2}^{-1,\text{free}}(B_0) + f_{\text{bound}}\,T_{1,2}^{-1,\text{bound}}(B_0) \tag{5.6}$$

where $T_{1,2}^{-1,\text{free}}$ and $T_{1,2}^{-1,\text{bound}}$ represent the relaxation rates for the free and protein-bound states, respectively. The free state corresponds to a rapidly tumbling small molecule characterized by $\tau_c = 10$ ps and $S^2 = 0.05$, while the bound state reflects a motionally restricted complex with $\tau_c = 10$ ns and $S^2 = 0.95$[105].

Three representative binding scenarios were investigated: (i) no binding ($f_{\text{bound}} = 0$), representing the free state; (ii) 50% bound ($f_{\text{bound}} = 0.5$), corresponding to an equal mixture of free and bound species; and (iii) 100% bound ($f_{\text{bound}} = 1.0$), representing complete binding. For the intermediate case, the relaxation rates were computed as

$$T_{1,2}^{-1,50\%} = 0.5\,T_{1,2}^{-1,\text{free}} + 0.5\,T_{1,2}^{-1,\text{bound}} \tag{5.7}$$

For each magnetic field strength in the range 0.1-10 T, $T_1^{-1}$ and $T_2^{-1}$ values were first calculated separately for the free and bound states using the Lipari-Szabo model-free spectral density function.

This approach provides a straightforward means to visualize how binding modifies relaxation dispersion profiles, where a higher bound fraction results in increased $T_2^{-1}$ rate and decreased $T_1$ time constant, aligning with slower overall tumbling and restricted internal motion in the protein-bound complex.

The relaxation rates $T_1^{-1}$ and $T_2^{-1}$ are shown as a function of the applied magnetic field, illustrated in Fig. 5.1. The bond distance between $^{13}$C and $^{1}$H was set to 2 Å, corresponding to the actual distance between the 2-$^{13}$C and the methyl protons of the third carbon in pyruvate.

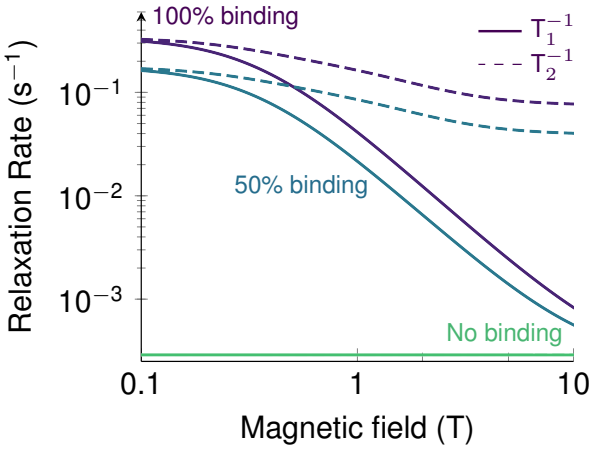


**Figure 5.1.:** $^{13}$C longitudinal ($T_1^{-1}$, solid lines) and transverse ($T_2^{-1}$, dashed lines) relaxation rates as a function of magnetic field for 100 % and 50 % binding. The free ligand relaxation rate is shown in green where $T_1^{-1} = T_2^{-1}$. The calculations correspond to a small molecule ($\tau_c$ = 10 ps, $S^2$ = 0.5) and to the same molecule bound to a protein ($\tau_c$ = 10 ns, $S^2$ = 0.95). Code is provided in Appendix A.10

**Interpretation:**

The relaxation profiles in Fig. 5.1 display characteristic field dependence across different binding fractions. Both the $T_1^{-1}$ and $T_2^{-1}$ relaxation rates decrease monotonically with increasing magnetic field strength throughout the studied range (0.1-10 T), representing the high-field regime of the relaxation dispersion. As the external magnetic field $B_0$ approaches zero, all Larmor frequencies also approach zero ($\omega \rightarrow 0$). Consequently, all $J(\omega)$ terms converge to the same value, $J(0)$. In this limit, the equations simplify to $T_1^{-1} = T_2^{-1}$, so that both rates become identical. At experimentally relevant higher fields, however, $T_2^{-1}$ exceeds $T_1^{-1}$ because it has a strong dependence on $J(0)$, while $T_1^{-1}$ is dominated by frequency-dependent terms.

Binding increases both relaxation rates, with the bound state showing significantly higher $T_1^{-1}$ and $T_2^{-1}$ compared to the free state. Although $T_2^{-1}$ remains larger in absolute values, the **relative contrast** upon binding ( $T_{1,\text{bound}}^{-1}/T_{1,\text{free}}^{-1}$ ) is significant for both rates. This model predicts that binding can substantially enhance both relaxation mechanisms, motivating experimental studies of protein-ligand interactions at low field. Based on this framework, a simple dipolar relaxation model is expected to predict experimentally observable binding effects at 1.3 T. Specifically, $T_1^{-1}$ should show strong relative enhancement upon protein-binding, while $T_2^{-1}$ remains higher in absolute terms. This hypothesis guided the experimental design to probe binding-induced relaxation changes in the model system. To experimentally investigate these binding effects, a well-characterized model system is required, which will be discussed in the following section.

## 5.3. Model System

In this study, the prolyl hydroxylase domain 1 (PHD1; 44 kDa) was examined. PHD1 belongs to the family of non-heme Fe(II)-dependent oxygenases that regulate the stability of hypoxia-inducible factors (HIFs). The enzyme normally contains a catalytic $Fe^{2+}$ center,[108–110] but studies on related isoforms have shown that $Mn^{2+}$ can substitute for $Fe^{2+}$ at the active site. Although this substitution is well documented in the PHD2 isoform[111], the extent to which $Fe^{2+}$ has been replaced by $Mn^{2+}$ in the present PHD1 samples is not known. Consequently, it is unclear whether the $Fe^{2+}$ ion in PHD1 samples has been fully replaced by $Mn^{2+}$. Such substitution inhibits or alters catalytic activity and, from an NMR perspective, is expected to strongly enhance nuclear relaxation due to the pronounced paramagnetic relaxation enhancement (PRE) associated with $Mn^{2+}$[109]. The PHD1 protein used in this study was obtained from a collaborating laboratory at ETH Zürich; detailed procedures regarding its expression and purification are given in Appendix A.11 [96].

PHD1 contains several binding pockets. The native co-substrate of PHD1 is $\alpha$-ketoglutarate ($\alpha$-KG), a five-carbon $\alpha$-keto acid that donates electrons for the hydroxylation of hypoxia-inducible factor (HIF). Pyruvate, although not a natural substrate, shares the same $\alpha$-keto acid functional group and can be considered a structural analogue of $\alpha$-KG. Previous studies have shown that small $\alpha$-keto acids such as pyruvate can act as weak alternative substrates or competitive inhibitors of PHD enzymes.[112] Based on this, pyruvate was chosen as a model ligand due to its small size and long carbonyl carbon $T_1$ in the present study. Ligands typically show different affinities for various protein sites, which are measured by their dissociation constants ($K_d$).

To explore the impact of ligand binding on low-field longitudinal relaxation rates $T_1^{-1}$ for different $K_d$ values, PHD1 is modeled with a rotational correlation time of $\tau_c \sim 10$ ns (estimated from its molar mass). In contrast, a free small ligand such as pyruvate tumbles with $\tau_c$ on the order of tens of picoseconds. Upon binding, the ligand experiences an effective correlation time that is intermediate between its free-state value and that of the protein-ligand complex, due to fast exchange. This substantial change in correlation time directly modulates the relaxation rates of nuclei in the ligand, providing a convenient probe to evaluate protein-ligand interactions. The $T_1^{-1}$ relaxation rates are strongly influenced by ligand binding affinities at low magnetic fields, as the observed relaxation reflects the population-weighted average of free and bound states. This effect can be demonstrated through simulations at 1.3 T, where different dissociation constants ($K_d$) lead to different relaxation effects, as shown in Fig. 5.2.

### 5.3.1. Calculation of $T_1^{-1}$

The dependence of the longitudinal relaxation rate $T_1^{-1}$ on the dissociation constant $K_d$ is modeled using a population-weighted approach that considers the equilibrium between free and protein-bound states. For a given total protein concentration $[P]_T$ and fixed ligand concentration $[L]_T$, the bound fraction $f_B$ is calculated by solving the quadratic equation derived from the binding equilibrium:

$$[PL] = \frac{([P]_T + [L]_T + K_d) - \sqrt{([P]_T + [L]_T + K_d)^2 - 4[P]_T[L]_T}}{2} \tag{5.8}$$

The bound fraction is then computed as:

$$f_B = \frac{[PL]}{[L]_T} \tag{5.9}$$

where $[PL]$ represents the concentration of the protein-ligand complex. The observed relaxation rate is expressed as a population-weighted average of the free and bound contributions:

$$T_1^{-1,\mathrm{obs}}(K_d) = (1 - f_B)\, T_1^{-1,\mathrm{free}} + f_B\, T_1^{-1,\mathrm{bound}} \tag{5.10}$$

Here, $T_1^{-1,\mathrm{free}}$ and $T_1^{-1,\mathrm{bound}}$ denote the intrinsic relaxation rates of the fully free and fully bound states, respectively. The model is evaluated for dissociation constants ranging from $K_d = 1$ to $10^4$ µM, at protein concentrations of 0, 1, and 2 µM, with $[L]_T = 20$ µM fixed throughout.

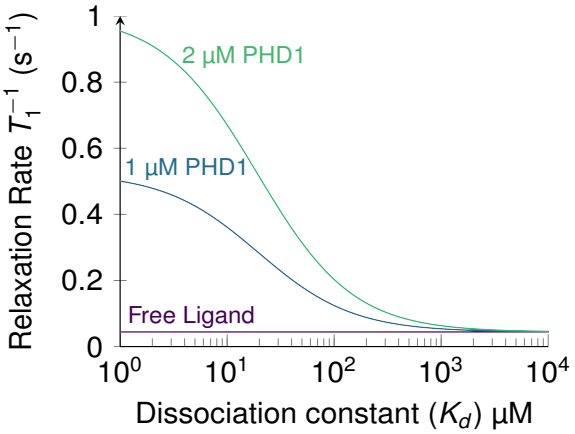


**Figure 5.2.:** Plot of $T_1^{-1}$ vs the binding dissociation constant $K_d$ for a small molecule ($\tau_c = 10$ ps) upon binding with a PHD1 protein of concentration 1 µM to 2 µM at magnetic field of 1.3 T. Code is proided in Appendix A.12.

These simulations do not include paramagnetic relaxation effects from metal centers like Mn, and therefore are generally applicable to systems with similar correlation times ($\tau_c$) and binding affinities. Compounds with strong binding ($K_d = 1$ µM) exhibit significantly faster relaxation even at low protein concentrations (2 µM), compared to weak binders ($K_d = 10^4$ µM) where only a small fraction of ligand is bound.

## 5.4. Experimental Workflow

The experimental workflow consists of four main steps: (i) Sample preparation (ii) hyperpolarization by DNP, (iii) transfer and dissolution at low field with evolution, and (iv) detection at high field. These steps are summarized below, and a schematic representation is given in Fig. 5.3.

(i) **Sample preparation:** The sample was prepared using the optimized sample composition described in the previous chapter, namely $D_2O$:DMSO (2:1) with 1 M doubly $^{13}$C-labeled DMSO as the spin-diffusion agent. A 5 µL bumper layer was first inserted into the bullet and frozen in liquid nitrogen to ensure reliable ejection. A bead-sized 2-$^{13}$C pyruvate stock solution containing 15 mM trityl Ox063 was then prepared and frozen in liquid nitrogen. The pyruvate bead volume was adjusted according to the desired final concentration after dissolution, but the overall preparation followed the same general procedure. This bead was added to the bullet as a second layer. A final 10 µL layer of water:glycerol (1:1) was added to seal the sample and protect it from heating from the microwave.

(ii) **Hyperpolarization (DNP):** In this step, the pyruvate was hyperpolarized for 3-4 hours under cryogenic conditions at a magnetic field of 6.7 T until the desired polarization level was achieved.

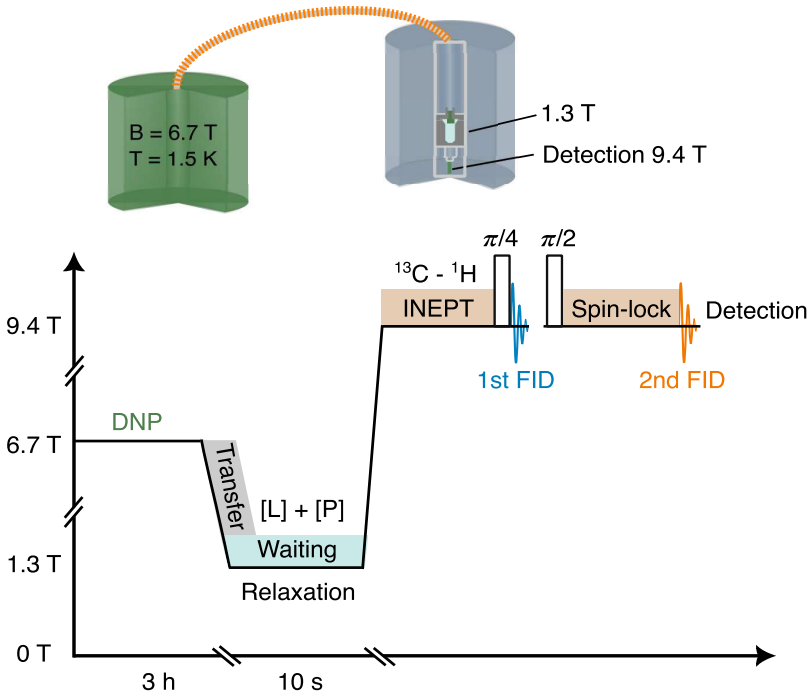


**Figure 5.3.:** Schematic of the experimental workflow: polarization at 6.7 T, transfer through a magnetic tunnel, 10 s evolution at 1.3 T, and subsequent detection at 9.4 T by double acquisition. During the evolution period, bound ligand molecules exhibit accelerated longitudinal relaxation ($T_1^{-1}$) compared to the free ligand, generating $\Delta T_1^{-1}$ contrast. The double acquisition further records the transverse relaxation ($T_2^{-1}$) decay under a 300 ms spin-lock, providing an independent measure of binding.

(iii) **Transfer and dissolution at low field:** After polarization, the sample was rapidly transferred to a liquid-state NMR magnet and dissolved in a solvent ( 50 mM Tris buffer, pH 7.5, 300 mM NaCl ) for the free ligand. During dissolution, the solution was kept at a magnetic field of 1.3 T for 10 s, allowing the ligand to partially relax. This procedure serves as a reference experiment in the absence of protein. In ligand-binding experiments, only the ligand was subjected to hyperpolarization. Subsequently, it was dissolved in the same Tris buffer containing the protein at the desired concentration, and the ligand was allowed to relax in the presence of the protein at 1.3 T prior to detection at 9.4 T.

(iv) **Detection at high field:** Subsequently, the solution was injected into the NMR tube, and detected at a 9.4 T magnetic field using the double acquisition $^{13}$C - $^{1}$H INEPT pulse sequence[76], illustrated in Fig. 5.4.

The INEPT sequence delays used DEL1 = 1/10 $J$ and DEL2 =1/4 $J$ as appropriate for refocused INEPT transfer of polarization from a single carbon spin to the three methyl protons[92]. In the first acquisition, a $\pi/4$ pulse was applied to store half of the $^{1}$H magnetization along the $z$-axis. During the second acquisition, $^{1}$H magnetization was brought back to the x-y plane using a $(\pi/2)_y$ pulse and then subjected to a spin-lock experiment, which measures the $T_2^{-1}$ relaxation rate, which increases upon binding with protein. Binding was further evaluated through competition-binding experiments, where 2-$^{13}$C-pyruvate served as the reporter ligand. Potential competitor ligands were added to the protein sample before each measurement. The competitors and protein were placed in the solvent reservoir, where they waited for the hyperpolarized pyruvate. Upon mixing, the solution evolved for 10 s at 1.3 T before detection at 9.4 T. The competitor ligands, from weak to strong binding affinities, included fumaric acid (fumarate), N-oxalylglycine (NOG), and 2,4-pyridinedicarboxylic acid (PDCA).

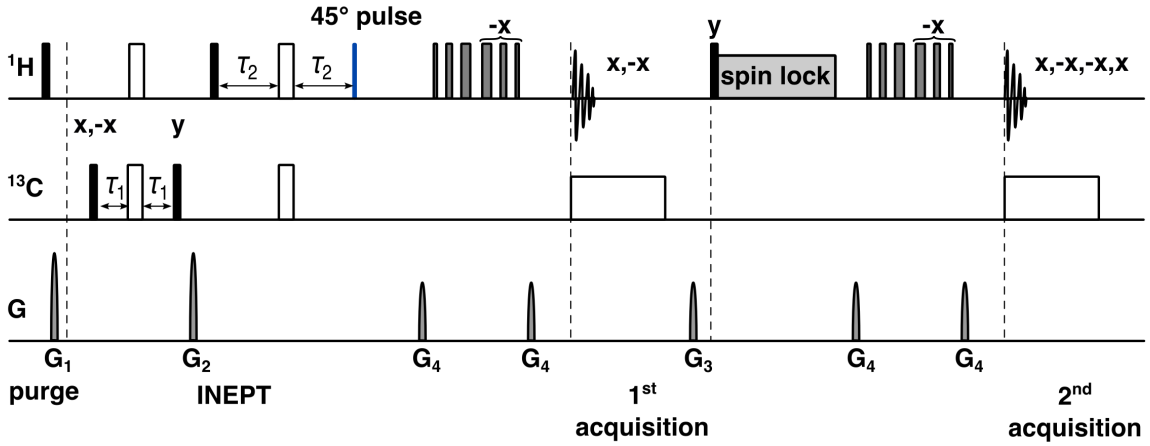


**Figure 5.4.:** The INEPT pulse sequence begins with a $\pi/2$ pulse on $^1$H, placing the proton magnetization in the transverse plane. A reverse INEPT block then transfers polarization from $^{13}$C to $^1$H. The resulting proton magnetization is flipped by a $\pi/4$ pulse (blue), brought back to the $xy$-plane by a subsequent $\pi/2$ pulse, and spin-locked for 300 ms. Broad white bars represent $\pi$ pulses, while narrow black bars denote $\pi/2$ pulses. Water suppression was achieved using a WG3919 pulse (gray) applied as a second $\pi$ pulse on $^1$H.Pulsed-field gradients were applied with the following relative strengths: G1 = 61%, G2 = 35%, and G3 = 79%. No phase cycling was employed in this single-scan DNP-enhanced experiment.

## 5.5. Results & Discussion

For the ligand-binding experiments, it was important to determine both the protein concentration and the duration for which the signal is detectable at low field. To estimate an appropriate waiting time at, the longitudinal relaxation time constant ($T_1$) of free 2-$^{13}$C-pyruvate was measured at 1.3 T.

### 5.5.1. Low-Field $T_1$

For the experiments, 10 µL of 5 mM pyruvate containing 15 mM trityl OX063 was first frozen in liquid nitrogen to form the initial layer. A second layer of 10 µL of water : glycerol (1:1) was then added on top and frozen again. The resulting two-layer sample was polarized and subsequently ejected into 700 µL of Tris buffer. Following hyperpolarization, the sample was transferred as described in Section 5.4, with varying delays of 10, 30, 60, and 90 seconds at 1.3 T. As this experiment did not involve ligand-protein interactions, detection was carried out at 9.4 T using the sequence shown in Fig. 4.8, with only a single INEPT acquisition recorded. For each time delay, liquid-state spectra were recorded using an independent hyperpolarized shot. The pyruvate peak was observed at 2.3 ppm, while the antiphase signal at 2.6 ppm originates from the DMSO solvent, shown in Fig. 5.5. The intensities were normalized to the solid-state polarization to correct for shot-to-shot variation. The final pyruvate concentration after dissolution was 100 µM for all four experiments.

By integrating the methyl peak regions, the data-fitted relaxation curve (Fig. 5.6) gives relaxation time constant $T_1$ = 46 s for free pyruvate at 1.3 T. At short delays, a slightly faster decay was observed than predicted by the exponential fit, likely due to incomplete mixing during dissolution or local radical concentration inhomogeneity. This relatively long $T_1$ indicates that a significant fraction of the polarization remains over a 10 s period, making it a suitable delay for subsequent ligand-binding experiments. However, the overall signal intensity shows a variability of approximately ±20%, likely arising from differences in sample preparation, polarization transfer, and analyte distribution. Such variability raises concerns about experimental reproducibility. Therefore, to accurately estimate the

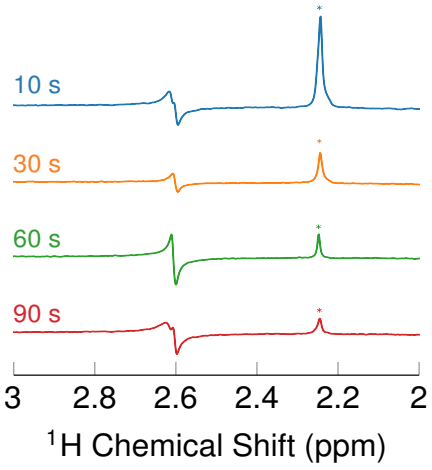


**Figure 5.5.:** $^1$H spectra of 2-$^{13}$C-pyruvate recorded via INEPT transfer at 9.4 T, after different evolution times at 1.3 T.

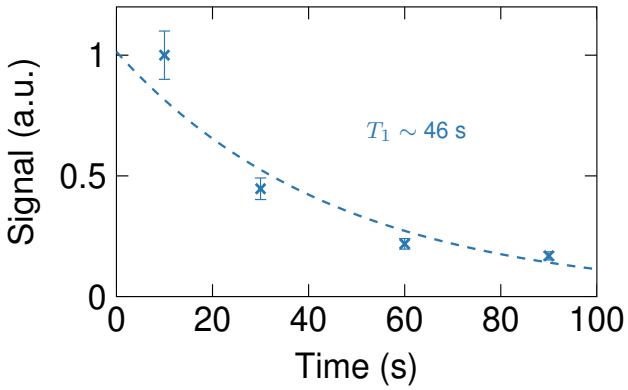


**Figure 5.6.:** Exponential decay fit of signal intensities at 1.3 T with evolution time 10, 30, 60, and 90 seconds. The dashed line represents the best-fit single-exponential model.

error bar at a waiting time of 10 s delay, the experiment was repeated multiple times under identical conditions, as discussed in the following section.

### 5.5.2. Repeatability of Experiments

To evaluate the repeatability of the hyperpolarization experiment, 2 µL of 5 mM 2-$^{13}$C pyruvate was polarized for approximately 3 hours. A fourier transformation of the last FID of the buildup, indicating the final solid-state polarization, is shown in Fig. 5.7 (A). Following transfer, the liquid-state signal was detected using the double-acquisition INEPT sequence depicted in Fig. 5.4. In all cases, the nominal concentration of hyperpolarized 2-$^{13}$C pyruvate in the final solution was 14 µM. Five independent experiments were performed under identical conditions, with a 10 s evolution period at 1.3 T prior to detection. An exponential line-broadening of 5 Hz was applied to all liquid-state spectra for consistency.

The double-acquisition sequence provides two signal intensities per experiment. The first acquisition intensity, $I_1$, reflects the longitudinal magnetization remaining after the 10 s evolution at 1.3 T and therefore encodes information about the $T_1^{-1}$ relaxation rate of the ligand under the given protein concentration. The second acquisition, recorded after a delay $\Delta t = 300$ ms, yields the intensity $I_2$, which

reflects the additional transverse or spin-lock relaxation rates ($T_2^{-1}$ or $T_{1\rho}^{-1}$) occurring during this short inter-acquisition delay. This approach allows the simultaneous evaluation of both longitudinal and effective transverse relaxation processes with a single hyperpolarization shot. These relaxation rates can also be written as:

$$R_1 = \frac{1}{T_1}, \qquad R_{1\rho} = R_2 \approx \frac{1}{T_{1\rho}} \tag{5.11}$$

From this point onward, $R_1$ and $R_{1\rho}$ will be used to denote the relaxation rates, replacing $T_1^{-1}$ and $T_2^{-1}$ for simplicity.

As shown in Fig. 5.7 (A), the solid-state spectra exhibit variations in polarization levels. To allow fair comparison, the liquid-state spectra were normalized using the solid-state integrals. Figure 5.7 (B) presents the methyl region of the $^1$H spectra. The first and second spectra were offset horizontally for clarity. By integrating this region, the mean intensity of the first acquisition across all experiments, $\langle I_1 \rangle$, was calculated. The first-scan intensities were then normalized to this mean, yielding the ratio $I_1/\langle I_1 \rangle$. The first spectrum was obtained after relaxation at 1.3 T. As shown in Fig. 5.7 (C), the normalized intensities approach 1 with a standard deviation of 4.5 %, indicating high repeatability of the first acquisition.

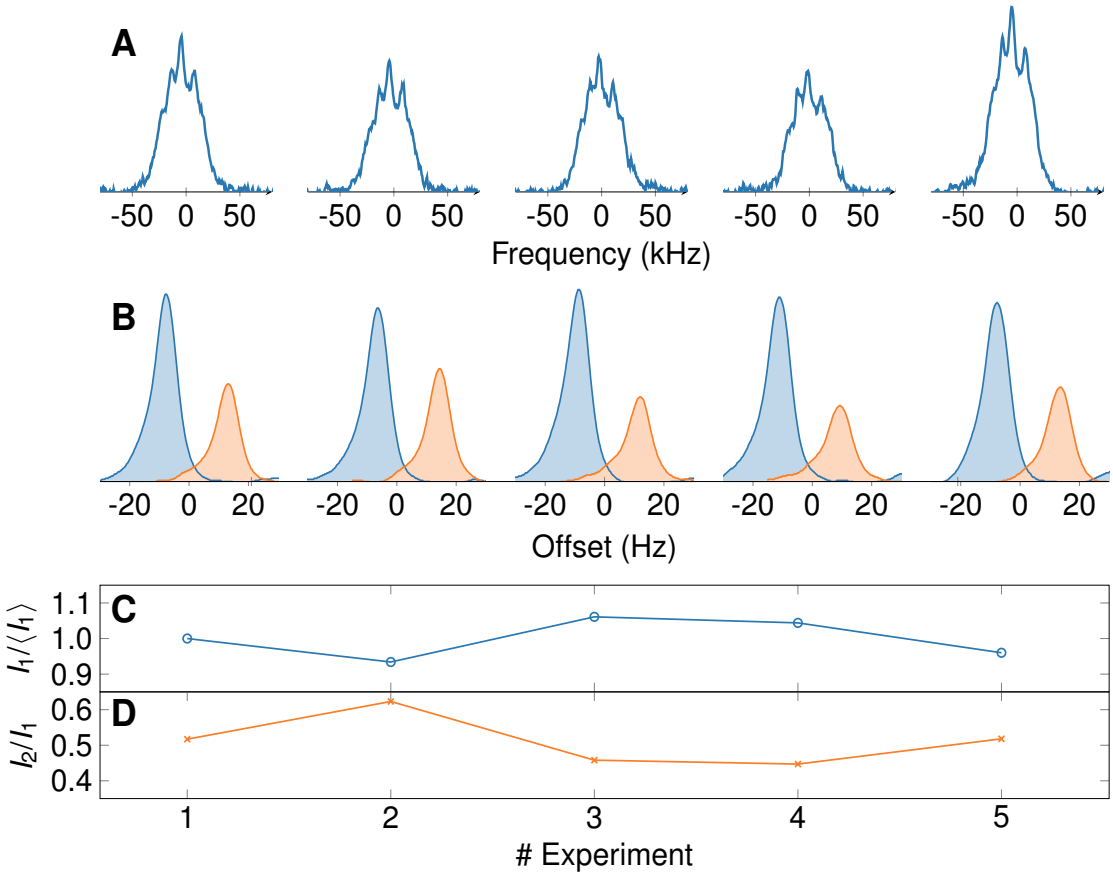


**Figure 5.7.:** Repeatability of hyperpolarized 2-$^{13}$C pyruvate measurements at 14 µM with a 10 s evolution at 1.3 T. (A) Last FID of the solid-state buildup prior to dissolution. (B) Methyl region of the first spectra (blue) and second spectra (orange) in five repeated experiments. (C) First spectra ($I_1$) normalized by their mean $\langle I_1 \rangle$. (D) Second spectra ($I_2$) normalized to the corresponding first spectra.

A second measure of repeatability was obtained from the second acquisition. The ratio $I_2/I_1$ quantifies the relative signal intensity between the two acquisitions. As illustrated in Fig. 5.7 (D), these values show an absolute standard deviation of 6 %. Therefore, the variation for both the first and second spectra remains within ~6 %, confirming the reliability and repeatability of the proposed method. Establishing this high level of repeatability is essential for further ligand-binding experiments. Since low-field relaxation contrast depends on small differences in $R_1$ and $R_{1\rho}$ between free and protein-bound ligands, the small experimental fluctuations observed here ($\leq$ 6 %) ensure that large changes in signal intensity can be confidently attributed to ligand-protein interactions rather than variability in the hyperpolarization or detection process. This provides a solid foundational reference to quantify the effects of binding-induced relaxation in the following experiments.

### 5.5.3. Ligand Binding and Competition at 5 µM PHD1 Concentration

Initial ligand-binding experiments were performed using a PHD1 protein concentration of 20 µM with pyruvate concentration of 100 µM. In the presence of protein, the ligand signal vanished immediately after the hyperpolarized shots, as the protein-bound ligand remained in the solvent reservoir at 1.3 T for approximately 1 s. At this low field, the PHD1 protein exhibits very fast relaxation, causing its signal to disappear within 1 s. Consequently, the protein concentration was reduced to 5 µM, and a 10 s low-field evolution period at 1.3 T was used before detection to ensure measurable signals.

To further characterize this binding interaction, competition-binding experiments were performed sequentially at the same 5 µM PHD1 concentration using competitors of increasing binding affinity. The competitors : fumarate (weak binder, $K_d$ = 200 µM), N-oxalylglycine (NOG; moderate binder, $K_d$ = 60 µM), and 2,4-pyridinedicarboxylic acid (PDCA; strong binder, $K_d$ = 0.4 µM) - were each used at a concentration of 60 µM. Hyperpolarized pyruvate at a concentration of 100 µM was used as a reporter ligand. The observed signals are shown in Fig. 5.8 (A). Each dataset represents an independent hyperpolarization and detection experiment performed under identical conditions using double-acquisition INEPT detection at 9.4 T. All liquid-state integrals $I_1$ (blue), $I_2$ (orange) were normalized by the corresponding solid-state DNP buildup integral to correct for variations in polarization. Data processing included an exponential line broadening of 2 Hz.

To describe the effect of binding on the signal intensities, we define the dimensionless binding scores $Q_1$ and $Q_2$ as:

$$Q_1 = \frac{I_1^c}{I_1^{\text{free}}}, \quad Q_2 = \frac{I_2^c}{I_1^c} \cdot \frac{I_1^{\text{free}}}{I_2^{\text{free}}} \tag{5.12}$$

where $I_1^{\text{free}}$ and $I_2^{\text{free}}$ are the first and second acquisition intensities for the free ligand, and $I_1^c$ and $I_2^c$ are the corresponding intensities in the presence of protein or competitor. $Q_1$ thus reflects the relative change in longitudinal ($R_1$) relaxation after the 10 s evolution at 1.3 T, while $Q_2$ captures the effective transverse ($R_{1\rho}$) relaxation occurring during the 300 ms inter-acquisition delay. Both $Q_1$ and $Q_2$ range from 0 to 1, where $Q = 1$ indicates no binding and $Q < 1$ indicates protein-induced relaxation enhancement. A shift of $Q$ back toward unity upon addition of a competitor indicates successful displacement of the reporter ligand.

As shown in Fig. 5.8 (B) and (C), in the absence of protein, $Q_1$ and $Q_2$ Q were 1 by definition. Upon addition of 5 µM PHD1, $Q_1$ decreased to 0.27 and $Q_2$ to 0.51, indicating substantial enhancement of $R_1$ due to protein binding, while the transverse relaxation rate ($R_{1\rho}$) was comparatively less affected. When fumarate (60 µM) was added, $Q_1$ decreased to 0.16 while $Q_2$ increased to 0.65. The moderate

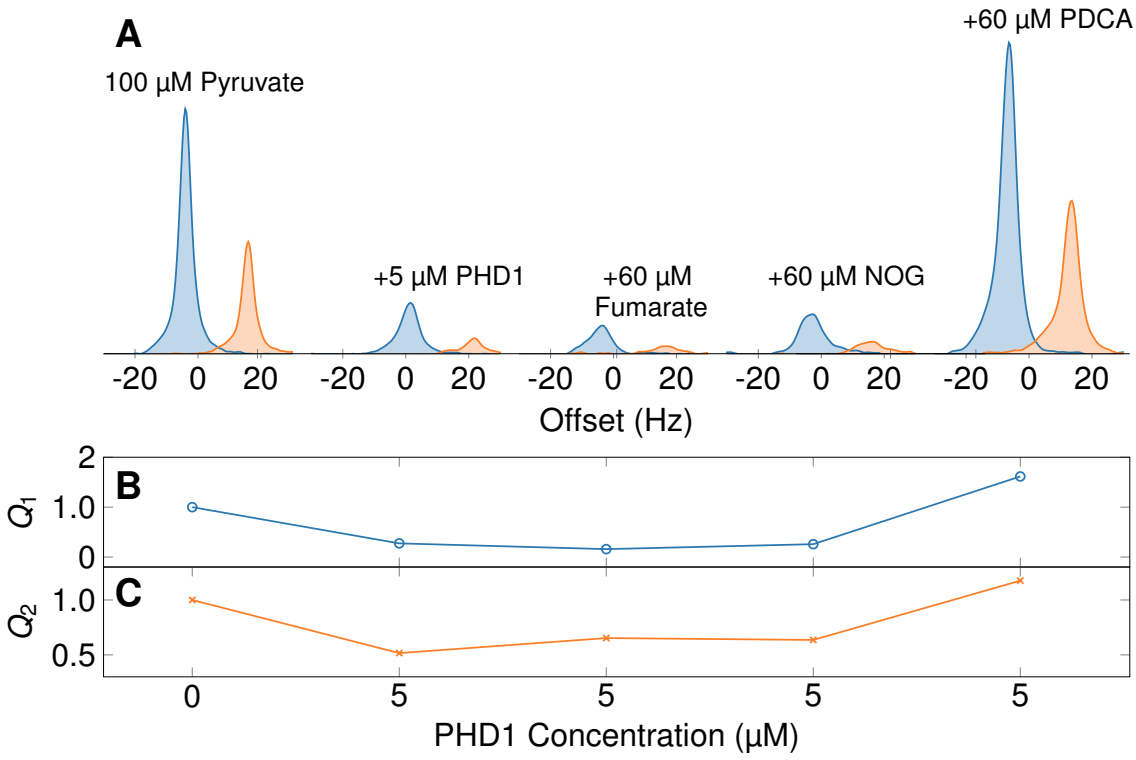


**Figure 5.8.:** (A) 100 µM reporter ligand (pyruvate) dataset acquired after 10 s evolution at 1.3 T, recorded without and with 5 µM PHD1 protein. The measurements were repeated following the addition of competitive ligands of increasing affinity for PHD1: Fumarate (weak binder, 60 µM), NOG (moderate binder, 60 µM), and PDCA (strong binder, 60 µM). Panels (B) and (C) show the resulting $Q_1$ and $Q_2$ scores, respectively, demonstrating a stronger $R_1$ relaxation effect relative to $R_{1\rho}$ for protein-bound 2-$^{13}$C pyruvate.

increase in $Q_2$ suggests partial displacement consistent with fumarate's weak binding affinity. The moderate binder NOG (60 µM) produced $Q_1$ = 0.26. An unexpectedly low $Q_2$ = 0.17, indicating strong transverse relaxation enhancement that contradicts its expected competitive behavior. In contrast, the strong binder PDCA ($K_d$ = 0.4 µM) produced $Q_1$ = 1.6 and $Q_2$ = 1.1. The $Q_2$ value near unity confirms complete displacement of pyruvate and recovery of free-like transverse relaxation behavior. However, the elevated $Q_1 > 1$ value, which theoretically cannot be explained by relaxation effects, indicates a difference in the PDCA experiment that persists despite normalization by solid-state polarization. This could arise from subtle variations in dissolution efficiency, sample transfer, or trityl radical concentration that are not fully accounted for by the normalization. Nevertheless, the key conclusion from the competitive binding series remains robust: PDCA effectively displaces pyruvate, as evidenced by the restoration of $Q_2$ to its free ligand value.

Overall, the contrasts in $Q_1$ and $Q_2$ provided a robust, metric to assess protein-ligand binding and competition using hyperpolarized NMR data. The prominent $R_1$ rate relaxation enhancement observed at 5 µM PHD1 highlights the sensitivity of low-field $R_1$ relaxation rate to protein-ligand interactions. These results indicated that the protein concentration could potentially be further reduced.

### 5.5.4. Binding at Reduced Protein Concentration (2 µM)

To reduce the PHD1 concentration, it was necessary to also lower the ligand concentration, as effective binding requires an appropriate ligand-to-protein ratio. At high ligand excess, the fraction

of bound molecules becomes very small, making the binding-induced relaxation changes difficult to detect against the dominant free ligand signal. To investigate this, hyperpolarized 2-$^{13}$C pyruvate was dissolved in Tris buffer containing PHD1 concentration (1, 1.5, or 2 µM), while maintaining a constant ligand concentration of 14 µM. Spectra were recorded using the double-acquisition INEPT sequence (Fig. 5.4). Each experiment corresponded to a single, independent DNP shot. Liquid-state signals, illustrated in Fig. 5.9, were normalized to the respective solid-state buildup integrals to account for polarization differences between experiments.

Binding was assessed using the intensity ratios $Q_1$ and $Q_2$ defined in the previous section. For free pyruvate, the $Q_1$ and $Q_2$ values were 1 by definition. At 1 µM PHD1, the $Q_1$ value remained close to 1, indicating no measurable interaction at this concentration. This was an unexpected result. As the protein concentration was increased to 1.5 and 2 µM, both $Q_1$ and $Q_2$ decreased and started approaching 0, shown in Fig. 5.9, consistent with increasing relaxation due to binding. At 2 µM PHD1, the $Q_1 = 0.35$ reflects higher low-field $R_1$ relaxation effects in comparison to $R_{1\rho}$ with $Q_2$ value 0.61. The overall signal intensity at this concentration decreased to roughly one-fourth of that observed for free pyruvate.

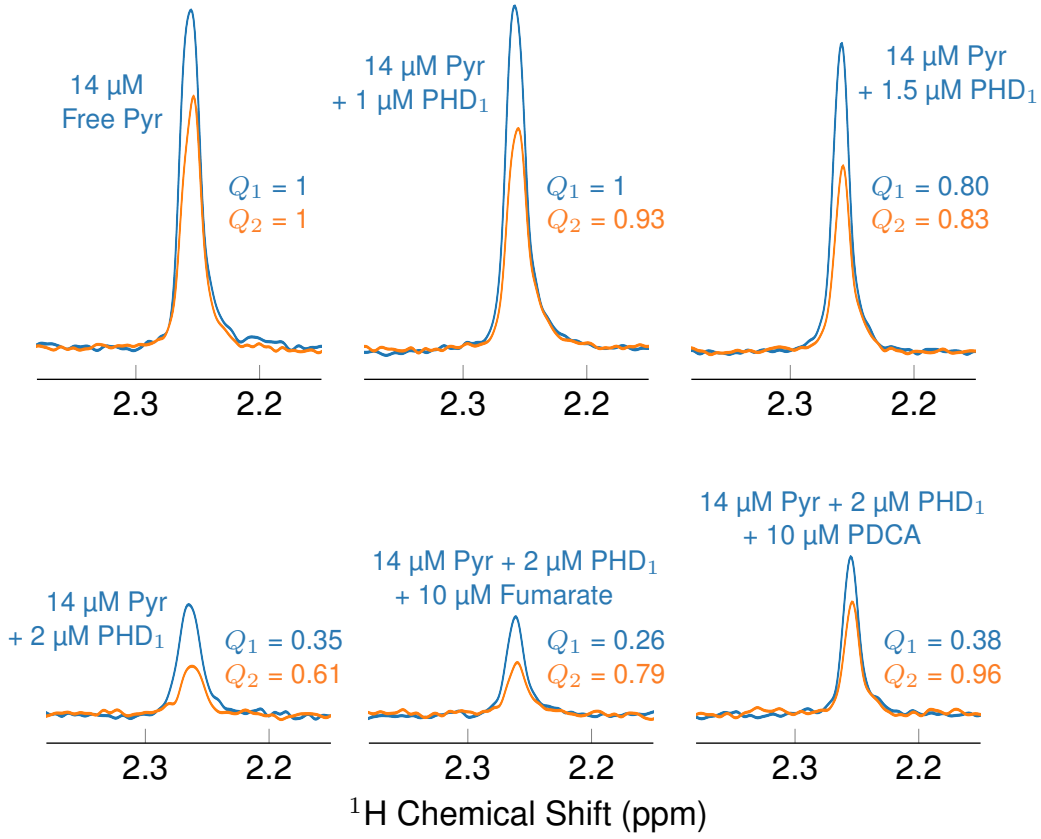


**Figure 5.9.:** First (blue) and second (orange) 14 µM pyruvate dataset acquired after 10 s evolution at 1.3 T, showing the effect of increasing PHD1 concentration (1 to 2 µM) and subsequent addition of competitive binders. The weak binder fumarate (10 µM) produced minimal change, whereas the strong binder PDCA (10 µM) displaced pyruvate completely. The corresponding $Q_1$ and $Q_2$ ratios illustrate the relaxation enhancement and competitive displacement behavior at 2 µM protein concentrations.

To further confirm the binding interaction at 2 µM PHD1, competition experiments were performed with the weak binder fumarate and the strong binder PDCA, both added before dissolution. A low concentration of fumarate (10 µM) produced no observable change, consistent with its weak affinity being insufficient to compete effectively with pyruvate for the limited protein binding sites. In contrast,

PDCA completely displaced pyruvate from PHD1, as indicated by the $R_{1\rho}$ relaxation rate returning to values comparable to free pyruvate. However, the overall signal intensity did not fully recover to the level of the free pyruvate sample. This reduction in intensity likely reflects polarization losses during the competition experiment rather than the effects of binding itself. Such losses could arise from small variations in dissolution efficiency or radical stability between measurements. Overall, these results demonstrate that the relaxation-based approach remains sensitive to binding even at 2 µM protein concentration and that competitive ligands can modulate the observed relaxation behavior. The experiments were repeated, and the resulting datasets are compared in the next section.

### 5.5.5. Repeatability of Binding at 2 µM PHD1 Concentration

To confirm the repeatability of the relaxation effects observed at 2 µM PHD1 and 14 µM pyruvate, the experiments were repeated under identical conditions. The resulting data are shown in Fig. 5.10.

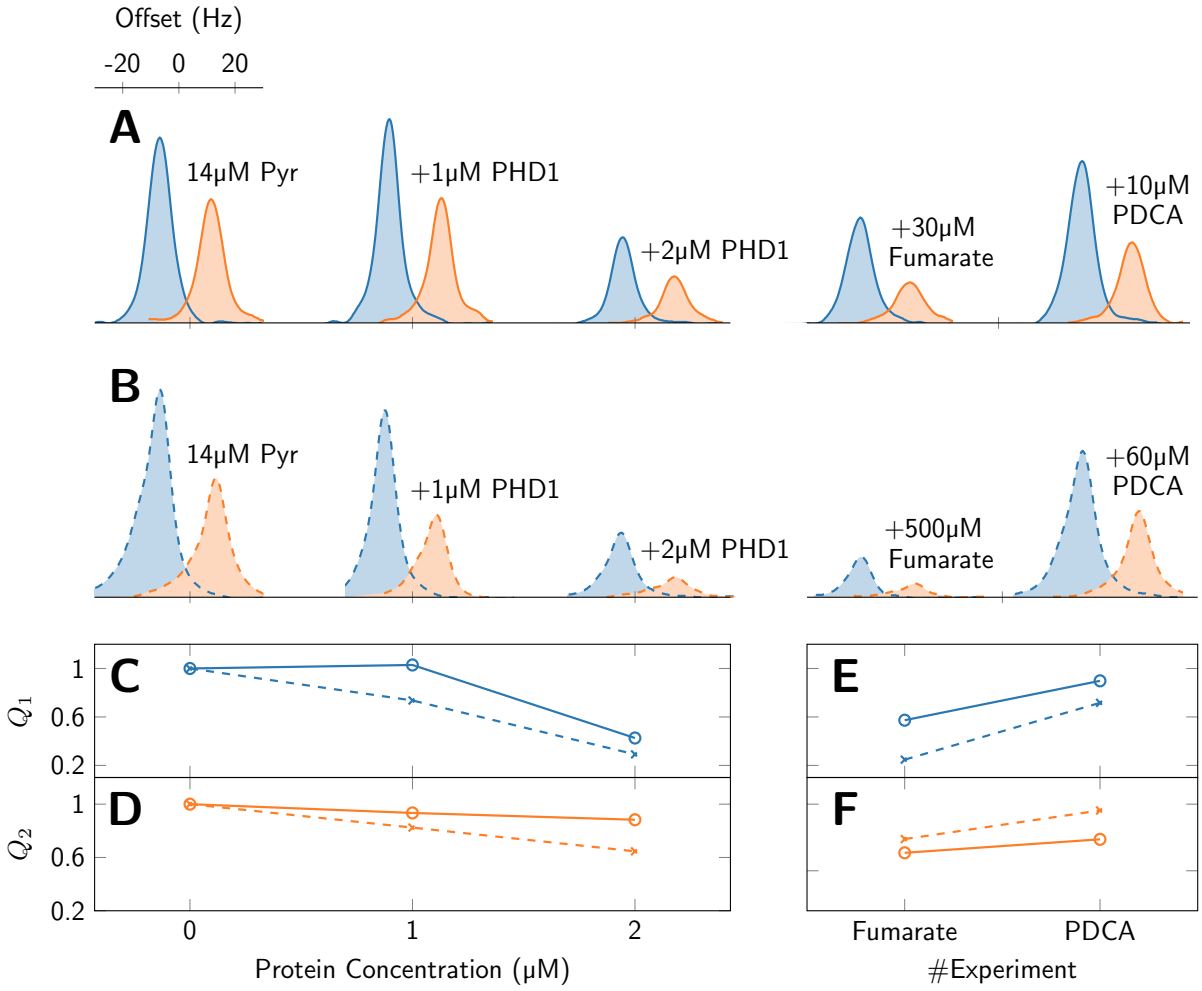


**Figure 5.10.:** Reproducibility of ligand-binding experiments at 2 µM PHD1. (A) First and second spectra acquired at increasing PHD1 concentrations. Protein concentrations are indicated below panel (D); for the competition experiments with PDCA, the protein concentration was kept constant at 2 µM. (B) Repetition of the experiment shown in (A) with higher PDCA (60 µM) and fumarate (500 µM) concentrations. Solid lines correspond to the data in (A), dashed lines to those in (B). (C) and (D) show the corresponding dimensionless binding scores $Q_1$ and $Q_2$, illustrating the relative longitudinal ($R_1$) and transverse ($R_{1\rho}$) relaxation effects. (E) and (F) depict the change in $Q_1$ and $Q_2$ upon fumarate and PDCA addition, indicated from the protein-bound to the competitor-bound state.

For experiments, the same sample preparation protocol, hyperpolarization parameters, and INEPT detection sequence were used to ensure consistency. In competition-binding experiments, higher concentrations of PDCA (60 µM) and fumarate (500 µM) were used to test whether competitive binding could also be detected in the $R_{1\rho}$ relaxation rate. The 1.5 µM dataset from the previous series was excluded.

Comparison of the datasets confirmed that negligible binding effects were observed at 1 µM PHD1, while pronounced binding effects were evident at 2 µM, as seen on the left sides of panels (A) and (B). The decrease in $Q_1$ and $Q_2$ values upon PHD1 addition indicated enhanced relaxation due to binding, as shown in panels (C) and (D). The competition experiments revealed a clear affinity-dependent response. PDCA effectively displaced pyruvate, as shown by the increase in $Q_2$ towards unity. This effect was more complete with 60 µM PDCA than with 10 µM. In contrast, fumarate showed only minimal displacement at 30 µM and partial recovery at the high concentration of 500 µM, consistent with its weak binding affinity. The fact that $Q_1$ and $Q_2$ values were not fully restored to unity in any competitor experiment suggested that a small population of pyruvate might have remained bound, or that the competitors themselves subtly influenced the relaxation environment.

Crucially, the qualitative behavior and the trends in $Q_1$ and $Q_2$ were consistent across both datasets. This repeatability robustly confirmed that the low-field $R_1$ and $R_{1\rho}$ relaxation metrics provided a reliable probe of binding, even at these low micromolar protein concentrations. To further interpret these effects, the same hyperpolarized intensities were used to calculate the corresponding longitudinal and transverse relaxation rates. This quantitative analysis provided direct insight into how binding modulated $R_1$ and $R_{1\rho}$, as described below.

#### 5.5.5.1. Determination of Relaxation Rates from Hyperpolarized Intensities

The observed signal intensities $I_1$ and $I_2$ were used to calculate the apparent longitudinal and transverse relaxation rates. Because the hyperpolarized system does not reach a steady state, each intensity directly reports the residual polarization after the corresponding relaxation interval. For the first acquisition, the detected intensity after a low-field evolution time $t_{\text{evol}}$ is given by:

$$I_1 = M_0 \, e^{-t_{\text{evol}}/T_1} \tag{5.13}$$

where $M_0$ is the initial magnetization immediately after dissolution and transfer. The longitudinal relaxation rate $R_1$ is then:

$$R_1 = \frac{1}{T_1} = -\frac{1}{t_{\text{evol}}} \ln\left(\frac{I_1}{M_0}\right) \tag{5.14}$$

Since $M_0$ cannot be measured directly, it was estimated using the signal intensity of the free ligand, for which $T_{1,\text{free}}$ is known from independent measurements. This estimation assumes that the initial hyperpolarization level $M_0$ is reproducible across all experiments:

$$M_0 = I_{1,\text{free}} \, e^{t_{\text{evol}}/T_{1,\text{free}}} \tag{5.15}$$

The second acquisition, recorded after $\Delta t = 300$ ms, reflects relaxation during the spin-lock period. After INEPT transfer, the first $\pi/4$ $^1$H readout pulse converts part of the hyperpolarized $^1$H magnetization into a detectable signal ($I_1$), while leaving the remaining magnetization along the $z$-axis. A subsequent $\pi/2$ $^1$H pulse flips this remaining magnetization for polarization transfer to $^{13}$C during the spin-lock. The intensity $I_2$ therefore follows:

$$I_2 = I_1 \, e^{-\Delta t/T_{1\rho}} \tag{5.16}$$

where $T_{1\rho}$ denotes the effective spin-lock relaxation time. The corresponding rate is:

$$R_{1\rho} = \frac{1}{T_{1\rho}} = -\frac{1}{\Delta t} \ln\left(\frac{I_2}{I_1}\right) \tag{5.17}$$

The extracted $R_1$ and $R_{1\rho}$ values thus provide two complementary relaxation observables, both of which are affected by protein binding. Experimental results from the previous section indicated that $R_1$ was more sensitive to binding-induced changes than $R_{1\rho}$ at low field, reflecting its dependence on both dipolar and paramagnetic relaxation pathways. The first two datasets : 14 µM pyruvate with varying PHD1 concentrations, shown in Fig. 5.9 and Fig. 5.10 (A), were used to extract the relaxation rates, which are summarized in Fig. 5.11. Note that the 1.5 µM experiment was missing from the third dataset Fig. 5.10 (B), so that dataset was excluded from this plot.

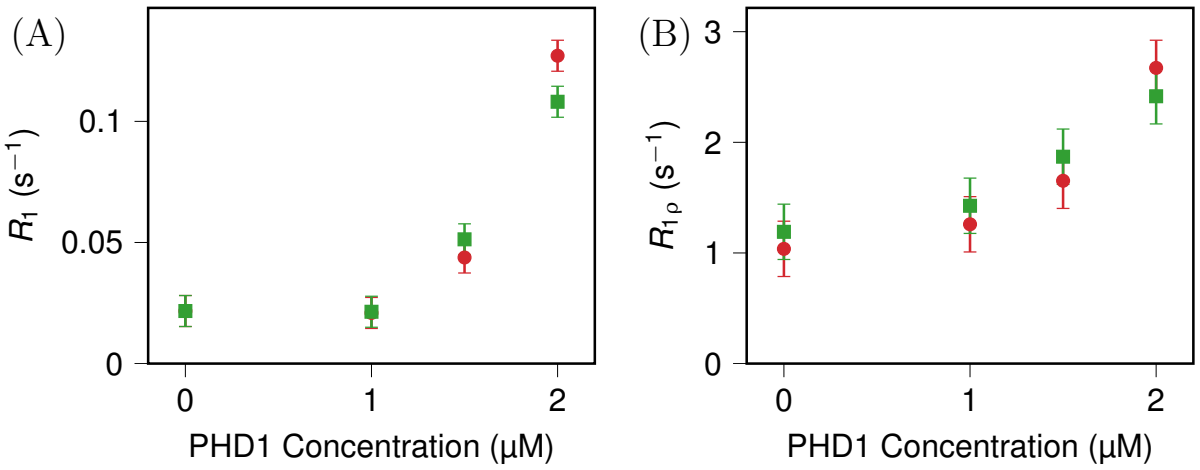


**Figure 5.11.:** Longitudinal ($R_1$) and spin-lock ($R_{1\rho}$) relaxation rates as a function of PHD1 concentration. The red circles represent the dataset from Fig. 5.9, and the green squares represent the dataset from Fig. 5.10A, with the error bars. The Python code for calculation is provided in Appendix A.13.

The corresponding calculated $T_1$ and $T_{1\rho}$ values are shown in Fig 5.12.

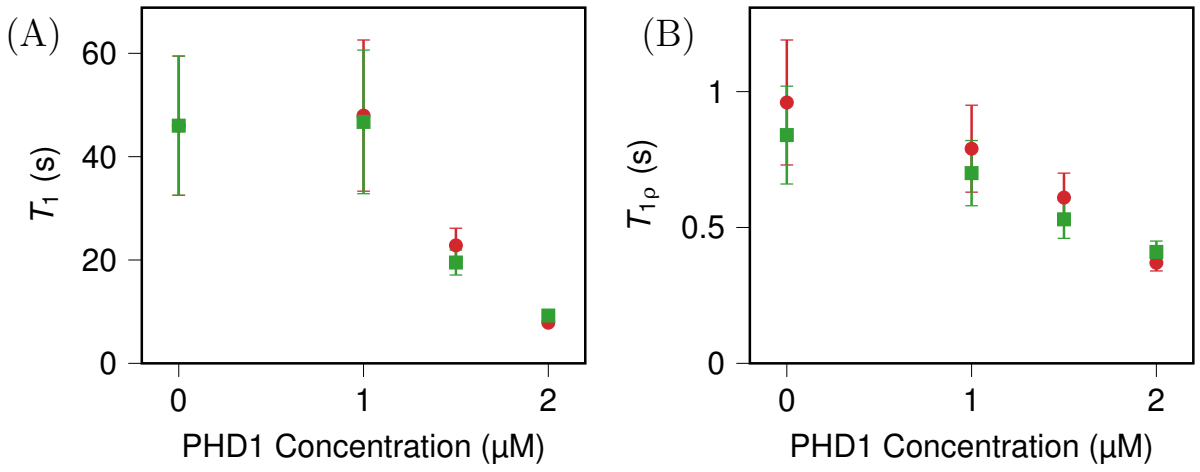


**Figure 5.12.:** $T_1$ and $T_{1\rho}$ relaxation time constant as a function of PHD1 concentration. The red circles represent the dataset from Fig. 5.9, and the green squares represent the dataset from Fig. 5.10A. Code is provided in Appendix A.13

As shown in Fig. 5.11 for two datsets, both longitudinal ($R_1$) and spin-lock ($R_{1\rho}$) relaxation rates increase with PHD1 concentration, demonstrating clear binding-induced relaxation enhancement. The $R_1$ rate exhibits particularly strong sensitivity, increasing approximately 5-fold from 0.022 $s^{-1}$ (free pyruvate) to 0.11-0.13 $s^{-1}$ at 2 µM PHD1. In comparison, $R_{1\rho}$ shows a more modest 2-3 fold increase over the same concentration range. In both sets of experiments, the addition of only 1 µM PHD1 protein did not produce a significant contrast in either $R_1$ or $R_{1\rho}$. The lack of contrast was attributed to adsorption of the protein on the ~ 1 m-long capillary used to deliver the buffer solution into the solvent reservoir. Although the two datasets differ slightly in absolute values, they consistently show the same concentration-dependent trends, confirming the robustness and reproducibility of the observed binding-induced relaxation effects.

The corresponding $T_1$ and $T_{1\rho}$ values shown in Fig 5.12, reveal the practical impact of these rate enhancements. $T_1$ decreases dramatically from ~46 s for free pyruvate to ~8-9 s at 2 µM PHD1, representing a 5-6 fold reduction in hyperpolarization signal. This substantial shortening directly affects the feasible signal detection time window in hyperpolarized experiments. Similarly, $T_{1\rho}$ decreases from ~0.8-1.0 s to ~0.4 s, indicating enhanced transverse relaxation.

Error bars in the calculated relaxation rates were estimated based on the experimental reproducibility established in Section 5.5.2. From repeated hyperpolarization experiments, the relative standard deviations of the measured signal intensities were $\sigma_{I_1} = 4.5\%$ for $I_1$ and $\sigma_{I_2} = 6\%$ for $I_2$. Assuming that both $I_1$ and $I_2$ are affected by the same level of uncertainties. The relative errors propagate through the logarithmic relationships in Equations 5.14 and 5.17 to yield absolute error bar in the relaxation rates:

$$\sigma(R_1) = \frac{\sqrt{2}\,\sigma_{I_1}}{t_{\text{evol}}}, \qquad \sigma(R_{1\rho}) = \frac{\sqrt{\sigma_{I_1}^2 + \sigma_{I_2}^2}}{\Delta t} \tag{5.18}$$

where $t_{evol}$ and $\Delta t$ is the evolution time used for $R_1$ and $R_{1\rho}$ determination. The resulting errors are absolute values with units of $s^{-1}$, as required for relaxation rates. To further isolate binding effects from experimental variability and provide dimensionless metrics, the rates were analyzed in terms of relative contrasts.

### 5.5.6. Quantification of Binding-Induced Relaxation Contrast

For binding assessments, the binding contrast $C_R$ has been defined in the literature [113] for the relaxation rates $R_1$ and $R_{1\rho}$. These contrast parameters serve as direct indicators of binding, independent of the absolute polarization level. The relaxation rates obtained for each protein concentration were compared to those of the free ligand. The relative changes can be expressed in terms of relaxation contrasts:

$$C_{R_1} = \frac{R_1 - R_1^{(0)}}{R_1^{(0)}}, \qquad C_{R_{1\rho}} = \frac{R_{1\rho} - R_{1\rho}^{(0)}}{R_{1\rho}^{(0)}}, \tag{5.19}$$

where $R_1^{(0)}$ and $R_{1\rho}^{(0)}$ correspond to the rates for the free ligand, and $R_1$ and $R_{1\rho}$ represent the rates in the presence of protein or competitor. The calculated contrast values $C_{R_1}$ and $C_{R_{1\rho}}$, derived from the $R_1$ and $R_{1\rho}$ values in Fig. 5.11, are presented in Fig. 5.13. Positive contrast values indicate enhanced relaxation due to binding-induced molecular motion restriction or paramagnetic effects.

Figure 5.13 shows the binding-induced relaxation contrasts $C_{R_1}$ (panel A) and $C_{R_{1\rho}}$ (panel B) as a function of PHD1 concentration. Both contrasts are negligible at 0-1 µM, indicating minimal binding,

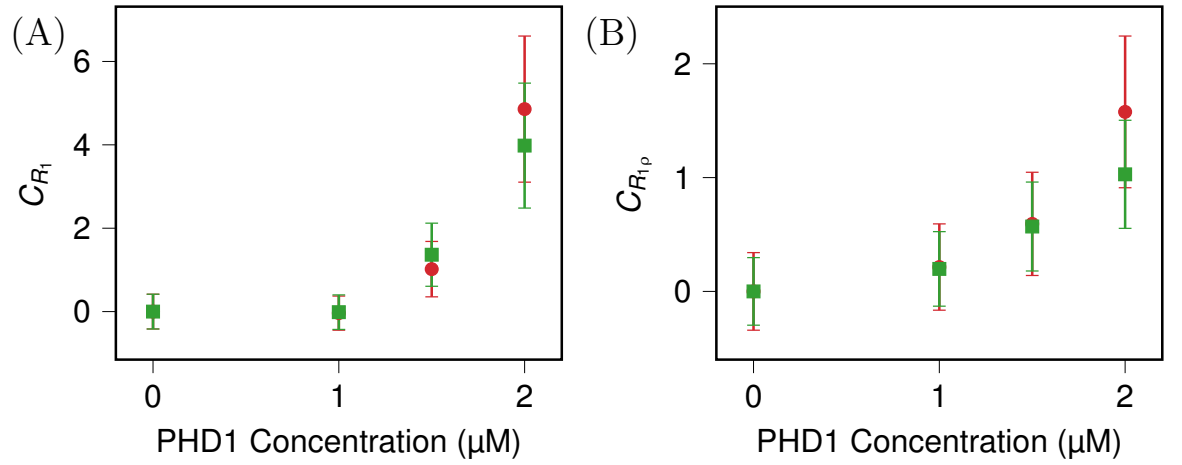


**Figure 5.13.:** Binding-induced relaxation contrasts $C_{R_1}$ (panel A) and $C_{R_{1\rho}}$ (panel B) as a function of PHD1 concentration. Red circles represent the dataset from Fig. 5.9, and green squares represent the dataset from Fig. 5.10A. The Python code for the calculations is provided in Appendix A.14.

and increase sharply at 1.5-2 μM, reflecting enhanced relaxation due to binding. $C_{R_1}$ rises more steeply than $C_{R_{1\rho}}$, suggesting a stronger impact on $R_1$ relaxation rate. Dataset 2 (green) reaches slightly higher contrast values than dataset 1 (red) at 2 μM, consistent with stronger or more efficient binding. The small error bars demonstrate that these trends are statistically significant.

The error bars on the relaxation contrasts were obtained by standard error propagation, accounting for the uncertainties in both the measured rate and the reference free-ligand rate. The uncertainties $\sigma(R_1^{(0)})$ and $\sigma(R_{1\rho}^{(0)})$ were estimated for the free ligand using Equation 5.18. The resulting errors in the contrast parameters are given by:

$$\sigma(C_{R_1}) = \sqrt{\left(\frac{\sigma(R_1)}{R_1^{(0)}}\right)^2 + \left(\frac{R_1\,\sigma(R_1^{(0)})}{(R_1^{(0)})^2}\right)^2}, \qquad \sigma(C_{R_{1\rho}}) = \sqrt{\left(\frac{\sigma(R_{1\rho})}{R_{1\rho}^{(0)}}\right)^2 + \left(\frac{R_{1\rho}\,\sigma(R_{1\rho}^{(0)})}{(R_{1\rho}^{(0)})^2}\right)^2} \tag{5.20}$$

## 5.6. Conclusion

This chapter demonstrated how low-field $R_1$ relaxation, combined with $^{13}$C hyperpolarization and $^{13}$C-$^{1}$H INEPT transfer, can serve as a sensitive and efficient method to probe ligand-protein interactions while reducing the required protein concentration to values as low as 2 μM. This represents a substantial improvement over conventional high-field ligand-observed NMR approaches, which typically require 10-100 μM protein concentrations. High-field NMR experiments typically rely on $R_{1\rho}$-based contrast. However, the findings presented here show that $R_1$-based contrast surpasses $R_{1\rho}$ contrast at low magnetic fields. This effect is inherently limited to low-field conditions, as $R_1$-based contrast primarily operates within this regime. Contrary to expectations, the $R_{1\rho}$-based contrast performed poorly in this study, with significant signal loss observed even in the absence of protein.

Binding-induced relaxation enhancements became apparent at protein concentrations of 1.5-2 μM. On the other hand, addition of 1 μM PHD1 protein did not produce a significant contrast in either $R_1$ or $R_{1\rho}$, likely due to adsorption on the ~ 1 m-long capillary used to deliver the buffer solution. A major experimental limitation arises from considerable variation in signal intensity observed between

independent experiments. This strict requirement for high repeatability can be significantly relaxed if an appropriate low-field $T_1$ measurement is performed, allowing $R_1$ itself to serve as the basis for contrast calculation[114].

Future developments will focus on integrating benchtop low-field $T_1$ measurements with hyperpolarized detection and advanced detection schemes such as microfluidic or cryogenic probes to enhance reproducibility and throughput. Together, these strategies open a path toward routine, low-cost screening of weak or transient protein-ligand interactions under near-physiological conditions. Overall, this work establishes low-field $R_1$ relaxometry as a versatile and scalable tool for studying biomolecular systems with minimal sample requirements.

# 6. Summary

In summary, this thesis demonstrates that bullet dissolution dynamic nuclear polarization (bullet-DNP) effectively addresses the fundamental sensitivity limitations of conventional NMR spectroscopy. Unlike conventional dissolution-DNP, bullet-DNP enables rapid sample transfer with minimal dilution, thereby preserving polarization during the transition from cryogenic to liquid states, as discussed in Chapter 2. A particular advantage is its compatibility with sensitive biological samples like proteins, as it eliminates the need for hot solvents. To enhance polarization efficiency and detection sensitivity, several methodological optimizations were implemented.

The development of optimized sample preparation formulations that promote efficient spin diffusion was crucial for achieving high polarization levels. Detection sensitivity was further improved through implementation of a $^{13}C \rightarrow ^{1}H$ reverse-INEPT polarization transfer coupled with a high-sensitivity $^{1}H$-detection probe. The combination of these advancements enabled the detection of 2-$^{13}$C-pyruvate at concentrations as low as 250 nM, corresponding to just 20 ng of material. This represents an approximately 4-fold enhancement in signal-to-noise ratio compared to direct $^{13}C$ detection and establishes new frontiers for NMR studies of mass-limited samples. Further, this approach was applied to experiments with a 1-minute delay, yielding a signal-to-noise ratio of 58 for 32 µM 2-$^{13}$C-pyruvate, demonstrating its potential for *in vivo* applications where such delays are operationally relevant.

Expanding upon the developed high-sensitivity framework, this work applied bullet-DNP to investigate protein-ligand interactions under physiologically relevant conditions. A novel low-field relaxation strategy was introduced, which exploits the high sensitivity of longitudinal relaxation rates ($R_1$) at low fields. Employing the human PHD1 protein as a model, binding was observed at concentrations down to 2 µM, representing a 10-fold decrease in protein requirement relative to standard NMR experiments. Quantitative analysis demonstrated that $R_1$-based measurements provided approximately 5-fold enhancement in binding contrast, whereas $R_{1\rho}$ yielded only a 2-3 fold increase. These findings establish $R_1$ relaxometry as a more sensitive approach for probing low-field ligand-binding. Competition binding experiments further show binding of the competitors, while the methodology's robustness was confirmed through repeatable results across multiple datasets. Overall, this work establishes bullet-DNP as a powerful and versatile tool for studying biomolecular systems with minimal sample requirements. The developed methods apply broadly to the systems containing long-lived spin polarization $^{13}C$ nuclei, such as carbonyl carbons, enabling studies of metabolic processes and protein-ligand interactions.

While this work demonstrates significant advancements, several limitations present opportunities for future improvement. A key challenge lies in the repeatability of the final detected hyperpolarized signal. The signal intensity depends on the entire process chain, from the initial polarization build-up in the solid state to the transfer and dissolution efficiency, and is susceptible to variability. Factors such as sample positioning, liquid helium flow dynamics during transfer, can all influence the efficiency of these steps, leading to the experimental variations observed in this work. Although the system operates under automated control, minor variations in these parameters between experiments contribute to the observed variability in liquid-state polarization. Additional polarization losses can occur during sample

transfer and dissolution, potentially arising from variations in radical concentration during dissolution or incomplete mixing. These effects are reflected in the repeated experiments for ligand-binding at 2 μM in Chapter 4, and contribute to the error bars in the measured relaxation rates. Future technical refinements addressing these operational variabilities could further improve the method's precision and repeatability.

Future developments could address these limitations through several promising approaches. First, the integration of bullet-DNP with benchtop low-field relaxometry would enable direct $T_1$ measurements within single experiments, eliminating dependence on polarization of reference samples like free pyruvate in ligand-binding. These low-field experiments can improve repeatability. Another approach, using a dilution-free detection scheme under development in our laboratory, would preserve polarization by avoiding dilution entirely, maintaining the same concentration of radicals, and reducing transfer losses. The integration of microfluidic handling systems could further enhance mixing during dissolution. For detection, cryogenic probes would boost concentration sensitivity, while stripline or detection probes would enhance mass sensitivity; both approaches could significantly improve the overall sensitivity of the bullet-DNP. A key direction for future work is the development of a fully automated bullet-DNP system, which is currently underway in our laboratory. Automation would enhance the method's robustness by standardizing sample handling and results in higher-throughput data acquisition.

The methodologies established in this thesis have significant implications beyond the specific model system studied. By drastically reducing sample requirements, this work makes NMR-based drug discovery accessible for targets that are difficult to express or purify, such as membrane proteins. Furthermore, the ability to perform sensitive, low-concentration binding studies under near-physiological conditions provides a more relevant framework for understanding biomolecular interactions. The detection sensitivity achieved also opens new avenues for following metabolic pathways in minimal cell cultures or tissue extracts, bridging the gap between *in vitro* biochemistry and *in vivo* imaging.

# Acronyms

| | |
|---|---|
| **ADC** | Analog-to-Digital Converter |
| **AKG** | $\alpha$-Ketoglutarate |
| **BBO** | Broadband Observe |
| **CE** | Cross-Effect |
| **CIDNP** | Chemically Induced Dynamic Nuclear Polarization |
| **CP** | Cross Polarization |
| **CPMG** | Carr–Purcell–Meiboom–Gill |
| **D-DNP** | Dissolution Dynamic Nuclear Polarization |
| **DFT** | Discrete Fourier Transform |
| **DMSO** | Dimethyl Sulfoxide |
| **DNP** | Dynamic Nuclear Polarization |
| **DTT** | Dithiothreitol |
| **EPR** | Electron Paramagnetic Resonance |
| **ETH** | Eidgenössische Technische Hochschule Zürich |
| **FID** | Free Induction Decay |
| **GE** | General Electric |
| **HIF** | Hypoxia-Inducible Factor |
| **IBG** | Institute of Biological Interfaces |
| **INEPT** | Insensitive Nuclei Enhanced by Polarization Transfer |
| **KG** | Ketoglutarate |
| **LB** | Luria–Bertani (broth) |
| **LOGSY** | Ligand-Observed via Gradient SpectroscopY |
| **MAS** | Magic Angle Spinning |
| **MRI** | Magnetic Resonance Imaging |
| **MR** | Magnetic Resonance |
| **NMR** | Nuclear Magnetic Resonance |
| **NOE** | Nuclear Overhauser Effect |

**NOG** N-oxalylglycine

**NTA** Nitrilotriacetic Acid

**OE** Overhauser Effect

**OD** Optical Density

**PDCA** 2,4-Pyridinedicarboxylic Acid

**PHD1** Prolyl Hydroxylase Domain 1

**PHIP** Parahydrogen-Induced Polarization

**PRE** Paramagnetic Relaxation Enhancement

**PTFE** Polytetrafluoroethylene (Teflon)

**RF** Radiofrequency

**SABRE** Signal Amplification by Reversible Exchange

**SE** Solid Effect

**SNR** Signal-to-Noise Ratio

**STD** Saturation Transfer Difference

**TBI** Triple-resonance Broadband Inverse

**TCI** Tokyo Chemical Industry

**TEMPO** (2,2,6,6-Tetramethylpiperidin-1-yl)oxyl

**TEMPOL** 4-Hydroxy-TEMPO

**TM** Thermal Mixing

**UV** Ultraviolet

# List of Figures

# List of Tables

# Bibliography


(1) Ardenkjær-Larsen, J. H.; Fridlund, B.; Gram, A.; Hansson, G.; Hansson, L.; Lerche, M. H.; Servin, R.; Thaning, M.; Golman, K. Increase in signal-to-noise ratio of >10,000 times in liquid-state NMR. *Proceedings of the National Academy of Sciences* **2003**, *100*, 10158–10163.

(2) Kouřil, K.; Kouřilová, H.; Bartram, S.; Levitt, M. H.; Meier, B. Scalable dissolution-dynamic nuclear polarization with rapid transfer of a polarized solid. *Nature Communications* **2019**, *10*, 1733.

(3) Kouřil, K.; Gramberg, M.; Jurkutat, M.; Kouřilová, H.; Meier, B. A cryogen-free, semi-automated apparatus for bullet-dynamic nuclear polarization with improved resolution. *Magnetic Resonance Discussions* **2021**, *2021*, 1–16.

(4) Levitt, M. H., *Spin Dynamics: Basics of Nuclear Magnetic Resonance*, 1st ed.; Wiley: Chichester ; New York, 2001; 672 pp.

(5) Keeler, J., *Understanding NMR Spectroscopy, Second Edition*, 1st ed.; Wiley: 2010; 528 pp.

(6) Bloch, F. Nuclear induction. *Physical review* **1946**, *70*, 460.

(7) Slichter, C. P. The discovery and demonstration of dynamic nuclear polarization—a personal and historical account. *Physical Chemistry Chemical Physics* **2010**, *12*, 5741–5751.

(8) Slichter, C. P., *Principles of magnetic resonance*; Springer Science & Business Media: 2013; Vol. 1.

(9) Hoult, D. I.; Richards, R. E. The Signal-to-Noise Ratio of the Nuclear Magnetic Resonance Experiment. *Journal of Magnetic Resonance (1969)* **1976**, *24*, 71–85.

(10) Ernst, R. R.; Bodenhausen, G.; Wokaun, A., *Principles of Nuclear Magnetic Resonance in One and Two Dimensions*; Oxford University Press: Oxford, 1990; 640 pp.

(11) Doty, F.; Connick, T.; Ni, X.; Clingan, M. Noise in high-power, high-frequency double-tuned probes. *Journal of Magnetic Resonance (1969)* **1988**, *77*, 536–549.

(12) Nyquist, H. Thermal agitation of electric charge in conductors. *Physical review* **1928**, *32*, 110.

(13) Kovacs, H.; Moskau, D.; Spraul, M. Cryogenically cooled probes—a leap in NMR technology. *Progress in Nuclear Magnetic Resonance Spectroscopy* **2005**, *46*, 131–155.

(14) Bloembergen, N.; Purcell, E. M.; Pound, R. V. Relaxation Effects in Nuclear Magnetic Resonance Absorption. *Physical Review* **1948**, *73*, 679–712.

(15) Solomon, I. Relaxation processes in a system of two spins. *Physical Review* **1955**, *99*, 559–565.

(16) Bydder, G. M.; Young, I. R. MR imaging: clinical use of the inversion recovery sequence. *Journal of Computer Assisted Tomography* **1985**, *9*, 659–675.

(17) Bydder, G. M.; Young, I. R. Clinical use of the partial saturation and saturation recovery sequences in MR imaging. *Journal of Computer Assisted Tomography* **1985**, *9*, 1020–1032.

(18) Meiboom, S.; Gill, D. Modified spin-echo method for measuring nuclear relaxation times. *Review of Scientific Instruments* **1958**, *29*, 688–691.

(19) Lowe, I. J. Free induction decays of rotating solids. *Physical Review Letters* **1959**, *2*, 285–287.

(20) Buratto, R.; Bornet, A.; Milani, J.; Mammoli, D.; Vuichoud, B.; Salvi, N.; Singh, M.; Laguerre, A.; Passemard, S.; Gerber-Lemaire, S., et al. Drug screening boosted by hyperpolarized long-lived states in NMR. *ChemMedChem* **2014**, *9*, 2509–2515.

(21) Min, H.; Sekar, G.; Hilty, C. Polarization transfer from ligands hyperpolarized by dissolution dynamic nuclear polarization for screening in drug discovery. *ChemMedChem* **2015**, *10*, 1559–1563.

(22) Stern, Q.; Milani, J.; Vuichoud, B.; Bornet, A.; Gossert, A. D.; Bodenhausen, G.; Jannin, S. Hyperpolarized water to study protein–ligand interactions. *The Journal of Physical Chemistry Letters* **2015**, *6*, 1674–1678.

(23) Gallagher, F. A.; Kettunen, M. I.; Brindle, K. M. Biomedical Applications of Hyperpolarized $^{13}$C Magnetic Resonance Imaging. *Progress in Nuclear Magnetic Resonance Spectroscopy* **2009**, *55*, 285–295.

(24) Nelson, S. J.; Kurhanewicz, J.; Vigneron, D. B.; Larson, P. E. Z.; Harzstark, A. L.; Ferrone, M.; Van Criekinge, M.; Chang, J. W.; Bok, R.; Park, I., et al. Metabolic Imaging of Patients with Prostate Cancer Using Hyperpolarized [1-$^{13}$C]Pyruvate. *Science Translational Medicine* **2013**, *5*, 198ra108.

(25) Golman, K.; in't Zandt, R.; Lerche, M.; Pehrson, R.; Ardenkjaer-Larsen, J. H. Metabolic Imaging by Hyperpolarized $^{13}$C Magnetic Resonance Imaging for In Vivo Tumor Diagnosis. *Cancer Research* **2006**, *66*, 10855–10860.

(26) Kovtunov, K. V.; Beck, I. E.; Bukhtiyarov, V. I.; Koptyug, I. V. Observation of parahydrogen-induced polarization in heterogeneous hydrogenation on supported metal catalysts. *Angewandte Chemie International Edition* **2008**, *47*, 1492–1495.

(27) Lesage, A.; Lelli, M.; Gajan, D.; Caporini, M. A.; Vitzthum, V.; Miéville, P.; Alauzun, J.; Roussey, A.; Thieuleux, C.; Mehdi, A., et al. Surface enhanced NMR spectroscopy by dynamic nuclear polarization. *Journal of the American Chemical Society* **2010**, *132*, 15459–15461.

(28) Rossini, A. J.; Zagdoun, A.; Lelli, M.; Lesage, A.; Copéret, C.; Emsley, L. Dynamic Nuclear Polarization Surface Enhanced NMR Spectroscopy. *Accounts of Chemical Research* **2013**, *46*, 1942–1951.

(29) Bowen, S.; Hilty, C. Temporal Chemical Shift Correlations in Reactions Studied by Hyperpolarized Nuclear Magnetic Resonance. *Analytical Chemistry* **2009**, *81*, 4543–4547.

(30) Zeng, H.; Lee, Y.; Hilty, C. Quantitative rate determination by dynamic nuclear polarization enhanced NMR of a Diels- Alder reaction. *Analytical chemistry* **2010**, *82*, 8897–8902.

(31) Lee, Y.; Heo, G. S.; Zeng, H.; Wooley, K. L.; Hilty, C. Detection of Living Anionic Species in Polymerization Reactions Using Hyperpolarized NMR. *Journal of the American Chemical Society* **2013**, *135*, 4636–4639.

(32) Eills, J.; Budker, D.; Cavagnero, S.; Chekmenev, E. Y.; Elliott, S. J.; Jannin, S.; Lesage, A.; Matysik, J.; Meersmann, T.; Prisner, T., et al. Spin Hyperpolarization in Modern Magnetic Resonance. *Chemical Reviews* **2023**, *123*, 1417–1551.

(33) Hirsch, M. L.; Kalechofsky, N.; Belzer, A.; Rosay, M.; Kempf, J. G. Brute-force hyperpolarization for NMR and MRI. *Journal of the American Chemical Society* **2015**, *137*, 8428–8434.

(34) Silvera, I. F. The solid molecular hydrogens in the condensed phase: Fundamentals and static properties. *Reviews of Modern Physics* **1980**, *52*, 393–452.

(35) Kovtunov, K. V.; Zhivonitko, V. V.; Skovpin, I. V.; Salnikov, O. G.; Koptyug, I. V., Catalytic enhancement of NMR sensitivity for advanced spectroscopic and imaging studies in catalysis and life sciences In *Magnetic Nanomaterials: Applications in Catalysis and Life Sciences*, Bossmann, S. H., Wang, H., Eds.; Royal Society of Chemistry: 2017, pp 142–171.

(36) Nikolaou, P.; Goodson, B. M.; Chekmenev, E. Y. NMR hyperpolarization techniques for biomedicine. *Chemistry–A European Journal* **2015**, *21*, 3156–3166.

(37) Tickner, B. J.; Zhivonitko, V. V. Advancing homogeneous catalysis for parahydrogen-derived hyperpolarisation and its NMR applications. *Chemical Science* **2022**, *13*, 4670–4696.

(38) Bhattacharya, P.; Chekmenev, E. Y.; Reynolds, W. F.; Wagner, S.; Zacharias, N.; Chan, H. R.; Bünger, R.; Ross, B. D. Parahydrogen-induced polarization (PHIP) hyperpolarized MR receptor imaging in vivo: a pilot study of $^{13}$C imaging of atheroma in mice. *NMR in Biomedicine* **2011**, *24*, 1023–1028.

(39) Fraser, R.; Rutjes, F. P.; Feiters, M. C.; Tessari, M. Analysis of complex mixtures by chemosensing NMR using para-hydrogen-induced hyperpolarization. *Accounts of Chemical Research* **2022**, *55*, 1832–1844.

(40) Bordonali, L.; Nordin, N.; Fuhrer, E.; MacKinnon, N.; Korvink, J. G. Parahydrogen based NMR hyperpolarisation goes micro: an alveolus for small molecule chemosensing. *Lab on a Chip* **2019**, *19*, 503–512.

(41) Robertson, T. B. R.; Mewis, R. E., Perspective on the hyperpolarisation technique signal amplification by reversible exchange (SABRE) in NMR spectroscopy and MR imaging In *Annual Reports on NMR Spectroscopy*; Elsevier: 2018; Vol. 93, pp 145–212.

(42) Adams, R. W.; Aguilar, J. A.; Atkinson, K. D.; Cowley, M. J.; Elliott, P. I. P.; Duckett, S. B.; Green, G. G. R.; Khazal, I. G.; López-Serrano, J.; Williamson, D. C. Reversible interactions with para-hydrogen enhance NMR sensitivity by polarization transfer. *Science* **2009**, *323*, 1708–1711.

(43) Rayner, P. J.; Duckett, S. B. Signal amplification by reversible exchange (SABRE): From discovery to diagnosis. *Angewandte Chemie International Edition* **2018**, *57*, 6742–6753.

(44) Cowley, M. J.; Adams, R. W.; Atkinson, K. D.; Cockett, M. C. R.; Duckett, S. B.; Green, G. G. R.; Lohman, J. A. B.; Kerssebaum, R.; Kilgour, D.; Mewis, R. E. Iridium N-heterocyclic carbene complexes as efficient catalysts for magnetization transfer from para-hydrogen. *Journal of the American Chemical Society* **2011**, *133*, 6134–6137.

(45) Zeng, H.; Xu, J.; Gillen, J.; McMahon, M. T.; Artemov, D.; Tyburn, J.-M.; Lohman, J. A. B.; Mewis, R. E.; Atkinson, K. D.; Green, G. G. R., et al. Optimization of SABRE for polarization of the tuberculosis drugs pyrazinamide and isoniazid. *Journal of Magnetic Resonance* **2013**, *237*, 73–78.

(46) Skovpin, I. V.; Svyatova, A.; Chukanov, N.; Chekmenev, E. Y.; Kovtunov, K. V.; Koptyug, I. V. $^{15}$N hyperpolarization of dalfampridine at natural abundance for magnetic resonance imaging. *Chemistry – A European Journal* **2019**, *25*, 12694–12697.

(47) Chukanov, N. V.; Salnikov, O. G.; Trofimov, I. A.; Kabir, M. S. H.; Kovtunov, K. V.; Koptyug, I. V.; Chekmenev, E. Y. Synthesis and $^{15}$N NMR Signal Amplification by Reversible Exchange of [$^{15}$N] Dalfampridine at Microtesla Magnetic Fields. *ChemPhysChem* **2021**, *22*, 960–967.

(48) Bargon, J.; Fischer, H.; Johnsen, U. Kernresonanz-emissionslinien während rascher radikalreaktionen: I. Aufnahmeverfahren und beispiele. *Zeitschrift für Naturforschung A* **1967**, *22*, 1551–1555.

(49) Ward, H. R.; Lawler, R. G. Nuclear magnetic resonance emission and enhanced absorption in rapid organometallic reactions. *Journal of the American Chemical Society* **1967**, *89*, 5518–5519.

(50) Torres, F.; Sobol, A.; Greenwald, J.; Renn, A.; Morozova, O.; Yurkovskaya, A.; Riek, R. Molecular features toward high photo-CIDNP hyperpolariztion explored through the oxidocyclization of tryptophan. *Physical Chemistry Chemical Physics* **2021**, *23*, 6641–6650.

(51) Hore, J.; Broadhurst, R. Photo-CIDNP of biopolymers. *Progress in nuclear magnetic resonance spectroscopy* **1993**, *25*, 345–402.

(52) Wenckebach, W. T., *Essentials of Dynamic Nuclear Polarization*; Spindrift Publications: The Netherlands, 2016.

(53) Wind, R. A.; Duijvestijn, M. J.; Van Der Lugt, C.; Manenschijn, A.; Vriend, J. Applications of dynamic nuclear polarization in $^{13}$C NMR in solids. *Progress in Nuclear Magnetic Resonance Spectroscopy* **1985**, *17*, 33–67.

(54) Lock, H.; Maciel, G. E.; Johnson, C. E. Natural-abundance $^{13}$C dynamic nuclear polarization experiments on chemical vapor deposited diamond film. *Journal of Materials Research* **1992**, *7*, 2791–2797.

(55) Hall, D. A.; Maus, D. C.; Gerfen, G. J.; Inati, S. J.; Becerra, L. R.; Dahlquist, F. W.; Griffin, R. G. Polarization-enhanced NMR spectroscopy of biomolecules in frozen solution. *Science* **1997**, *276*, 930–932.

(56) Maryasov, A. G.; Bowman, M. K. Comment on "Modeling of motional EPR spectra using hindered Brownian rotational diffusion and the stochastic Liouville equation" [J. Chem. Phys. 152, 094103 (2020)]. *The Journal of Chemical Physics* **2020**, *153*, 027101.

(57) Mohr, P. J.; Taylor, B. N.; Newell, D. B. CODATA Recommended Values of the Fundamental Physical Constants: 2006. *Journal of Physical and Chemical Reference Data* **2008**, *37*, 1187–1284.

(58) Abragam, A.; Bleaney, B., *Electron Paramagnetic Resonance of Transition Ions*; Oxford University Press: Oxford, 2012.

(59) Capozzi, A.; Patel, S.; Gunnarsson, C. P.; Marco-Rius, I.; Comment, A.; Karlsson, M.; Lerche, M. H.; Ouari, O.; Ardenkjær-Larsen, J. H. Efficient hyperpolarization of U-13C-glucose using narrow-line UV-generated labile free radicals. *Angewandte Chemie International Edition* **2019**, *58*, 1334–1339.

(60) Kurdzesau, F.; Van Den Brandt, B.; Comment, A.; Hautle, P.; Jannin, S.; Van Der Klink, J. J.; Konter, J. A. Dynamic nuclear polarization of small labelled molecules in frozen water–alcohol solutions. *Journal of Physics D: Applied Physics* **2008**, *41*, 155506.

(61) Lumata, L.; Kovacs, Z.; Sherry, A. D.; Malloy, C.; Hill, S.; Van Tol, J.; Yu, L.; Song, L.; Merritt, M. E. Electron spin resonance studies of trityl OX063 at a concentration optimal for DNP. *Physical Chemistry Chemical Physics* **2013**, *15*, 9800–9807.

(62) Overhauser, A. W. Polarization of nuclei in metals. *Physical Review* **1953**, *92*, 411.

(63) Wenckebach, W. T. Electron spin–spin interactions in DNP: Thermal mixing vs. the cross effect. *Applied Magnetic Resonance* **2021**, *52*, 731–748.

(64) Mentink-Vigier, F.; Mathies, G.; Liu, Y.; Barra, A.-L.; Caporini, M. A.; Lee, D.; Hediger, S.; Griffin, R. G.; De Paëpe, G. Efficient cross-effect dynamic nuclear polarization without depolarization in high-resolution MAS NMR. *Chemical Science* **2017**, *8*, 8150–8163.

(65) Ardenkjær-Larsen, J. H. On the present and future of dissolution-DNP. *Journal of Magnetic Resonance* **2016**, *264*, 3–12.

(66) Comment, A. Dissolution DNP for in vivo preclinical studies. *Journal of Magnetic Resonance* **2016**, *264*, 39–48.

(67) Kim, Y.; Hilty, C., Applications of dissolution-DNP for NMR screening In *Methods in enzymology*; Elsevier: 2019; Vol. 615, pp 501–526.

(68) Yang, H.; Li, S.; Mickles, C. A.; Guzman-Luna, V.; Sugisaki, K.; Thompson, C. M.; Dang, H. H.; Cavagnero, S. Selective Isotope Labeling and LC-Photo-CIDNP Enable NMR Spectroscopy at Low-Nanomolar Concentration. *Journal of the American Chemical Society* **2022**, *144*, 11608–11619.

(69) Torres, F.; Bütikofer, M.; Stadler, G. R.; Renn, A.; Kadavath, H.; Bobrovs, R.; Jaudzems, K.; Riek, R. Ultrafast Fragment Screening Using Photo-Hyperpolarized (CIDNP) NMR. *Journal of the American Chemical Society* **2023**, *145*, 12066–12080.

(70) Bowers, C. R.; Weitekamp, D. P. Parahydrogen and Synthesis Allow Dramatically Enhanced Nuclear Alignment. *Journal of the American Chemical Society* **1987**, *109*, 5541–5542.

(71) Sellies, L.; Aspers, R. L. E. G.; Feiters, M. C.; Rutjes, F. P. J. T.; Tessari, M. Parahydrogen Hyperpolarization Allows Direct NMR Detection of $\alpha$-Amino Acids in Complex (Bio)mixtures. *Angewandte Chemie* **2021**, *133*, 27160–27165.

(72) Eills, J.; Hale, W.; Sharma, M.; Rossetto, M.; Levitt, M. H.; Utz, M. High-Resolution Nuclear Magnetic Resonance Spectroscopy with Picomole Sensitivity by Hyperpolarization on a Chip. *Journal of the American Chemical Society* **2019**, *141*, 9955–9963.

(73) Chen, H.-Y.; Ragavan, M.; Hilty, C. Protein folding studied by dissolution dynamic nuclear polarization. *Angewandte Chemie International Edition* **2013**, *52*, 9192–9195.

(74) Zhang, G.; Schilling, F.; Glaser, S. J.; Hilty, C. Reaction monitoring using hyperpolarized NMR with scaling of heteronuclear couplings by optimal tracking. *Journal of Magnetic Resonance* **2016**, *272*, 123–128.

(75) Olsen, G.; Markhasin, E.; Szekely, O.; Bretschneider, C.; Frydman, L. Optimizing water hyperpolarization and dissolution for sensitivity-enhanced 2D biomolecular NMR. *Journal of Magnetic Resonance* **2016**, *264*, 49–58.

(76) Narwal, P.; Lorz, N.; Minaei, M.; Jannin, S.; Kouřil, K.; Gossert, A.; Meier, B. Bullet-DNP Enables NMR Spectroscopy of Pyruvate and Amino Acids at Nanomolar to Low Micromolar Concentrations. *Analytical Chemistry* **2024**, *96*, 14734–14740.

(77) Harris, T.; Bretschneider, C.; Frydman, L. Dissolution DNP NMR with solvent mixtures: Substrate concentration and radical extraction. *Journal of Magnetic Resonance* **2011**, *211*, 96–100.

(78) Ardenkjær-Larsen, J. H.; Bowen, S.; Petersen, J. R.; Rybalko, O.; Vinding, M. S.; Ullisch, M.; Nielsen, N. C. Cryogen-free dissolution dynamic nuclear polarization polarizer operating at 3.35 T, 6.70 T, and 10.1 T. *Magnetic Resonance in Medicine* **2019**, *81*, 2184–2194.

(79) Ardenkjaer-Larsen, J.-H.; Boebinger, G. S.; Comment, A.; Duckett, S.; Edison, A. S.; Engelke, F.; Griesinger, C.; Griffin, R. G.; Hilty, C.; Maeda, H., et al. Facing and Overcoming Sensitivity Challenges in Biomolecular NMR Spectroscopy. *Angewandte Chemie International Edition* **2015**, *54*, 9162–9185.

(80) Harris, T.; Bretschneider, C.; Frydman, L. Dissolution DNP NMR with solvent mixtures: Substrate concentration and radical extraction. *Journal of Magnetic Resonance* **2011**, *211*, 96–100.

(81) Joo, C.-G.; Casey, A.; Turner, C. J.; Griffin, R. G. In Situ Temperature-Jump Dynamic Nuclear Polarization: Enhanced Sensitivity in Two Dimensional 13C-13C Correlation Spectroscopy in Solution. *Journal of the American Chemical Society* **2009**, *131*, 12–13.

(82) Sharma, M.; Janssen, G.; Leggett, J.; Kentgens, A.; van Bentum, P. Rapid-melt dynamic nuclear polarization. *Journal of Magnetic Resonance* **2015**, *258*, 40–48.

(83) Miéville, P.; Ahuja, P.; Sarkar, R.; Jannin, S.; Vasos, P. R.; Gerber-Lemaire, S.; Mishkovsky, M.; Comment, A.; Gruetter, R.; Ouari, O., et al. Scavenging free radicals to preserve enhancement and extend relaxation times in NMR using dynamic nuclear polarization. *Angewandte Chemie* **2010**, *122*, 6318–6321.

(84) Jacquinot, J. F.; Wenckebach, W. T.; Goldman, M.; Abragam, A. Polarization and NMR Observation of $Ca^{43}$ Nuclei in $CaF_2$. *Physical Review Letters* **1974**, *32*, 1096.

(85) Elliott, S. J.; Cousin, S. F.; Chappuis, Q.; Cala, O.; Ceillier, M.; Bornet, A.; Jannin, S. Dipolar order mediated $^{1}H \rightarrow {}^{13}C$ cross-polarization for dissolution-dynamic nuclear polarization. *Magnetic Resonance Discussions* **2020**, *2020*, 1–10.

(86) Bornet, A.; Melzi, R.; Perez Linde, A. J.; Hautle, P.; van Den Brandt, B.; Jannin, S.; Bodenhausen, G. Boosting dissolution dynamic nuclear polarization by cross polarization. *The Journal of Physical Chemistry Letters* **2013**, *4*, 111–114.

(87) Kouřilová, H.; Jurkutat, M.; Peat, D.; Kouřil, K.; Khan, A. S.; Horsewill, A. J.; MacDonald, J. F.; Owers-Bradley, J.; Meier, B. Radical-induced hetero-nuclear mixing and low-field $^{13}C$ relaxation in solid pyruvic acid. *Physical Chemistry Chemical Physics* **2022**, *24*, 28242–28249.

(88) Jurkutat, M.; Kouřilová, H.; Peat, D.; Kouřil, K.; Khan, A. S.; Horsewill, A. J.; MacDonald, J. F.; Owers-Bradley, J.; Meier, B. Radical-induced low-field $^{1}H$ relaxation in solid pyruvic acid doped with trityl-OX063. *The Journal of Physical Chemistry Letters* **2022**, *13*, 10370–10376.

(89) Asakura, T.; Ando, I., *Solid State NMR of Polymers*; Elsevier: 1998; Vol. 84.

(90) Dumez, J.-N.; Halse, M. E.; Butler, M. C.; Emsley, L. A first-principles description of proton-driven spin diffusion. *Physical Chemistry Chemical Physics* **2012**, *14*, 86–89.

(91) Wang, J.; Kreis, F.; Wright, A. J.; Hesketh, R. L.; Levitt, M. H.; Brindle, K. M. Dynamic $^{1}H$ imaging of hyperpolarized [1-$^{13}C$] lactate in vivo using a reverse INEPT experiment. *Magnetic Resonance in Medicine* **2018**, *79*, 741–747.

(92) Claridge, T. D. W., *High-resolution NMR Techniques in Organic Chemistry*; Elsevier: 2016; Vol. 27.

(93) Bengs, C.; Levitt, M. H. SpinDynamica: Symbolic and numerical magnetic resonance in a Mathematica environment. *Magnetic Resonance in Chemistry* **2018**, *56*, 374–414.

(94) Hoult, D. I.; Richards, R. E. The signal-to-noise ratio of the nuclear magnetic resonance experiment. *Journal of Magnetic Resonance (1969)* **1976**, *24*, 71–85.

(95) Badilita, V.; Meier, R. C. H.; Spengler, N.; Wallrabe, U.; Utz, M.; Korvink, J. G. Microscale nuclear magnetic resonance: a tool for soft matter research. *Soft Matter* **2012**, *8*, 10583–10597.

(96) Narwal, P.; Lorz, N.; Minaei, M.; Gossert, A. D.; Meier, B. Single-scan detection of ligand-binding using hyperpolarization and low-field relaxation. *Communications Chemistry* **2026**.

(97) Mayer, M.; Meyer, B. Characterization of ligand binding by saturation transfer difference NMR spectroscopy. *Angewandte Chemie International Edition* **1999**, *38*, 1784–1788.

(98) Dalvit, C.; Flocco, M.; Knapp, S.; Mostardini, M.; Perego, R.; Stockman, B. J.; Veronesi, M.; Varasi, M. High-Throughput NMR-Based Screening with Competition Binding Experiments. *Journal of the American Chemical Society* **2002**, *124*, 7702–7709.

(99) Dalvit, C.; Flocco, M.; Knapp, S.; Mostardini, M.; Perego, R.; Stockman, B. J.; Veronesi, M.; Varasi, M. High-throughput NMR-based screening with competition binding experiments. *Journal of the American Chemical Society* **2002**, *124*, 7702–7709.

(100) McKenzie, E. A.; Abbott, W. M. Expression of recombinant proteins in insect and mammalian cells. *Methods* **2018**, *147*, 40–49.

(101) Lorz, N.; Czarniecki, B.; Loss, S.; Meier, B.; Gossert, A. D. Higher Contrast in 1H-Observed NMR Ligand Screening with the PEARLScreen Experiment. *Angewandte Chemie International Edition* **2025**, *64*, e202423879.

(102) Lee, Y.; Zeng, H.; Ruedisser, S.; Gossert, A. D.; Hilty, C. Nuclear magnetic resonance of hyperpolarized fluorine for characterization of protein–ligand interactions. *Journal of the American Chemical Society* **2012**, *134*, 17448–17451.

(103) Lerche, M. H.; Meier, S.; Jensen, P. R.; Baumann, H.; Petersen, B. O.; Karlsson, M.; Duus, J. Ø.; Ardenkjær-Larsen, J. H. Study of molecular interactions with $^{13}$C DNP-NMR. *Journal of Magnetic Resonance* **2010**, *203*, 52–56.

(104) Pham, P.; Hilty, C. $R_2$ Relaxometry of SABRE-Hyperpolarized Substrates at a Low Magnetic Field. *Analytical Chemistry* **2023**, *95*, 16911–16917.

(105) Kowalewski, J.; Maler, L., *Nuclear Spin Relaxation in Liquids: Theory, Experiments, and Applications*, 1st; CRC Press: Boca Raton, 2006.

(106) Lipari, G.; Szabo, A. Model-free approach to the interpretation of nuclear magnetic resonance relaxation in macromolecules. 1. Theory and range of validity. *Journal of the American Chemical Society* **1982**, *104*, 4546–4559.

(107) Torchia, D. A.; Szabo, A. Spin-lattice relaxation in solids. *Journal of Magnetic Resonance (1969)* **1982**, *49*, 107–121.

(108) Flashman, E.; Bagg, E. A. L.; Chowdhury, R.; Mecinovic, J.; Loenarz, C.; McDonough, M. A.; Hewitson, K. S.; Schofield, C. J. Kinetic rationale for selectivity toward N- and C-terminal oxygen-dependent degradation domain substrates mediated by a loop region of hypoxia-inducible factor prolyl hydroxylases. *Journal of Biological Chemistry* **2008**, *283*, 3808–3815.

(109) Bertini, I.; Luchinat, C.; Parigi, G.; Pierattelli, R. Perspectives in paramagnetic NMR of metalloproteins. *Dalton Transactions* **2008**, 3782–3790.

(110) Leung, I. K. H.; Demetriades, M.; Hardy, A. P.; Lejeune, C.; Smart, T. J.; Szöllössi, A.; Kawamura, A.; Schofield, C. J.; Claridge, T. D. W. Reporter ligand NMR screening method for 2-oxoglutarate oxygenase inhibitors. *Journal of Medicinal Chemistry* **2013**, *56*, 547–555.

(111) Gurol, K. C.; Jursa, T.; Cho, E. J.; Fast, W.; Dalby, K. N.; Smith, D. R.; Mukhopadhyay, S. PHD2 enzyme is an intracellular manganese sensor that initiates the homeostatic response against elevated manganese. *Proceedings of the National Academy of Sciences* **2024**, *121*, e2402538121.

(112) Koivunen, P.; Hirsilä, M.; Remes, A. M.; Hassinen, I. E.; Kivirikko, K. I.; Myllyharju, J. Inhibition of Hypoxia-Inducible Factor (HIF) Hydroxylases by Citric Acid Cycle Intermediates: Possible Links between Cell Metabolism and Stabilization of HIF. *Journal of Biological Chemistry* **2007**, *282*, 4524–4532.

(113) Buratto, R.; Mammoli, D.; Chiarparin, E.; Williams, G.; Bodenhausen, G. Exploring Weak Ligand–Protein Interactions by Long-Lived NMR States: Improved Contrast in Fragment-Based Drug Screening. *Angewandte Chemie International Edition* **2014**, *53*, 11376–11380.

(114) Buratto, R.; Mammoli, D.; Canet, E.; Bodenhausen, G. Ligand–protein affinity studies using long-lived states of fluorine-19 nuclei. *Journal of Medicinal Chemistry* **2016**, *59*, 1960–1966.

(115) Brinkmann, A.; Levitt, M. H. Symmetry principles in the nuclear magnetic resonance of spinning solids: Heteronuclear recoupling by generalized Hartmann–Hahn sequences. *The Journal of Chemical Physics* **2001**, *115*, 357–384.

# A. Appendix

This appendix includes SpinDynamica code in Mathematica and Python scripts used to produce many figures in this thesis.

## A.1. Boltzmann Distribution

**Code A.1:** Thermal equilibrium polarization for the electron (blue), $^{1}$H (orange), and $^{13}$C (green) at a magnetic field of 6.7 T.

```
import numpy as np
import matplotlib.pyplot as plt
from spindata import gamma
from scipy.constants import hbar, k

B = 6.7
# calculate energy splitting
dE = gamma("1H")*B
print("{:.2f} MHz".format(dE/(2*np.pi*1e6)))

# Temperature range in Kelvin
T = np.linspace(1, 300, 500)  # from 1 K to 150 K, 500 points

# Function to calculate polarization P for a given particle's gamma
def calculate_polarization(gamma_val, T):
    dE = gamma_val * hbar * B  # Energy splitting in Joules
    P = np.tanh(dE / (2 * k * T))  # Polarization formula
    return P

# Gyromagnetic ratios for 1H, 13C, and an electron (E)
gamma_1H = gamma("1H")  # for proton
gamma_13C = gamma("13C")  # for carbon-13
gamma_electron = gamma("E")  # for electron

# Calculate P for each particle across temperature range T
P_1H = calculate_polarization(gamma_1H, T)
P_13C = calculate_polarization(gamma_13C, T)
P_electron = calculate_polarization(gamma_electron, T)

# Plotting
plt.figure(figsize=(6, 5))
plt.plot(T, P_1H, label="1H", color="blue")
plt.plot(T, P_13C, label="13C", color="orange")
plt.plot(T, P_electron, label="Electron", color="green")

# Set log scale for both x and y axes
plt.xscale("log")
plt.yscale("log")

# Set x and y axis limits
plt.xlim(1, 300)
```

```
plt.ylim(1e-6, 2)

# Labels, title, and grid
plt.xlabel("Temperature (K)")
plt.ylabel("Polarization (P)")
plt.legend()
plt.show()
```

## A.2. Bloch Equations

The following Mathematica code simulates the trajectory of a net magnetization vector under a $\pi/2$ pulse along the y-axis, followed by free precession around the z-axis. The code also visualizes the trajectory on a Bloch sphere.

```
Path = Append[Path, "/Users/others/Documents/Old_Dropbox/SDv3.7.0/SpinDynamica"];
Needs["SpinDynamica‘"]
SetSpinSystem[1];

rhoeq = ThermalEquilibriumDensityOperator[
    LarmorFrequency[1, 9.4] opI[1, "z"], 300];

{trajx, trajy, trajz} = Trajectory[
    12000 rhoeq -> {opI[1, "x"]/2, opI[1, "y"]/2, opI[1, "z"]/2},
    {{None, 2}},
    BackgroundGenerator -> CombineGenerators[2 Pi 3 opI[1, "z"],
    ThermalizeSuperoperator[PhenomenologicalRelaxationSuperoperator[{1, 1, 0.6}],
    opI[1, "z"], 300]]];

Show[SphereAndAxes[],
    ParametricPlot3D[{trajx[t], trajy[t], trajz[t]}, {t, 0, 12},
    PlotRange -> {{-0.55, 0.55}, {-0.55, 0.55}, {-0.55, 0.55}},
    PlotStyle -> {Purple, Thickness[0.02]}],
    Arrow3D[{0, 0, 0}, Directive -> {Purple, Thickness[0.01]}],
    Boxed -> False,
    ImageSize -> 200];
```

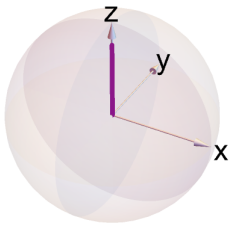


**Code A.2:** The net magnetization vector (in purple) undergoes a hypothetical sequence: a $\pi/2$ pulse rotates the magnetization vector around the y-axis.

```
{trajx, trajy, trajz} =
 Trajectory[12000 rhoeq -> {opI[1, "x"]/2, opI[1, "y"]/2, opI[1, "z"]/2},
  {RotationSuperoperator[1, {Pi/2, "y"}], {None, 2}},
   BackgroundGenerator -> CombineGenerators[2 Pi 0 opI[1, "z"],
   ThermalizeSuperoperator[
   PhenomenologicalRelaxationSuperoperator[{1, 1, 0.6}],
   opI[1, "z"], 300]]
```

```
  ]
Show[SphereAndAxes[],
  ParametricPlot3D[{trajx[t], trajy[t], trajz[t]}, {t, 0, 12},
  PlotRange -> {{-0.55, 0.55}, {-0.55, 0.55}, {-0.55, 0.55}},
  PlotStyle -> {Purple, Thickness[0.02]}],
  Arrow3D[{0, 0, 0}, Directive -> {Purple, Thickness[0.01]}],
  Boxed -> False, ImageSize -> 200];
```

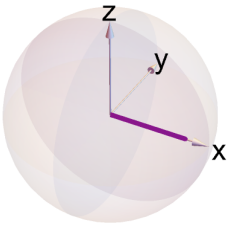


**Code A.3:** After $\pi/2$ pulse rotates the magnetization vector around the y-axis, followed by free precession of the spins around the z-axis.

```
{trajx, trajy, trajz} = Trajectory[
  12000 rhoeq -> {opI[1, "x"]/2, opI[1, "y"]/2, opI[1, "z"]/2},
  {RotationSuperoperator[1, {Pi/2, "y"}],
   RotationSuperoperator[1, {Pi/3, "z"}], {None, 2}},
   BackgroundGenerator -> CombineGenerators[2 Pi 0 opI[1, "z"],
   ThermalizeSuperoperator[PhenomenologicalRelaxationSuperoperator[{1, 1, 0.6}],
   opI[1, "z"], 300]]
  ]
Show[
  SphereAndAxes[],
  ParametricPlot3D[{trajx[t], trajy[t], trajz[t]}, {t, 0, 12},
  PlotRange -> {{-0.55, 0.55}, {-0.55, 0.55}, {-0.55, 0.55}},
  PlotStyle -> {Purple, Thickness[0.02]}],
  Arrow3D[{0, 0, 0}, Directive -> {Purple, Thickness[0.01]}],
  Boxed -> False, ImageSize -> 200];
```

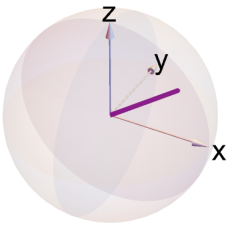


## A.3. Spin-Lattice Relaxation

Plot of Larmor frequency ($\omega_0$) vs the relaxation rate $T_1^{-1}$.

**Code A.4:** Calculation of $T_1^{-1}$ for proton as a function of Larmor frequency for two $\tau_c$ values, $\tau_c = 0.2$ ns (blue) and $\tau_c = 2$ ns (orange). The mean square fluctuating field was assumed $\langle B_x^2 \rangle = 10^{-4}\,\mathrm{T}^2$.

```
import numpy as np
import matplotlib.pyplot as plt

# Constants
```

```
gamma = 2.675e8  # Gyromagnetic ratio for 1H (rad/s/T)
B_rms = 100e-6   # RMS fluctuating field (T)
tau_c_values = [0.2e-9, 2e-9]

# Generate omega0 values (log scale from 1e1 to 1e12 rad/s)
omega0 = np.logspace(1, 12, 1000)

plt.figure(figsize=(6, 4.5))

# Plot for each tau_c
for tau_c in tau_c_values:
    term = (gamma**2 * B_rms**2) * tau_c / (1 + (omega0 * tau_c)**2)
    T1_inv = term
    label = f'tau_c = {tau_c:.1e} s'
    plt.semilogx(omega0, T1_inv, label=label)

# Mark critical omega0 where omega0*tau_c = 1
for tau_c in tau_c_values:
    omega_crit = 1 / tau_c
    plt.axvline(omega_crit, color='gray', linestyle='--', alpha=0.5,
    label=f'omega0 = 1/tau_c ({tau_c:.1e} s)')

plt.xlabel('Larmor Frequency $\omega_0$ (rad/s)')
plt.ylabel('Relaxation Rate $T_1^{-1}$ (s$^{-1}$)')
plt.legend()
plt.show()
```

Plot of correlation time ($\tau_c$) vs the relaxation rate $T_1^{-1}$.

**Code A.5:** Calculation of proton and carbon relaxation rates $T_1^{-1}$ as a function of correlation time at 1T and 9.4T.

```
import numpy as np
import matplotlib.pyplot as plt
from matplotlib import cm

# Constants
gamma_H = 2.675e8  # Gyromagnetic ratio for protons (rad T^-1 s^-1)
gamma_C = 6.728e7  # Gyromagnetic ratio for carbon (rad T^-1 s^-1)
B0_1T = 1
B0_9_4T = 9.4

# Larmor frequencies
omega_1T = [gamma_H * B0_1T, gamma_C * B0_1T]
omega_9_4T = [gamma_H * B0_9_4T, gamma_C * B0_9_4T]

# Correlation times
tau_c = np.logspace(-11, -7, 100)

# Spectral density function
def J(omega, tau_c):
    return tau_c / (1 + (omega * tau_c) ** 2)

def R1(omega, tau_c):
    return 3 * J(omega, tau_c) + 5 * J(2 * omega, tau_c)

def R2(omega, tau_c):
    return J(0, tau_c) + 3 * J(omega, tau_c) + 6 * J(2 * omega, tau_c)

# Colors using Viridis colormap
viridis = cm.get_cmap('viridis', 4)
```

```
colors = viridis(np.linspace(0, 1, 4))

# Plot setup
fig, ax = plt.subplots(figsize=(10,6))

# Hide top/right spines
ax.set_axis_on()

# Loop for 1H and 13C at 1T and 9.4T
omegas = [omega_1T[0], omega_9_4T[0], omega_1T[1], omega_9_4T[1]]
colors_idx = [0, 0, 1, 1]
linestyles = ['-', '--', '-', '--']

for i, omega in enumerate(omegas):
    R1_vals = R1(omega, tau_c)
    plt.loglog(tau_c, R1_vals, color=colors[colors_idx[i]], linestyle=linestyles[i], linewidth=2)

ax.set_xlim(1e-11, 1e-7)
ax.set_xlabel('Correlation time (s)')
ax.set_ylabel('T^-1 s^-1 relaxation rate (s^-1)')
plt.savefig('relaxation_times_clean_v3.png', dpi=600, bbox_inches='tight', pad_inches=0, transparent=False)

plt.show()
```

## A.4. Solomon Equation

**Code A.6:** Python code used for computing $^{13}$C relaxation rates at 1 T and 9.4 T.

```
import numpy as np
import matplotlib.pyplot as plt
from matplotlib import cm

# Constants
gamma = 6.728e7  # for 13C
B0_1T = 1
B0_9_4T = 9.4
omega_1T = gamma * B0_1T
omega_9_4T = gamma * B0_9_4T
tau_c = np.logspace(-11, -6, 100)

# Spectral density
def J(omega, tau_c):
    return tau_c / (1 + (omega * tau_c)**2)

# Relaxation rates
def R1(omega, tau_c):
    return (3 * J(omega, tau_c) + 5 * J(2 * omega, tau_c)) / 1e-9

def R2(omega, tau_c):
    return (J(0, tau_c) + 3 * J(omega, tau_c) + 6 * J(2 * omega, tau_c)) / 1e-9

# Compute relaxation rates
R1_1T = R1(omega_1T, tau_c)
R2_1T = R2(omega_1T, tau_c)
R1_9_4T = R1(omega_9_4T, tau_c)
R2_9_4T = R2(omega_9_4T, tau_c)

# Prepare Viridis colormap
```

```
viridis = cm.get_cmap('viridis', 4)
colors = viridis(np.linspace(0, 1, 4))

# Plot without axes, labels, or frame
fig, ax = plt.subplots(figsize=(8, 6))
ax.set_axis_off()
for spine in ax.spines.values():
    spine.set_visible(False)

# Plot curves
ax.loglog(tau_c, R1_1T, color=colors[0], linewidth=2)
ax.loglog(tau_c, R2_1T, color=colors[1], linewidth=2)
ax.loglog(tau_c, R1_9_4T, color=colors[0], linestyle='--', linewidth=2)
ax.loglog(tau_c, R2_9_4T, color=colors[1], linestyle='--', linewidth=2)

# Set axis limits manually
ax.set_xlim(1e-11, 1e-6)

# Save image with high DPI
plt.savefig('relaxation_rates.png', dpi=600, bbox_inches='tight', pad_inches=0, transparent=True)
```

## A.5. Experimental Determination of Relaxation Times

```
(* Parameters *)
Omega0 = 2 Pi;
T1 = 2;
T2 = 1;
times = Range[0, 12, 0.05];

(* Trajectories *)
trajxFunc[t_] := Sin[Omega0 t] Exp[-t/T2];
trajyFunc[t_] := -Cos[Omega0 t] Exp[-t/T2];
trajzFunc[t_] := 1 - Exp[-t/T1];

(* Trajectory curve *)
trajLine = ParametricPlot3D[
  {trajxFunc[t], trajyFunc[t], trajzFunc[t]},
  {t, 0, 12},
  PlotStyle -> {Blue, Thickness[0.015]},
  Mesh -> None
];

(* Axes with adjusted label placement *)
axisLen = 1.05; (* Reduced axis length to fit within PlotRange *)
axes = {
  {Black, Arrowheads[0.05], Arrow[{{0, 0, 0}, {axisLen, 0, 0}}],
   Text[Style["x", 20, Bold, Black], {axisLen, 0, 0}, {-1.2, 0}]},
  {Black, Arrowheads[0.05], Arrow[{{0, 0, 0}, {0, axisLen, 0}}],
   Text[Style["y", 20, Bold, Black], {0, axisLen, 0}, {0, -1.2}]},
  {Black, Arrowheads[0.05], Arrow[{{0, 0, 0}, {0, 0, axisLen}}],
   Text[Style["z", 20, Bold, Black], {0, 0, axisLen}, {0, -0.8}]}
};

(* Final plot with tighter range *)
Show[
  Graphics3D[{Opacity[0.5], Sphere[{0, 0, 0}, 1.0], Sequence @@ axes}],
  trajLine,
```

```
  Boxed -> False,
  Axes -> False,
  ImageSize -> 200,
  PlotRange -> {{-1.1, 1.1}, {-1.1, 1.1}, {-1.1, 1.1}},
  PlotRangePadding -> Scaled[0.001],
  ImagePadding -> 20,
  ViewAngle -> Pi/13
];
```

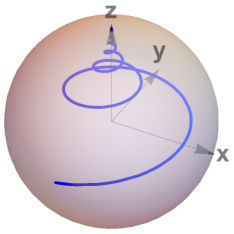


**Code A.7:** Trajectory of the tip of the magnetization vector after a $(\pi/2)_x$ pulse for various relaxation times $T_1$ and $T_2$

```
(* Second trajectory with T2 = 2 *)
T2 = 2;

trajLine = ParametricPlot3D[
  {trajxFunc[t], trajyFunc[t], trajzFunc[t]},
  {t, 0, 12},
  PlotStyle -> {Blue, Thickness[0.015]},
  Mesh -> None
];

Show[
  Graphics3D[{Opacity[0.5], Sphere[{0, 0, 0}, 1.0], Sequence @@ axes}],
  trajLine,
  Boxed -> False,
  Axes -> False,
  ImageSize -> 200,
  PlotRange -> {{-1.1, 1.1}, {-1.1, 1.1}, {-1.1, 1.1}},
  PlotRangePadding -> Scaled[0.001],
  ImagePadding -> 20,
  ViewAngle -> Pi/13
];
```

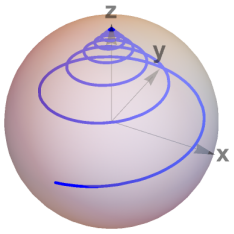


## A.6. $T_1$ Measurements - Inversion Recovery

```
Path = Append[Path, "/Users/others/Documents/Old_Dropbox/SDv3.7.0/SpinDynamica"];
Needs["SpinDynamica`"];
SetSpinSystem[1];
```

```
(* Thermal equilibrium density operator *)
rho_eq = ThermalEquilibriumDensityOperator[
    LarmorFrequency[1, 9.4] opI[1, "z"], 300
];

(* Parameters *)
T1 = 2;
M0 = 1;
taus = {0, 1, 5, 10};  (* tau values in seconds *)

(* Recovery function after inversion *)
MzFunc[t_] := M0 (1 - 2 Exp[-t/T1]);

(* Function to create Bloch sphere with vector at given tau *)
BlochSphereWithVector[tau_] :=
  Graphics3D[
    {
      {Opacity[0.2], Sphere[{0, 0, 0}, 1]},  (* Bloch sphere *)
      {Black, Arrow[{{0, 0, 0}, {1.1, 0, 0}}], Text[Style["x", Bold, 12], {1.2, 0, 0}]},
      {Black, Arrow[{{0, 0, 0}, {0, 1.1, 0}}], Text[Style["y", Bold, 12], {0, 1.2, 0}]},
      {Black, Arrow[{{0, 0, 0}, {0, 0, 1.1}}], Text[Style["z", Bold, 12], {0, 0, 1.2}]},
      {Blue, Thick, Arrow[{{0, 0, 0}, {0, 0, MzFunc[tau]}}]},  (* Relaxation vector *)
      Text[Style["Tau = " <> ToString[tau], 16, Blue], {0.8, -0.8, -1}]  (* Label *)
    },
    Boxed -> False,
    Axes -> False,
    PlotRange -> {{-1.1, 1.1}, {-1.1, 1.1}, {-1.1, 1.1}},
    PlotRangePadding -> Scaled[0.001],
    ImagePadding -> 4,
    ImageSize -> 200,
    ViewAngle -> Pi/11
  ];

(* Generate panel of Bloch spheres for each tau *)
GraphicsRow[BlochSphereWithVector /@ taus, Spacings -> Scaled[0]]
```

**Code A.8:** SpinDynamica code: $T_1$ Measurements - Inversion Recovery

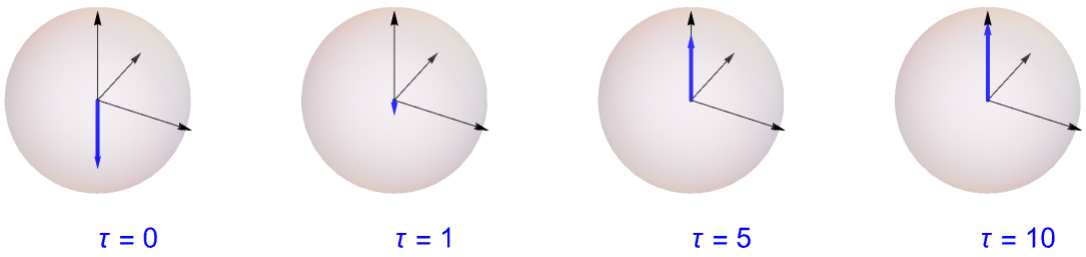

## A.7. EPR Spectrum

In the liquid state, the solution is isotropic and averages g-tensor values, but this does not apply to solid samples. When the solution is glassy in DNP, all orientations are equally probable, and the resulting spectra, averaged over these orientations, are called powder spectra[115]. For a particular orientation S ( $\omega, \phi, \theta$ ) the EPR spectrum is defined by:

$$S_{\text{powder}}(\omega) = \frac{1}{4\pi} \iint S(\omega, \phi, \theta)\ \sin\theta\, d\theta\, d\phi \tag{A.1}$$

Here, $\sin\theta$ represents the decreasing probability of the orientation from angle 0 to $\pi$. The EPR spectrum can be simulated by computing $g_{\text{eff}}$ for randomly oriented molecules and then translating these into resonance frequencies. The spectra can be shown in Gaussian form as described below.

$$K\left(g_{\text{eff}}, g\right) = \frac{1}{\sqrt{2\pi\sigma^2}} \exp\left(-\frac{(g - g_{\text{eff}})^2}{2\sigma^2}\right) \tag{A.2}$$

To do that, the g-tensor should be in the lab frame, which rotates with respect to the PAF frame. The rotations are defined by the Euler angles $\alpha$, $\beta$, and $\gamma$ for molecular orientations and the spherical angles $\theta$ and $\phi$ for the magnetic field direction. If the rotation by angle $\gamma$ is applied, which ensures axial spin rotation from 0 to $2\pi$ about the z-axis, then the corresponding rotation matrix can be defined as:

$$R_z(\gamma) = \begin{bmatrix} \cos\gamma & \sin\gamma & 0 \\ -\sin\gamma & \cos\gamma & 0 \\ 0 & 0 & 1 \end{bmatrix} \tag{A.3}$$

Now apply the rotation by angle $\beta$ from 0 to $\pi$ about the lab frame y-axis, on the rotated matrix $R_z(\gamma)$. This tilts the molecular z-axis away from the lab z-axis.

$$R_y(\beta) = \begin{bmatrix} \cos\beta & 0 & -\sin\beta \\ 0 & 1 & 0 \\ \sin\beta & 0 & \cos\beta \end{bmatrix} \tag{A.4}$$

The next rotation can be applied by an angle $\alpha$ from 0 to $2\pi$ about the lab frame z- axis on matrix $R_y(\beta)$.This rotation causes the molecule to spin around its symmetry axis, similar to a spinning top.

$$R_z(\alpha) = \begin{bmatrix} \cos\alpha & \sin\alpha & 0 \\ -\sin\alpha & -\sin\alpha & 0 \\ 0 & 0 & 1 \end{bmatrix} \tag{A.5}$$

The g-tensors are defined within the molecular frames, but measurements are done in the lab frame. The Euler rotation matrix R, which is a zyz rotation matrix, mathematically rotates the molecular axes to align with the lab frame represented below.

$$R(\alpha, \beta, \gamma) = R_z(\alpha)\, R_y(\beta)\, R_z(\gamma) \quad =$$

$$\begin{pmatrix} -\sin\alpha\sin\gamma + \cos\alpha\cos\beta\cos\gamma & \sin\alpha\cos\gamma + \sin\gamma\cos\alpha\cos\beta & -\sin\beta\cos\alpha \\ -\sin\alpha\cos\beta\cos\gamma - \sin\gamma\cos\alpha & -\sin\alpha\sin\gamma\cos\beta + \cos\alpha\cos\gamma & \sin\alpha\sin\beta \\ \sin\beta\cos\gamma & \sin\beta\sin\gamma & \cos\beta \end{pmatrix} \tag{A.6}$$

With complete rotation, now $g_{\text{eff}}$ can be calculated, which helps determine the resonance condition for each orientation. The next step is to convert these $g_{\text{eff}}$ values into frequencies to see the spectrum, using the following equation.

$$\nu = \frac{g_{\text{eff}}\, \mu_B\, B_0}{h} \tag{A.7}$$

**Code A.9:** EPR spectra of the TEMPO (blue) and Trityl OX063 (orange) using $g_{\text{eff}}$ values.

```
import numpy as np
import matplotlib.pyplot as plt

# Constants
mu_B = 9.274e-24  # Bohr magneton (J/T)
h = 6.626e-34     # Planck's constant (J*s)
B0 = 6.7          # Magnetic field (T)

# g-Tensors (molecular frame)
g_TEMPO = np.diag([2.0094, 2.0065, 2.0017])**2  # Squared for efficiency
g_Trityl = np.diag([2.00319, 2.00319, 2.00258])**2

# Sample molecular orientations uniformly on a sphere
N = 100000  # Number of orientations (increase for smoother spectra)
cos_beta = 2 * np.random.rand(N) - 1  # Uniform in cos(beta)
beta = np.arccos(cos_beta)
alpha = 2 * np.pi * np.random.rand(N)
gamma = 2 * np.pi * np.random.rand(N)  # Include gamma rotation

# Magnetic field direction in lab frame (fixed along Z)
B_lab = np.array([0, 0, 1])

def get_g_eff_sq(g_tensor_mol, alpha, beta, gamma):
    """Compute squared effective g-factor for given orientation"""
    # Rotation matrix (active ZYZ convention)
    Rz_alpha = np.array([
        [np.cos(alpha), -np.sin(alpha), 0],
        [np.sin(alpha),  np.cos(alpha), 0],
        [0, 0, 1]
    ])
    Ry_beta = np.array([
        [np.cos(beta), 0, np.sin(beta)],
        [0, 1, 0],
        [-np.sin(beta), 0, np.cos(beta)]
    ])
    Rz_gamma = np.array([
        [np.cos(gamma), -np.sin(gamma), 0],
        [np.sin(gamma),  np.cos(gamma), 0],
        [0, 0, 1]
    ])
    R = Rz_alpha @ Ry_beta @ Rz_gamma

    # Transform g-tensor to lab frame and compute g_eff^2
    g_sq_lab = R @ g_tensor_mol @ R.T
    return B_lab @ g_sq_lab @ B_lab  # = g_eff^2

# Precompute g_eff^2 for all orientations
g_eff_sq_TEMPO = np.array([get_g_eff_sq(g_TEMPO, a, b, g)
                           for a, b, g in zip(alpha, beta, gamma)])
g_eff_sq_Trityl = np.array([get_g_eff_sq(g_Trityl, a, b, g)
                            for a, b, g in zip(alpha, beta, gamma)])

# Convert to g_eff
g_vals_TEMPO = np.sqrt(g_eff_sq_TEMPO)
g_vals_Trityl = np.sqrt(g_eff_sq_Trityl)

# Define g-axis globally for spectrum and frequency
g_axis = np.linspace(1.99, 2.02, 600)
```

```
# Build spectra
def build_spectrum(g_vals, g_axis, sigma=0.0002):
    spectrum = np.zeros_like(g_axis)
    for g in g_vals:
        spectrum += np.exp(-((g_axis - g)**2) / (2 * sigma**2))

    dx = g_axis[1] - g_axis[0]
    area = np.sum(spectrum) * dx
    return spectrum / area

spectrum_TEMPO = build_spectrum(g_vals_TEMPO, g_axis)
spectrum_Trityl = build_spectrum(g_vals_Trityl, g_axis)

# Convert to frequency (GHz)
freq_axis = g_axis * mu_B * B0 / h / 1e9

# Plot
plt.figure(figsize=(6, 5))
plt.plot(freq_axis, spectrum_TEMPO, label='TEMPO')
plt.plot(freq_axis, spectrum_Trityl, label='Trityl')
plt.xlim(187.5, 188.5)
plt.xlabel("Frequency (GHz)")
plt.ylabel("Normalized Intensity")
plt.title("Simulated EPR Spectra")
plt.legend()
plt.grid(True)
plt.show()
```

## A.8. Evolution of INEPT

The evolution of product operators for a 4-spin system (i.e., $CH_3$) under $H = 2\pi J_{14} I_{1z} S_z + 2\pi J_{24} I_{2z} S_z + 2\pi J_{34} I_{3z} S_z$. The delay used in the pulse sequence is DEL1 and DEL2. For simplicity, let us assume that $\tau_1/2$ = DEL1 and $\tau_2/2$ = DEL2. can be described as follows:

$$S_z \xrightarrow{90_x(S)} -S_y \xrightarrow{180_x(I,S)} S_y \xrightarrow{2\pi J_{14} I_{1z} S_z,\, \tau_1} S_y \cos(\pi J_{14}\tau_1) - 2I_{1z}S_x \sin(\pi J_{14}\tau_1)$$

$$\downarrow 2\pi J_{24} I_{2z} S_z,\, \tau_1$$

$$\begin{aligned} &S_y \cos(\pi J_{14}\tau_1)\cos(\pi J_{24}\tau_1) - 2I_{1z}S_x \sin(\pi J_{14}\tau_1)\cos(\pi J_{24}\tau_1) - 2I_{2z}S_x \cos(\pi J_{14}\tau_1)\sin(\pi J_{24}\tau_1) \\ &\quad - 4I_{1z}I_{2z}S_y \sin(\pi J_{14}\tau_1)\sin(\pi J_{24}\tau_1) \end{aligned}$$

$$\downarrow 2\pi J_{34} I_{3z} S_z,\, \tau_1$$

$$\begin{aligned} &S_y \cos(\pi J_{14}\tau_1)\cos(\pi J_{24}\tau_1)\cos(\pi J_{34}\tau_1) - 2I_{1z}S_x \sin(\pi J_{14}\tau_1)\cos(\pi J_{24}\tau_1)\cos(\pi J_{34}\tau_1) \\ &- 2I_{2z}S_x \cos(\pi J_{14}\tau_1)\sin(\pi J_{24}\tau_1)\cos(\pi J_{34}\tau_1) - 4I_{1z}I_{2z}S_y \sin(\pi J_{14}\tau_1)\sin(\pi J_{24}\tau_1)\cos(\pi J_{34}\tau_1) \\ &- 2I_{3z}S_x \cos(\pi J_{14}\tau_1)\cos(\pi J_{24}\tau_1)\sin(\pi J_{34}\tau_1) - 4I_{1z}I_{3z}S_y \sin(\pi J_{14}\tau_1)\cos(\pi J_{24}\tau_1)\sin(\pi J_{34}\tau_1) \\ &- 4I_{2z}I_{3z}S_y \cos(\pi J_{14}\tau_1)\sin(\pi J_{24}\tau_1)\sin(\pi J_{34}\tau_1) + 8I_{1z}I_{2z}I_{3z}S_x \sin(\pi J_{14}\tau_1)\sin(\pi J_{24}\tau_1)\sin(\pi J_{34}\tau_1) \end{aligned}$$

$$\downarrow 90_y(I,S);\, 180_x(I,S)$$

$$\begin{aligned} &- S_y \cos(\pi J_{14}\tau_1)\cos(\pi J_{24}\tau_1)\cos(\pi J_{34}\tau_1) - 2I_{1x}S_z \sin(\pi J_{14}\tau_1)\cos(\pi J_{24}\tau_1)\cos(\pi J_{34}\tau_1) \\ &- 2I_{2x}S_z \cos(\pi J_{14}\tau_1)\sin(\pi J_{24}\tau_1)\cos(\pi J_{34}\tau_1) - 2I_{3x}S_z \cos(\pi J_{14}\tau_1)\cos(\pi J_{24}\tau_1)\sin(\pi J_{34}\tau_1) \\ &+ 4I_{1x}I_{2x}S_y \sin(\pi J_{14}\tau_1)\sin(\pi J_{24}\tau_1)\cos(\pi J_{34}\tau_1) + 4I_{1x}I_{3x}S_y \sin(\pi J_{14}\tau_1)\cos(\pi J_{24}\tau_1)\cos(\pi J_{34}\tau_1) \\ &+ 4I_{2x}I_{3x}S_y \cos(\pi J_{14}\tau_1)\sin(\pi J_{24}\tau_1)\sin(\pi J_{34}\tau_1) + 8I_{1x}I_{2x}I_{3x}S_z \sin(\pi J_{14}\tau_1)\sin(\pi J_{24}\tau_1)\sin(\pi J_{34}\tau_1) \end{aligned}$$

Keeping in mind that we eventually detect proton coherences. This coherence enables the final detectable signal to consist only of those components ordered by the scalar interaction (2 $J_{CH}$). It is therefore necessary to consider the terms that result in a detectable signal for further evolution. The terms having heteronuclear coupling active ($-2I_{1x}S_z, -2I_{2x}S_z, -2I_{3x}S_z$) will contribute to the inphase detectable signal.

$$\begin{aligned} &- 2I_{1x}S_z \sin(\pi J_{14}\tau_1)\cos(\pi J_{24}\tau_1)\cos(\pi J_{34}\tau_1) - 2I_{2x}S_z \cos(\pi J_{14}\tau_1)\sin(\pi J_{24}\tau_1)\cos(\pi J_{34}\tau_1) \\ &- 2I_{3x}S_z \cos(\pi J_{14}\tau_1)\cos(\pi J_{24}\tau_1)\sin(\pi J_{34}\tau_1) \xrightarrow{J,\tau_2} -4I_{1y} \sin(\pi J_{14}\tau_1)\cos(\pi J_{24}\tau_1)\cos(\pi J_{34}\tau_1) \\ &\quad - 4I_{2y} \cos(\pi J_{14}\tau_1)\sin(\pi J_{24}\tau_1)\cos(\pi J_{34}\tau_1) - 4I_{3y} \cos(\pi J_{14}\tau_1)\cos(\pi J_{24}\tau_1)\sin(\pi J_{34}\tau_1). \end{aligned}$$

Polarization transfer from pyruvate [2-$^{13}$C] to the methyl protons corresponds to the case $N = 3$. Ideally, each methyl proton acquires a polarization equal to 0.387 times the polarization of the $S$-spin. Accounting for the three equivalent protons and the gyromagnetic ratio factor, the hyperpolarized magnetization is enhanced by $3 \times 0.387$. The $^2J_{\mathrm{CH}}$ between $C_2$ and the methyl protons is $J = 7$ Hz, which leads to relatively short optimal delays. In the absence of relaxation, the optimal delays used in this study were

$$\tau_1 = 2\big(\mathrm{DEL1} + p4/2\big) = 25 \text{ ms},$$
$$\tau_2 = 2\big(\mathrm{DEL2} + (p19 - 0.11 \text{ ms}) + (p1 \cdot 2.3846 + d5 \cdot 2.5)\big) = 61 \text{ ms},$$

where DEL1 and DEL2 denote the center-to-center delays of the first and second $^1$H-$^{13}$C spin echoes. There is a total of 86 ms between the first $^{13}$C pulse and the echo at the end of the reverse-INEPT module.

The coherence transfer pathways can be simulated using SpinDynamica as shown below:

## SpinDynamica Simulation Code

```
$Path = Append[$Path, "/Users/others/Dropbox/SDv3.7.0/SpinDynamica"];
$Path = Append[$Path, "/home/benno/SpinDynamica/SDv3.7.1/SpinDynamica"];

Needs["SpinDynamica‘"];

SpinDynamica version 3.7.1 loaded by Mathematica 13.1 running on Linux x86 (64-bit).

(* Additional definitions given to symbols *)
{Dot, Duration, Exp, Expand, Plus, Power, Simplify, SolidAngle, Times, WignerD}

(* Thermal Polarization Levels (9.4 T, 300 K) *)
Quiet[SetSpinSystem[4]];
Ispins = {1, 2, 3};
Sspins = {4};

ρ_eq = ThermalEquilibriumDensityOperator[
           LarmorFrequency[1, 9.4] opI[{Ispins}, "z"], 300] +
       ThermalEquilibriumDensityOperator[
           LarmorFrequency[13, 9.4] opI[{Sspins}, "z"], 300];

Meq = OperatorAmplitude[ρ_eq -> opI["z"]];

PLO = PolarizationLevelOperator[Ispins];
P1H = OperatorAmplitude[ρ_eq -> PLO] // EngineeringForm;

PLO = PolarizationLevelOperator[4];
P13C = OperatorAmplitude[ρ_eq -> PLO] // EngineeringForm;

(* Output *)
Out[11] = 1/8 (I_{1z} + I_{2z} + I_{3z});

Out[12] // EngineeringForm = 3.20132 \times 10^{-5};
Out[14] // EngineeringForm = 8.05144 \times 10^{-6};

(* 13C - 1H transfer without relaxation at 300 K from 13C thermal equilibrium *)
HJ[J_] = 2 \pi 7 opI[1, "z"].opI[4, "z"] + 2 \pi 7 opI[2, "z"].opI[4, "z"]
             + 2 \pi 7 opI[3, "z"].opI[4, "z"];

HJ[J_] /. {J -> 7};

H_lab = LarmorFrequency[13, 9.4] opI[{4}, "z"];
ρ_Θ = ThermalEquilibriumDensityOperator[H_lab, 300];
Meq = OperatorAmplitude[ρ_Θ -> opI[{Sspins}, "z"]];

L = CombineGenerators[HJ[J_]];
```

```
(* Start with only 13C polarization *)
ρ_eq = ThermalEquilibriumDensityOperator[ LarmorFrequency[13, 9.4] opI[{Sspins}, "z"], 300];

INEPT[τ_] := {RotationSuperoperator[{Sspins}, {π/2, "x"}], {None, 0.4 τ},
              RotationSuperoperator[{π, "x"}], {None, 0.4 τ},
              RotationSuperoperator[{π/2, "y"}], {None, τ},
              RotationSuperoperator[{π, "x"}], {None, τ}};

trajy1 = Trajectory[ρ_eq -> opI[1, "y"], INEPT[1/(4 7)], BackgroundGenerator -> L,
             NormalizationFactor -> 3.20132*10^-5 / 8];

trajy4 = Trajectory[ρ_eq -> opI[4, "y"], INEPT[1/(4 7)], BackgroundGenerator -> L,
          NormalizationFactor -> 8.05144*10^-6 / 8];

trajy10 = Trajectory[ρ_eq -> opI[1, "y"], INEPT[1/(4 7)], BackgroundGenerator -> L,
           NormalizationFactor -> 3.20132*10^-5 / 8 / 10];

Plot[{trajy4[t], trajy1[t], trajy10[t]},
     {t, 0, Duration[INEPT[1/(4 7)]]}, FrameLabel -> {"Time (s)"},
     PlotLegends -> {"<Sy> (13C)", "<Iy> (1H)", "<Iy> * 10"},
     PlotStyle -> {Black, Blue, {Blue, Dashed}}];
```

### Hamiltonian Output

$$H_J = 14\pi(I_{1z} \bullet I_{4z}) + 14\pi(I_{2z} \bullet I_{4z}) + 14\pi(I_{3z} \bullet I_{4z})$$

Out[ ]=

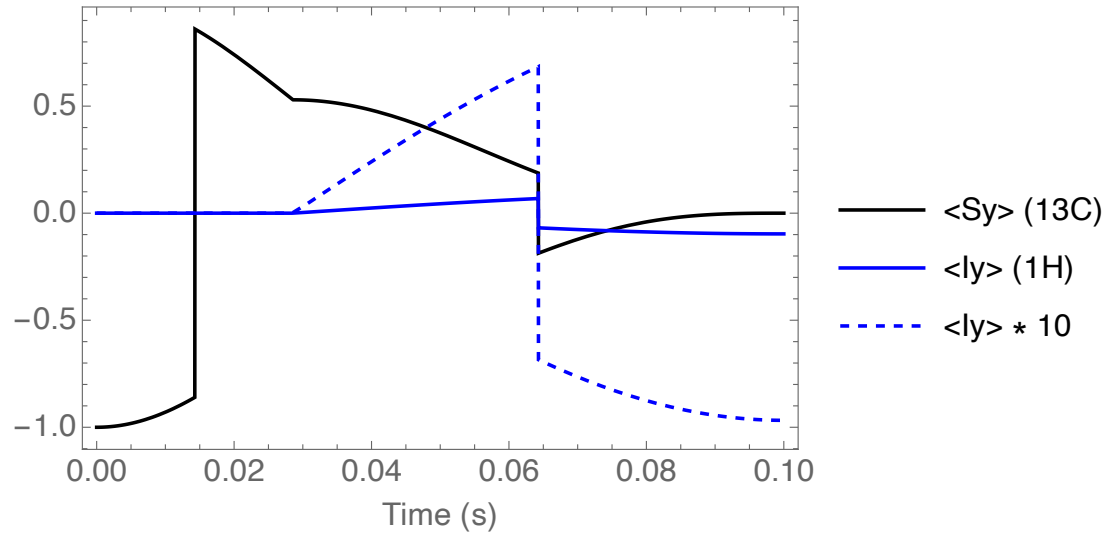


**Figure A.1.:** Coherence transfer pathways from $^{13}C$ to $^{1}H$ and multiplied by a factor of 10 (shown in dotted blue).

## A.9. Cryoprobe Sensitivity Gain

To assess the potential sensitivity enhancement achievable with a cryoprobe, the Bruker standard sucrose sample was measured using both the 400 MHz probes employed in this work and a CP-TCI 600 MHz cryoprobe at ETH Zürich (measurements performed by Lorz.N, a co-author). Signal-to-noise ratios (SNRs) were determined using the Bruker macro `supcal`, and the results are summarized in Table A.1. After correcting for the increased polarization at the higher magnetic field (by dividing the cryoprobe SNR by a factor of 1.5), the cryoprobe exhibited an SNR approximately 8.5 times higher than the most sensitive 400 MHz probe used for the hyperpolarization experiments.

| Probe | $^{1}$H Frequency | SNR | SNR at 400 MHz (Polarization) |
|---|---|---|---|
| TBI 400S1 H/C-BB-D-05 Z | 400 MHz | 102 | 102 |
| BBO 400S1 BBF-H-D-05 Z | 400 MHz | 71 | 71 |
| CP-TCI H & F-N/C-D-05 Z | 600 MHz | 1295 | 863 |

**Table A.1.:** Sensitivities of different Bruker probes estimated using the Bruker sucrose standard sample. Pulse sequence: `zgpr`. Acquisition parameters: TD = 1 s, 8 scans, 4 dummy scans, d1 = 5 s. The column "SNR at 400 MHz (Polarization)" reports the expected cryoprobe SNR if operated at 400 MHz instead of 600 MHz, corrected for the field-dependent polarization.

The reverse INEPT sequence used in this work suppresses contributions from thermal proton magnetization, ensuring that only polarization transferred from $^{13}$C is observed. When combined with a cryoprobe at a higher magnetic field, the achievable detection sensitivity can be improved by nearly an order of magnitude. Importantly, the injection device used in the experimental setup has an outer diameter of only 25 mm, making it fully compatible with standard 5 mm liquid-state cryoprobes.

## A.10. $^{13}$C Relaxation Simulation

The following Python script was used to compute and visualize field-dependent relaxation rates ($R_1$, $R_2$) for $^{13}$C nuclei dipolar-coupled to protons under different binding fractions. The calculations employ the standard spectral density function formalism using the Lipari-Szabo model-free approach.

**Code A.10:** Python script for field-dependent relaxation analysis

```
import numpy as np
import matplotlib.pyplot as plt
import matplotlib.cm as cm

# Physical constants
mu_0 = 4 * np.pi * 1e-7
hbar = 1.0545718e-34
gamma_H = 2.675e8
gamma_C = 6.728e7
r_CH = 2.0e-10

# Dipolar interaction constant
K = (mu_0**2 * hbar**2 * gamma_H**2 * gamma_C**2) / (16 * np.pi**2 * r_CH**6)

def J(omega, tau_c, tau_e, S2):
    tau_eff = (tau_c * tau_e) / (tau_c + tau_e)
    return (2 / 5) * (
```

```
        (S2 * tau_c) / (1 + (omega * tau_c)**2) +
        ((1 - S2) * tau_eff) / (1 + (omega * tau_eff)**2)
    )

def calc_relaxation(B0, tau_c, tau_e, S2):
    omega_H = gamma_H * B0
    omega_C = gamma_C * B0

    J_HmC = J(omega_H - omega_C, tau_c, tau_e, S2)
    J_HpC = J(omega_H + omega_C, tau_c, tau_e, S2)
    J_H   = J(omega_H, tau_c, tau_e, S2)
    J_C   = J(omega_C, tau_c, tau_e, S2)
    J_0   = J(0, tau_c, tau_e, S2)

    R1 = (K/4) * (J_HmC + 3 * J_H + 6 * J_HpC)
    R2 = (K/8) * (4*J_0 + J_HmC + 3*J_H + 6*J_C + 6*J_HpC)
    sigma_CH = (K/4) * (6*J_HpC - J_HmC)
    NOE = 1 + (gamma_H / gamma_C) * sigma_CH / R1

    return R1, R2, NOE

# Parameters
B0_values = np.logspace(np.log10(0.1), np.log10(15), 200)
binding_fractions = [100, 50, 0]

states = {
    "Free": {"tau_c": 10e-12, "tau_e": 10e-12, "S2": 0.05},
    "Bound": {"tau_c": 10e-9, "tau_e": 100e-12, "S2": 0.95}
}

# Compute R1 and R2
profiles_R1, profiles_R2 = {}, {}
for p in binding_fractions:
    f_bound = p / 100
    R1_list, R2_list = [], []

    for B0 in B0_values:
        R1_f, R2_f, _ = calc_relaxation(B0, **states["Free"])
        R1_b, R2_b, _ = calc_relaxation(B0, **states["Bound"])

        R1 = (1 - f_bound) * R1_f + f_bound * R1_b
        R2 = (1 - f_bound) * R2_f + f_bound * R2_b

        R1_list.append(R1)
        R2_list.append(R2)

    profiles_R1[p] = R1_list
    profiles_R2[p] = R2_list

# Plotting
fig, ax = plt.subplots(figsize=(6, 5))
cmap = cm.get_cmap("viridis")

for i, p in enumerate(binding_fractions):
    # Avoid bright yellow: restrict sampling to [0.1, 0.7]
    color = cmap(0.1 + 0.6 * (i / (len(binding_fractions) - 1)))
    ax.plot(B0_values, profiles_R1[p], linestyle='-', linewidth=2.5, color=color)
    ax.plot(B0_values, profiles_R2[p], linestyle='--', linewidth=2.5, color=color)

ax.set_xscale("log")
```

```
ax.set_yscale("log")
ax.set_xlim(0.1, 10)
ax.set_ylim(0.0025, 6)
ax.set_xlabel("B$_0$ (Tesla)")
ax.set_ylabel("Relaxation Rate (s$^{-1}$)")
plt.show()

# Save figure
fig.savefig("Fig5.8.png", dpi=600, bbox_inches='tight', pad_inches=0, transparent=True)
```

## A.11. Expression and Purification of PHD1 Protein

The following text is reproduced with minor modifications from a published work (Narwal et al.[96]). The expression of PHD1 was achieved using plasmid DNA (`pET-28b(+)`) encoding a $His_6$-GB1-Prescission-PHD1(168–407) construct, which was transformed into *E. coli* BL21(DE3) CodonPlus RIL cells (Agilent) using the heat-shock method. Following transformation, colonies were deposited overnight at 37 °C on LB agar plates supplemented with chloramphenicol (34 $\mu$g/mL) and kanamycin (50 $\mu$g/mL). These colonies were used to inoculate LB preculture, which was grown overnight at 30 °C with shaking.

Protein expression was carried out in 2×YT medium supplemented with 10 g/L glycerol, 25 mM $KH_2PO_4$, 25 mM $Na_2HPO_4$, 2.5 mM $Na_2SO_4$, and in-house prepared metal mixes (1000× and 10000×). All cultures contained chloramphenicol (34 $\mu$g/mL) and kanamycin (50 $\mu$g/mL). Main cultures (1 L in 5 L baffled Erlenmeyer flasks) were inoculated with an appropriate volume of preculture (typically ~15 mL per liter) to achieve an initial $OD_{600}$ of 0.1 and grown at 30 °C with shaking until $OD_{600}$ reached 2.

The cultures were then cooled to 18 °C for 30 min before induction with 1 mM isopropyl $\beta$-D-1-thiogalactopyranoside (IPTG). Protein expression proceeded overnight at 18 °C, after which cells were harvested by centrifugation (6000 ×$g$, 10 min, 4 °C).

Cell lysis was performed in lysis buffer (50 mM Tris, pH 8.0, 300 mM NaCl, 5 mM imidazole, 1 mM DTT, 1 mM PMSF, and 10% (v/v) glycerol) supplemented with DNase I (AppliChem), using an LM10 Microfluidizer (Microfluidics). The lysate was clarified by centrifugation (35,000 ×$g$, 45 min, 4 °C) and vacuum-filtered through a 0.45 $\mu$m nitrocellulose membrane (Merck MF-Millipore).

$Ni^{2+}$-affinity purification was performed using a 5 mL Ni-NTA Superflow Cartridge (Qiagen) pre-equilibrated with washing buffer (50 mM Tris, pH 8.0, 300 mM NaCl, 5 mM imidazole, 1 mM DTT, and 10% (v/v) glycerol). The protein was step-eluted with elution buffer (50 mM Tris, pH 8.0, 300 mM NaCl, 250 mM imidazole, 1 mM DTT, and 10% (v/v) glycerol), and the buffer was exchanged back to washing buffer using a HiPrep 26/10 Desalting Column (GE).

To remove the $His_6$-GB1 tag, in-house produced 3C protease was added, and the mixture was incubated for 3 h at 4 °C. Protease and cleaved tags were removed by reverse $Ni^{2+}$-affinity chromatography using a 5 mL Ni-NTA Superflow Cartridge pre-equilibrated with washing buffer.

To replace Fe(II) in the active site with Mn(II), the protein was supplemented with 2 mM $MnCl_2$ and incubated overnight at 4 °C. The sample was then concentrated to ~250 $\mu$M using a 10 kDa Amicon Ultra-15 centrifugal filter (Merck Millipore) and further purified by size-exclusion chromatography on

a Superdex 75 Increase 16/600 column (GE), equilibrated with 50 mM Tris, pH 7.5, 300 mM NaCl, and 1 mM DTT. The protein was concentrated to ~100 $\mu$M, aliquoted, flash-frozen in liquid nitrogen, and stored at −80 °C until further use.

## A.12. Methyl Group Dipolar Relaxation and Binding Simulation

The following Python script was used to calculate $^{13}$C pyruvate relaxation rates ($R_1$) as a function of protein concentration and dissociation constant ($K_d$).

**Code A.11:** $^{13}$C Relaxation as function of differenent binding dissociation constant ($K_d$ at 1.3 T.

```
import numpy as np
import matplotlib.pyplot as plt
import pandas as pd
from scipy.optimize import root_scalar

# Constants (updated for methyl group)
mu_0 = 4 * np.pi * 1e-7
gamma_H = 2.675e8
gamma_C = 6.728e7
hbar = 1.0545718e-34
r_free = 0.220e-9  # adjusted for 2-13C to 3rd carbon methyl proton distance
r_bound = 0.229e-9
n_protons = 3  # Methyl group has 3 protons
pyruvate_conc = 20  # $\mu$M
tau_c_bound = 10e-9  # Bound state correlation time

def calculate_A(r):
    return (3/10) * (mu_0/(4*np.pi))**2 * gamma_C**2 * gamma_H**2 * hbar**2 / r**6

A_free = n_protons * calculate_A(r_free)
A_bound = n_protons * calculate_A(r_bound)

def objective(tau_c):
    B0 = 9.4
    omega_C = gamma_C * B0
    omega_H = gamma_H * B0
    omega_diff = np.abs(omega_H - omega_C)
    omega_sum = omega_H + omega_C
    J_diff = (2 * tau_c)/(1 + (omega_diff * tau_c)**2)
    J_C = (2 * tau_c)/(1 + (omega_C * tau_c)**2)
    J_sum = (2 * tau_c)/(1 + (omega_sum * tau_c)**2)
    return A_free * (J_diff + 3*J_C + 6*J_sum) - 1/30  # Target T1 = 15 s

solution = root_scalar(objective, bracket=[1e-13, 1e-10], method='brentq')
tau_c_free = solution.root

def J(omega, tau_c):
    return (2 * tau_c) / (1 + (omega * tau_c)**2)

def calculate_R1(B0, p_B):
    omega_C = gamma_C * B0
    omega_H = gamma_H * B0
    omega_diff = np.abs(omega_H - omega_C)
    omega_sum = omega_H + omega_C
    R1_free = A_free * (J(omega_diff, tau_c_free) + 3*J(omega_C, tau_c_free) + 6*J(omega_sum, tau_c_free))
```

```
    R1_bound = A_bound * (J(omega_diff, tau_c_bound) + 3*J(omega_C, tau_c_bound) + 6*J(omega_sum,
     tau_c_bound))
    return (1 - p_B)*R1_free + p_B*R1_bound

def simulate_R1(protein_conc, Kd_values, B0):
    R1_values = []
    L = pyruvate_conc
    for Kd in Kd_values:
        if protein_conc == 0:
            p_B = 0.0
        else:
            Pt = protein_conc
            a = 1
            b = -(Pt + L + Kd)
            c = Pt * L
            sqrt_disc = np.sqrt(b**2 - 4*a*c)
            x = (-b - sqrt_disc) / 2
            x = np.clip(x, 0, min(Pt, L))
            p_B = x / L
        R1_values.append(calculate_R1(B0, p_B))
    return np.array(R1_values)

def print_T1_table():
    selected_Kds = [1, 10, 100, 1000, 10000]
    B0_fields = [1.3]
    protein_concs = [0, 1, 2]
    print("\nT1 (seconds) for Key Kd Values:")
    print(f"{'Kd ($\mu$M)':<10}", end="")
    for B0 in B0_fields:
        for prot in protein_concs:
            label = f"{prot}$\mu$M@{B0}T"
            print(f"{label:<15}", end="")
    print("\n" + "-"*(10 + 15*8))
    for kd in selected_Kds:
        print(f"{kd:<10}", end="")
        for B0 in B0_fields:
            for prot in protein_concs:
                R1 = simulate_R1(prot, [kd], B0)[0]
                T1 = 1/R1 if R1 != 0 else float('inf')
                print(f"{T1:.2f}{' '*(15-len(f'{T1:.2f}'))}", end="")
        print()

B0_fields = [1.3]
protein_concs = [0, 1, 2]
Kd_values = np.logspace(0, 4, 500)

plt.figure(figsize=(12, 7))
colors = ['#000000', '#1f77b4', '#d62728', '#9467bd']
linestyles = ['-', '--']
for j, B0 in enumerate(B0_fields):
    for i, prot in enumerate(protein_concs):
        R1_vals = simulate_R1(prot, Kd_values, B0)
        label = f'{prot} $\mu$M Protein @ {B0} T' if prot > 0 else f'Free @ {B0} T'
        plt.plot(Kd_values, R1_vals, color=colors[i], linestyle=linestyles[j],
                 lw=2, label=label)

plt.xscale('log')
plt.xlim(1, 1e4)
plt.xlabel('Kd [$\mu$M]')
plt.ylabel('R$_1$ [s$^{-1}$]')
```

```
plt.title('$^{13}$C Pyruvate R$_1$ vs Kd at 1.0T')
plt.legend(fontsize=8, bbox_to_anchor=(1.05, 1))
plt.tight_layout()
plt.show()
```

## A.13. Relaxation Parameter Extraction from Experimental Intensities

The following Python script was used to process experimental NMR intensity data of $^{13}$C-pyruvate acquired at 1.3 T. The code computes relaxation parameters ($R_1, R_{1\rho}, T_1, T_2$) with propagated uncertainties and generates plots of their dependence on protein concentration.

**Code A.12:** Relaxation analysis using hyperpolarized intensities.

```
import numpy as np
import matplotlib.pyplot as plt
import matplotlib.gridspec as gridspec

# --- Experimental parameters ---
t_decay = 10       # seconds for T1
delta_t = 0.3      # seconds for T2 (R1rho)
T1_free = 46       # seconds (free pyruvate at 1T)
sigma_I1_rel = 0.045    # 4.5% for I1
sigma_I2_rel = 0.06     # 6% for I2

# --- Datasets ---
datasets = [
    {'name': 'Dataset 1',
        'conc': np.array([0, 1.0, 1.5, 2.0]),
        'I1': np.array([58.48, 58.68, 43.53, 24.65]),
        'I2': np.array([40.91, 38.25, 24.84, 11.94]) },
    {'name': 'Dataset 2',
        'conc': np.array([0, 1.0, 1.5, 2.0]),
        'I1': np.array([111.39, 112.38, 89.34, 38.84]),
        'I2': np.array([81.61, 77.03, 54.42, 17.42])}
]

# --- Function ---
def compute_relaxation(conc, I1, I2, t_decay, delta_t, T1_free, sigma_I1_rel, sigma_I2_rel):
    # M0 from free pyruvate
    M0 = I1[0] * np.exp(t_decay / T1_free)

    # R1, T1
    R1 = -np.log(I1 / M0) / t_decay
    sigma_R1 = np.full_like(R1, (np.sqrt(2) * sigma_I1_rel) / t_decay)
    T1 = 1 / R1
    sigma_T1 = sigma_R1 / (R1**2)

    # R1rho, T2
    R1rho = -np.log(I2 / I1) / delta_t
    sigma_R1rho = np.full_like(R1rho, (np.sqrt(sigma_I1_rel**2 + sigma_I2_rel**2)) / delta_t)
    T2 = 1 / R1rho
    sigma_T2 = sigma_R1rho / (R1rho**2)

    # Remaining signal (% of initial)
    remaining = (I1 / M0) * 100
    sigma_rem = sigma_I1_rel * remaining
```

```
    return {'M0': M0, 'R1': R1, 'sigma_R1': sigma_R1, 'T1': T1, 'sigma_T1': sigma_T1,
            'R1rho': R1rho, 'sigma_R1rho': sigma_R1rho, 'T2': T2, 'sigma_T2': sigma_T2,
            'remaining': remaining, 'sigma_rem': sigma_rem}

# --- Compute for all datasets ---
for d in datasets:
    params = compute_relaxation(d['conc'], d['I1'], d['I2'], t_decay, delta_t, T1_free, sigma_I1_rel,
     sigma_I2_rel)
    d.update(params)

# --- Plotting ---
markers = ['o', 's']
colors = ['red', 'blue']

plt.figure(figsize=(16, 12))
gs = gridspec.GridSpec(3, 2, height_ratios=[1, 1, 1])

# Plot 1: Signal Remaining
ax1 = plt.subplot(gs[0, 0])
for i, d in enumerate(datasets):
    ax1.errorbar(d['conc'], d['remaining'], yerr=d['sigma_rem'], fmt=markers[i], color=colors[i],
     label=d['name'], capsize=4, markersize=8)
ax1.set_xlabel('Protein Concentration (uM)')
ax1.set_ylabel('Signal Remaining (%)')
ax1.set_title('Signal Remaining After 10 s Evolution')
ax1.grid(alpha=0.3)
ax1.legend()

# Plot 2: R1
ax2 = plt.subplot(gs[0, 1])
for i, d in enumerate(datasets):
    ax2.errorbar(d['conc'], d['R1'], yerr=d['sigma_R1'], fmt=markers[i], color=colors[i], label=d['name'],
    capsize=4, markersize=8)
ax2.set_xlabel('Protein Concentration (uM)')
ax2.set_ylabel('R1 (s^-1)')
ax2.set_title('Longitudinal Relaxation Rate R1')
ax2.grid(alpha=0.3)
ax2.legend()

# Plot 3: R1rho
ax3 = plt.subplot(gs[1, 0])
for i, d in enumerate(datasets):
    ax3.errorbar(d['conc'], d['R1rho'], yerr=d['sigma_R1rho'], fmt=markers[i],color=colors[i],
    label=d['name'], capsize=4, markersize=8)
ax3.set_xlabel('Protein Concentration (uM)')
ax3.set_ylabel('R1rho (s^-1)')
ax3.set_title('Spin-Lock Relaxation Rate R1rho')
ax3.grid(alpha=0.3)
ax3.legend()

# Plot 4: T1
ax4 = plt.subplot(gs[1, 1])
for i, d in enumerate(datasets):
    ax4.errorbar(d['conc'], d['T1'], yerr=d['sigma_T1'], fmt=markers[i], color=colors[i], label=d['name'],
    capsize=4, markersize=8)
ax4.set_xlabel('Protein Concentration (uM)')
ax4.set_ylabel('T1 (s)')
ax4.set_title('Longitudinal Relaxation Time T1')
ax4.grid(alpha=0.3)
ax4.legend()
```

```
# Plot 5: T2 (from R1rho)
ax5 = plt.subplot(gs[2, 0])
for i, d in enumerate(datasets):
    ax5.errorbar(d['conc'], d['T2'], yerr=d['sigma_T2'], fmt=markers[i], color=colors[i], label=d['name'],
     capsize=4, markersize=8)
ax5.set_xlabel('Protein Concentration (uM)')
ax5.set_ylabel('T2 (s)')
ax5.set_title('Transverse Relaxation Time T2 (from R1rho)')
ax5.grid(alpha=0.3)
ax5.legend()
# Plot 6: Theoretical decay curves from R1
ax6 = plt.subplot(gs[2, 1])
time = np.linspace(0, 30, 300)
for i, d in enumerate(datasets):
    for j, c in enumerate(d['conc']):
        decay = d['M0'] * np.exp(-d['R1'][j] * time)
        ax6.plot(time, decay, color=colors[i], alpha=0.7,
                 label=f"{d['name']} {c} uM" if j == 0 else "")
ax6.set_xlabel('Time (s)')
ax6.set_ylabel('Signal Intensity')
ax6.set_title('Theoretical Signal Decay (from R1)')
ax6.grid(alpha=0.3)
ax6.legend()
plt.tight_layout()
plt.savefig("relaxation_analysis_complete.pdf", dpi=600, bbox_inches="tight", transparent=True)
```

**Table A.2.:** Relaxation parameters from Dataset 1

| Conc | I1 | I2 | Remain (%) | R1 | $\sigma_{R1}$ | T1 | $\sigma_{T1}$ | R1ρ | $\sigma_{R1r}$ | T2 | $\sigma_{T2}$ |
|---|---|---|---|---|---|---|---|---|---|---|---|
| 0.0 | 111.39 | 81.61 | 80.07 | 0.022 | 0.006 | 46.00 | 13.47 | 1.037 | 0.25 | 0.96 | 0.23 |
| 1.0 | 112.38 | 77.03 | 80.79 | 0.021 | 0.006 | 47.95 | 14.63 | 1.259 | 0.25 | 0.79 | 0.16 |
| 1.5 | 89.34 | 54.42 | 64.22 | 0.044 | 0.006 | 22.83 | 3.32 | 1.652 | 0.25 | 0.61 | 0.09 |
| 2.0 | 38.84 | 17.42 | 27.92 | 0.127 | 0.006 | 7.87 | 0.39 | 2.673 | 0.25 | 0.37 | 0.03 |

**Table A.3.:** Relaxation parameters from Dataset 2

| Conc | I1 | I2 | Remain (%) | R1 | $\sigma_{R1}$ | T1 | $\sigma_{T1}$ | R1ρ | $\sigma_{R1r}$ | T2 | $\sigma_{T2}$ |
|---|---|---|---|---|---|---|---|---|---|---|---|
| 0.0 | 58.48 | 40.91 | 80.07 | 0.022 | 0.006 | 46.00 | 13.47 | 1.191 | 0.25 | 0.84 | 0.18 |
| 1.0 | 58.68 | 38.25 | 80.35 | 0.021 | 0.006 | 46.73 | 13.90 | 1.426 | 0.25 | 0.70 | 0.12 |
| 1.5 | 43.53 | 24.84 | 59.60 | 0.051 | 0.006 | 19.51 | 2.42 | 1.870 | 0.25 | 0.53 | 0.07 |
| 2.0 | 24.65 | 11.94 | 33.75 | 0.108 | 0.006 | 9.25 | 0.54 | 2.416 | 0.25 | 0.41 | 0.04 |

## A.14. Relaxation contrast comparison of two datasets

**Code A.13:** Calculation and plotting of relaxation contrasts $C_{R1}$ and $C_{R2}$.

```
import numpy as np
import matplotlib.pyplot as plt

# --- Data ---
data = [
    # Dataset 1
    {'conc': 0.0, 'R1': 0.0217, 'sigma_R1': 0.0064, 'R1rho': 1.0370, 'sigma_R1rho': 0.25},
    {'conc': 1.0, 'R1': 0.0209, 'sigma_R1': 0.0064, 'R1rho': 1.2590, 'sigma_R1rho': 0.25},
```

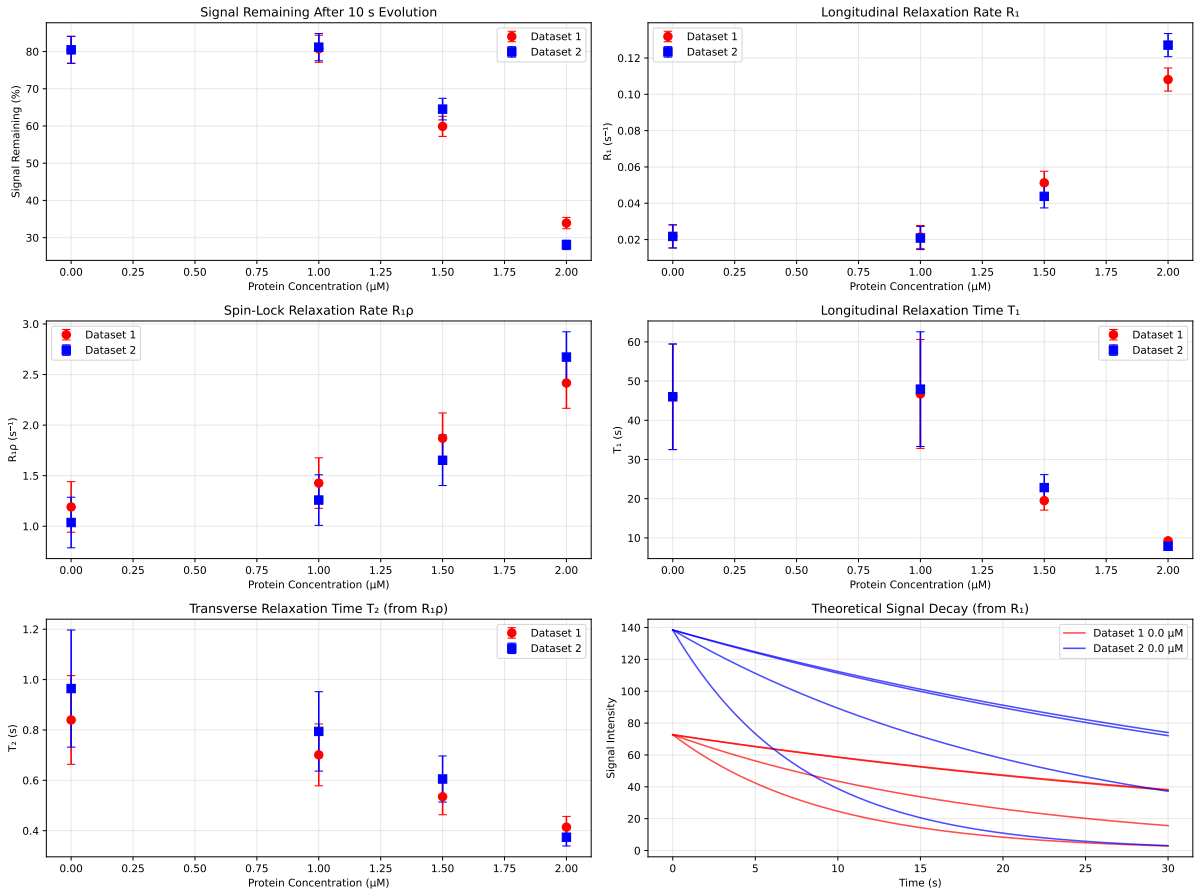


**Figure A.2.:** The remaining percentage signal after 10 s waiting time at 1.3 T, with $T_1$ = 46 s in the first plot. The calculated $R_1$ relaxation rate and $R_1\rho$ are shown in the second and third plots. The corresponding $T_1$ and $T_{1\rho}$ are shown in the fourth and fifth plots. The decay rate is shown last plot.

```
    {'conc': 1.5, 'R1': 0.0438, 'sigma_R1': 0.0064, 'R1rho': 1.6524, 'sigma_R1rho': 0.25},
    {'conc': 2.0, 'R1': 0.1271, 'sigma_R1': 0.0064, 'R1rho': 2.6728, 'sigma_R1rho': 0.25},
    # Dataset 2
    {'conc': 0.0, 'R1': 0.0217, 'sigma_R1': 0.0064, 'R1rho': 1.1910, 'sigma_R1rho': 0.25},
    {'conc': 1.0, 'R1': 0.0214, 'sigma_R1': 0.0064, 'R1rho': 1.4265, 'sigma_R1rho': 0.25},
    {'conc': 1.5, 'R1': 0.0513, 'sigma_R1': 0.0064, 'R1rho': 1.8700, 'sigma_R1rho': 0.25},
    {'conc': 2.0, 'R1': 0.1081, 'sigma_R1': 0.0064, 'R1rho': 2.4163, 'sigma_R1rho': 0.25}
]

# Split into two datasets
dataset1 = data[:4]
dataset2 = data[4:]

def calculate_contrasts(dataset):
    """Calculate C_R1 and C_R2 contrasts with correct error propagation"""
    # Free ligand values (conc = 0)
    R1_0 = dataset[0]['R1']
    sigma_R1_0 = dataset[0]['sigma_R1']
    R2_0 = dataset[0]['R1rho']  # Using R1rho as R2
    sigma_R2_0 = dataset[0]['sigma_R1rho']

    contrasts = []
```

```
    for point in dataset:
        # Contrasts
        C_R1 = (point['R1'] - R1_0) / R1_0
        C_R2 = (point['R1rho'] - R2_0) / R2_0

        # Error propagation (includes error in reference)
        sigma_C_R1 = np.sqrt((point['sigma_R1']/R1_0)**2 + (point['R1']*sigma_R1_0/(R1_0**2))**2)
        sigma_C_R2 = np.sqrt((point['sigma_R1rho']/R2_0)**2 + (point['R1rho']*sigma_R2_0/(R2_0**2))**2)

        contrasts.append({
            'conc': point['conc'],
            'C_R1': C_R1,
            'sigma_C_R1': sigma_C_R1,
            'C_R2': C_R2,
            'sigma_C_R2': sigma_C_R2
        })

    return contrasts

# Calculate contrasts
contrasts1 = calculate_contrasts(dataset1)
contrasts2 = calculate_contrasts(dataset2)

# --- Print results ---
print("Dataset 1 Contrasts:")
print(f"{'Conc':>6} {'C_R1':>10} {'sigma_C_R1':>12} {'C_R2':>10} {'sigma_C_R2':>12}")
for c in contrasts1:
    print(f"{c['conc']:6.1f} {c['C_R1']:10.4f} {c['sigma_C_R1']:12.4f} {c['C_R2']:10.4f} {c['sigma_C_R2
     ']:12.4f}")

print("\nDataset 2 Contrasts:")
print(f"{'Conc':>6} {'C_R1':>10} {'sigma_C_R1':>12} {'C_R2':>10} {'sigma_C_R2':>12}")
for c in contrasts2:
    print(f"{c['conc']:6.1f} {c['C_R1']:10.4f} {c['sigma_C_R1']:12.4f} {c['C_R2']:10.4f} {c['sigma_C_R2
     ']:12.4f}")

# --- Plotting ---
plt.figure(figsize=(12, 5))

# C_R1 plot
plt.subplot(1, 2, 1)
conc1 = [c['conc'] for c in contrasts1]
C_R1_1 = [c['C_R1'] for c in contrasts1]
sigma_C_R1_1 = [c['sigma_C_R1'] for c in contrasts1]

conc2 = [c['conc'] for c in contrasts2]
C_R1_2 = [c['C_R1'] for c in contrasts2]
sigma_C_R1_2 = [c['sigma_C_R1'] for c in contrasts2]

plt.errorbar(conc1, C_R1_1, yerr=sigma_C_R1_1, fmt='ro-', capsize=4, label='Dataset 1')
plt.errorbar(conc2, C_R1_2, yerr=sigma_C_R1_2, fmt='gs-', capsize=4, label='Dataset 2')
plt.xlabel('Protein Concentration (uM)')
plt.ylabel('C_R1')
plt.title('R1 Relaxation Contrast')
plt.grid(alpha=0.3)
plt.legend()

# C_R2 plot
plt.subplot(1, 2, 2)
C_R2_1 = [c['C_R2'] for c in contrasts1]
```

```
sigma_C_R2_1 = [c['sigma_C_R2'] for c in contrasts1]
C_R2_2 = [c['C_R2'] for c in contrasts2]
sigma_C_R2_2 = [c['sigma_C_R2'] for c in contrasts2]

plt.errorbar(conc1, C_R2_1, yerr=sigma_C_R2_1, fmt='ro-', capsize=4, label='Dataset 1')
plt.errorbar(conc2, C_R2_2, yerr=sigma_C_R2_2, fmt='gs-', capsize=4, label='Dataset 2')
plt.xlabel('Protein Concentration (uM)')
plt.ylabel('C_R2')
plt.title('R2 Relaxation Contrast')
plt.grid(alpha=0.3)
plt.legend()

plt.tight_layout()
plt.savefig("relaxation_contrasts.pdf", dpi=600, bbox_inches='tight', transparent=True)
plt.show()
```